-109 c.1

NOAA Technical Report NMFS 109 April 1992

Seasonal Climatologies and Variability of Eastern Tropical Pacific Surface Waters

Paul C. Fiedler

LIBRARY

JUL 10 1992

National Marine Fisheries Service
2570 Dole Street
Honolulu, Hawaii

NOAA
Tech.
Rept.
NMFS
109
c.1

U.S. Department of Commerce

Library
NOAA, National Marine Fisheries Service
SWFC Honolulu Laboratory F/SWC2
2570 Dole Street
Honolulu, HI 96822-2396

NOAA Technical Reports NMFS

The major responsibilities of the National Marine Fisheries Service (NMFS) are to monitor and assess the abundance and geographic distribution of fishery resources, to understand and predict fluctuations in the quantity and distribution of these resources, and to establish levels for their optimum use. NMFS is also charged with the development and implementation of policies for managing national fishing grounds, with the development and enforcement of domestic fisheries regulations, with the surveillance of foreign fishing off U.S. coastal waters, and with the development and enforcement of international fishery agreements and policies. NMFS also assists the fishing industry through marketing service and economic analysis programs and through mortage insurance and vessel construction subsidies. It collects, analyzes, and publishes statistics on various phases of the industry.

The NOAA Technical Report NMFS series was established in 1983 to replace two subcategories of the Technical Report series: "Special Scientific Report —Fisheries" and "Circular." The series contains the following types of reports: scientific investigations that document long-term continuing programs of NMFS; intensive scientific reports on studies of restricted scope; papers on applied fishery problems; technical reports of general interest intended to aid conservation and management; reports that review, in considerable detail and at a high technical level, certain broad areas of research; and technical papers originating in economics studies and in management investigations. Since this is a formal series, all submitted papers, except those of the U.S.-Japan series on aquaculture, receive peer review and all papers, once accepted, receive professional editing before publication.

Copies of NOAA Technical Reports NMFS are available free in limited numbers to government agencies, both federal and state. They are also available in exchange for other scientific and technical publications in the marine sciences. Individual copies may be obtained from the U.S. Department of Commerce, National Technical Information Service, 5285 Port Royal Road, Springfield, VA 22161. Although the contents of these reports have not been copyrighted and may be reprinted entirely, reference to source is appreciated.

Recently Published NOAA Technical Reports NMFS

96. **Marine flora and fauna of the eastern United States—Copepoda, Cyclopoida: Archinotodelphyidae, Notodelphyidae, and Ascidicolidae,** by Patricia L. Dudley and Paul L. Illg. January 1991, 40 p.

97. **Catalog of osteological collections of aquatic mammals from Mexico,** by Omar Vidal. January 1991, 36 p.

98. **Marine mammal strandings in the United States: proceedings of the second marine mammal stranding workshop; Miami, Florida, 3–5 December, 1987,** edited by John E. Reynolds III and Daniel K. Odell. January 1991, 157 p.

99. **Marine flora and fauna of the northeastern United States: erect Bryozoa,** by John S. Ryland and Peter J. Hayward. February 1991, 48 p.

100. **Marine flora and fauna of the eastern United States: Dicyemida,** by Robert B. Short. February 1991, 16 p.

101. **Larvae of nearshore fishes in oceanic waters near Oahu, Hawaii,** by Thomas A. Clarke. March 1991, 19 p.

102. **Marine ranching: proceedings of the seventeenth U.S.-Japan meeting on aquaculture; Ise, Mie Prefecture, Japan, 16–18 October 1988,** edited by Ralph S. Svrjcek. May 1991, 180 p.

103. **Benthic macrofauna of the New York Bight, 1979–89,** by Robert N. Reid, David J. Radosh, Ann B. Frame, and Steven A. Fromm. December 1991, 50 p.

104. **Incidental catch of marine mammals by foreign and joint venture trawl vessels in the U.S. EEZ of the North Pacific, 1973–88,** by Michael A. Perez and Thomas R. Loughlin. December 1991, 57 p.

105. **Biology, oceanography, and fisheries of the North Pacific transition zone and subarctic frontal zone,** edited by Jerry A. Wetherall. December 1991, 111 p.

106. **Marine ranching: proceedings of the eighteenth U.S.-Japan meeting on aquaculture; Port Ludlow, Washington, 18–19 September 1989,** edited by Ralph S. Svrjcek. February 1992, 136 p.

107. **Field guide to the searobins (*Prionotus* and *Bellator*) in the western North Atlantic,** by Mike Russell, Mark Grace, and Elmer J. Gutherz. March 1992, 26 p.

NMFS Honolulu Library
00000000004809

NOAA Technical Report NMFS 109

Seasonal Climatologies and Variability of Eastern Tropical Pacific Surface Waters

Paul C. Fiedler

April 1992

U.S. DEPARTMENT OF COMMERCE
Barbara Hackman Franklin, Secretary
National Oceanic and Atmospheric Administration
John A. Knauss, Under Secretary for Oceans and Atmosphere
National Marine Fisheries Service
William W. Fox Jr., Assistant Administrator for Fisheries

The National Marine Fisheries Service (NMFS) does not approve, recommend or endorse any proprietary product or proprietary material mentioned in this publication. No reference shall be made to NMFS, or to this publication furnished by NMFS, in any advertising or sales promotion which would indicate or imply that NMFS approves, recommends or endorses any proprietary product or proprietary material mentioned herein, or which has as its purpose an intent to cause directly or indirectly the advertised product to be used or purchased because of this NMFS publication.

Seasonal Climatologies and Variability of Eastern Tropical Pacific Surface Waters

PAUL C. FIEDLER

NOAA/NMFS/Southwest Fisheries Science Center
P.O. Box 271
La Jolla, CA 92038

ABSTRACT

Interannual variability caused by the El Niño-Southern Oscillation in the eastern tropical Pacific Ocean (ETP) is analogous to seasonal variability of comparable magnitude. Climatological spatial patterns and seasonal variability of physical variables that may affect the ETP ecosystem are presented and discussed. Surface temperature, surface salinity, mixed layer depth, thermocline depth, thermocline strength, and surface dynamic height were derived from bathythermograph, hydrocast, and CTD data. Surface current velocity, divergence, and upwelling velocity were derived from ship drift reports. Surface wind velocity, wind stress, wind divergence, wind stress curl, and Ekman pumping velocity were derived from gridded pseudostress data obtained from Florida State University. Seasonal maps of these variables, and their deviations from the annual mean, show different patterns of variation in Equatorial (5°S–5°N) and Tropical Surface Water (5°–15°N). Seasonal shifts in the trade winds, which affect the strength of equatorial upwelling and the North Equatorial Countercurrent, cause seasonal variations in most variables. Seasonal and interannual variability of surface temperature, mixed layer depth, thermocline depth and wind stress were quantified. Surface temperature, mixed layer depth and thermocline depth, but not local wind stress, are less variable in Tropical Surface Water than in Equatorial Surface Water. Seasonal and interannual variability are close to equal in most of the ETP, within factors of 2 or less.

Introduction

The physical oceanography of the eastern tropical Pacific Ocean (ETP) was described by Cromwell (1958) and Wyrtki (1966, 1967), based on sparse observations by research ships. Research ships and ships-of-opportunity have made many additional observations since Wyrtki's description. The National Marine Fisheries Service/Southwest Fisheries Science Center is currently monitoring the distribution and variability of dolphin stocks affected by the tuna purse seine fishery in the ETP. This program requires a comprehensive review of the climatological distributions and variability of physical oceanographic variables in the surface waters of the ETP.

The surface waters of the eastern tropical Pacific Ocean are subject to great variability caused by the El Niño-Southern Oscillation (ENSO), a 3–6 year cycle within the coupled ocean-atmosphere system of the tropical Pacific (Enfield 1989). This interannual variability has profound biological consequences (Walsh 1978; Barber and Chavez 1986). In the past, oceanic tropical marine ecosystems have been characterized as exhibiting little or no seasonal variation, probably due to the paucity of observations (Heinrich 1962; Sournia 1969). Walsh (1978) did not even consider the seasonal scale in a review of biological variability in the eastern tropical Pacific. Yet, seasonal variability is observed. Seasonal variability of temperature, wind, sea level, and other physical variables in the ETP has been described and analyzed by Hickey

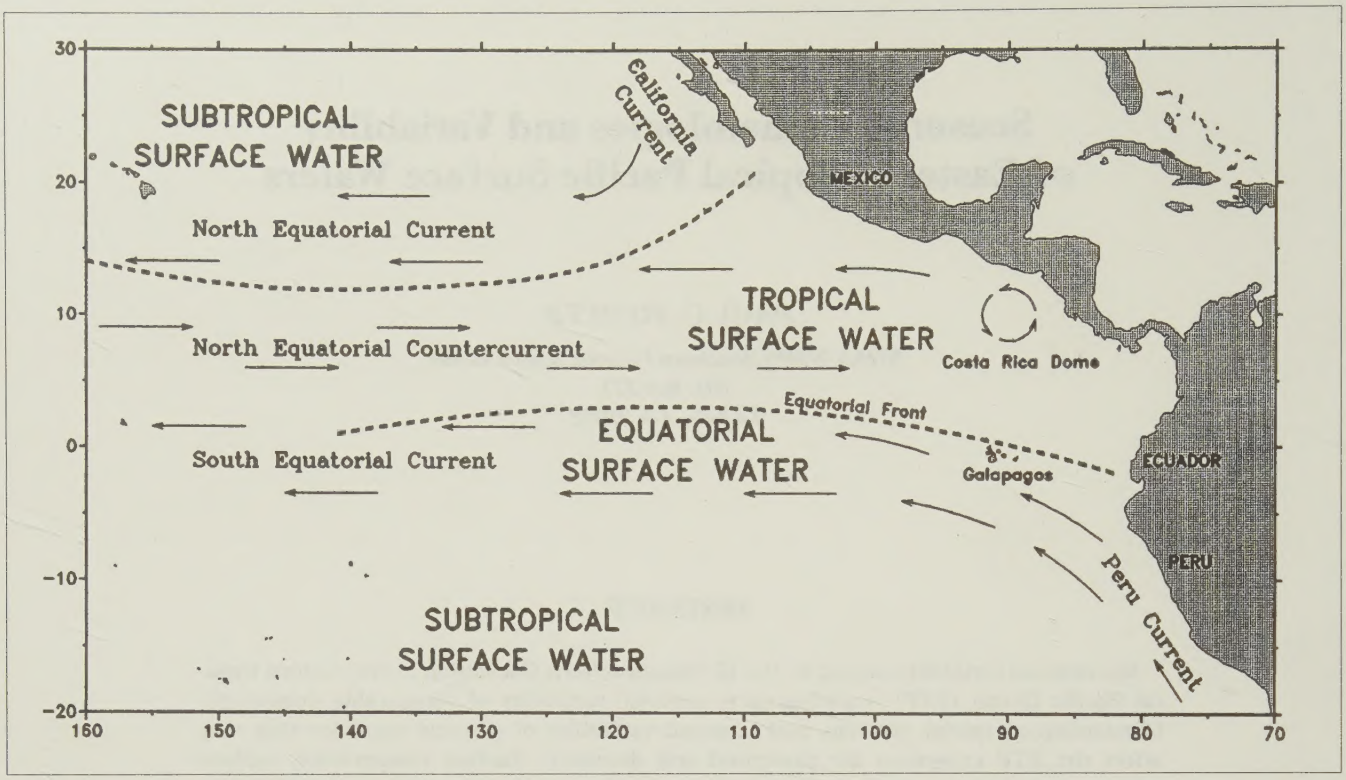

Figure 1
Schematic map of surface currents and water masses in the eastern tropical Pacific Ocean (Wyrtki 1966, 1967).

(1975) and Horel (1982). Primary production and plankton stocks measured during the 14-month EASTROPAC expedition of 1967–1968 varied by a factor of 2 in an apparent seasonal cycle (Blackburn et al. 1970; Owen and Zeitschel 1970). Reilly (1990) found variations in distributions of dolphin species, measured in different seasons in different years, that are consistent with seasonal environmental variability. In this report, I examine seasonal variability of physical variables that affect the ETP ecosystem and quantify relationships between seasonal and interannual variability. The report is intended primarily as a compilation of available data presented in a useful format and not a detailed or exhaustive interpretation of the data.

Background

Surface waters and currents of the ETP (Fig. 1) interact with the northeast and southeast trade winds, which blow around high pressure centers in the NE and SE Pacific, on either side of the equatorial low. The generally westward and equatorward trade winds drive surface waters to the west in the North and South Equatorial Currents (NEC, SEC). This transport sets up a downward slope of the sea surface of about half a meter from west to east across the tropical Pacific. The two trade wind belts converge north of the equator, between 5° and 10°N latitude, in the Intertropical Convergence Zone (ITCZ), where winds are weak (the doldrums). The eastward pressure gradient force exceeds the westward wind stress in the doldrums, so that the North Equatorial Countercurrent (NECC) flows eastward between the NEC and SEC.

The North and South Equatorial Currents are part of the subtropical, anticyclonic gyral circulations of the North and South Pacific. The California and Peru Currents form the eastern boundary currents of these gyres. They flow equatorward along the coasts of Baja California and Peru into the ETP, feeding the eastern, "upstream" ends of the NEC and SEC.

There are three principal surface water masses in the ETP: Tropical Surface Water, Subtropical Surface Water, and Equatorial Surface Water (Fig. 1). Each of these water masses has characteristic properties determined by climate regimes at local or remote points of origin. Tropical Surface Water (TSW) is

found in the center of the ETP, along 10°N. It is the warmest and least saline water in the ETP. Salinity is low because rainfall exceeds evaporation beneath the cloudy and rainy ITCZ. Cool, high-salinity Subtropical Surface Water (SSW) is found toward the poleward edges of the ETP, in the subtropical gyres of the North and South Pacific. Evaporation greatly exceeds rainfall, and surface salinity is over 36 psu in the center of the subtropical gyres.

Equatorial Surface Water (ESW) is found between the Tropical and southern Subtropical Surface Water masses. It appears as the tongue of anomalously cold water extending westward along the equator from the Peruvian coast. Salinity of ESW is intermediate between that of low-salinity TSW and high-salinity SSW. The cold tongue is maintained either by equatorial upwelling and advection of cold water from the Peru Current by the South Equatorial Current (Wyrtki 1981) and by the eastward advection of cold water by the Equatorial Undercurrent as it rises to the surface near 95°W (Bryden and Brady 1985).

In addition to the three oceanic surface water masses, the cool, low-salinity waters of the Peru and California Currents are also found in the ETP. Peru Current water is contiguous with ESW. Along the Central American coast, small and ephemeral water masses containing cool, recently upwelled water may be present.

Both coastal upwelling along eastern boundaries and equatorial upwelling occur in the ETP. Equatorial upwelling is the result of geostrophic divergence of the wind-driven SEC. The westward component of the southeast trade winds causes poleward Ekman transport of surface water on either side of the equator. The effects of upwelling are evident in the shoaling of the thermocline along the equator and in the anomalously cold temperature of Equatorial Surface Water. Sverdrup et al. (1942) presented evidence of surface divergence and upwelling at two sites in the equatorial current system: along the equator and between the NECC and NEC at 10°N. Offshore transport of surface waters and coastal upwelling are driven by equatorward longshore winds along the coasts of Baja California and Peru, and by topographically induced offshore winds at several points along the coast of Central America.

Methods

The limits of the ETP for this study are 20°S–30°N latitude and 70°–160°W longitude, to cover the eastern boundary current source waters and the zonal equatorial current system into the central equatorial Pacific. Hydrographic data were obtained from two sources: 1) National Oceanographic Data Center (NODC) CD-ROM NODC-03: Global Ocean Temperature and Salinity Profiles, vol. 2, Pacific Ocean, and 2) a Pacific Marine Environmental Laboratory (PMEL) bathythermograph dataset compiled and edited by Kessler (1990). The NODC data consist of MBT (mechanical bathythermograph), XBT (expendable bathythermograph), CTD (conductivity-temperature-depth), and oceanographic station (hydrocast) data collected between 1900 and 1990. Radio-message bathythermograph data were excluded.

NODC screened the CD-ROM data with logical tests for valid in-water positions and depths and a crude statistical test: a cast or station was rejected if temperature (or salinity) at any depth deviated by more than four standard deviations from the ten-degree square mean value. This screen rejected 2.4% of the MBT/XBT profiles and 2.2% of the CTD/hydrocast profiles in the entire Pacific Ocean data set (Topoly et al. 1989). NODC bathythermograph data collected since 1960 in the ETP study area (n=134,756) were futher screened by rejecting casts with temperature inversions >1°C and deep casts (>400 m) in which the deepest temperature exceeded 20°C (indicating a broken XBT wire). This preliminary screen rejected 1.5% of the profiles remaining after the NODC screen.

The PMEL bathythermograph data (63,715 casts in the ETP study area) consist of NODC XBT data (1967–1985), French-American ship-of-opportunity XBT data (1979–1987), and Japanese Far Seas Fisheries Research Laboratory MBT data (1970–1980). Kessler (1990) carefully screened these data for errors. I further screened the NODC MBT/XBT profiles with a statistical test based on 2 × 5-degree latitude-longitude means and standard deviations of the PMEL data: a cast was rejected if surface temperature or 20°C isotherm depth deviated from the mean by more than 3 standard deviations. This final screen rejected 7.8% of the NODC profiles remaining after the preliminary screen. The screened NODC data consisted of 122,425 profiles. The PMEL data set contained 15,442 additional profiles, for a total of 137,867 MBT and XBT profiles (1960–1990) available for analyses of surface temperature, mixed layer depth, thermocline depth, and thermocline strength in the ETP (Fig. A-1).

Mixed layer depth has been defined in various ways to represent the depth of the wind-mixed (isothermal or homogeneous) layer at the ocean surface. The most widely-used definition of mixed layer depth, and the definition used here, is the depth at which

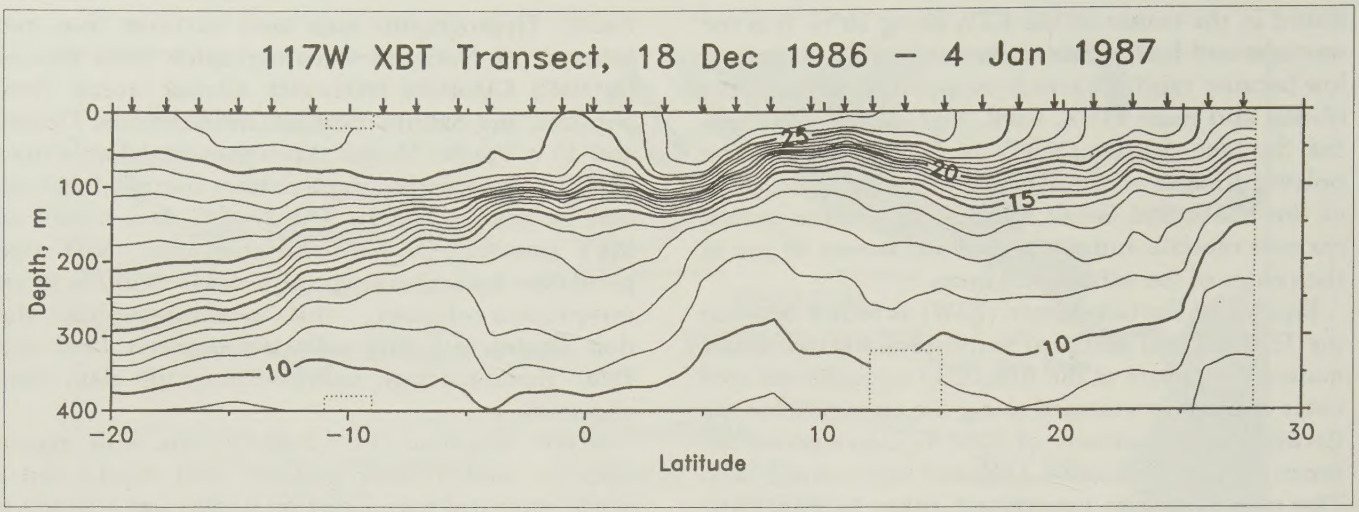

Figure 2

Meridional XBT transect across the eastern tropical Pacific (along approximately 117°W) by the albacore fishing vessel *Bald Eagle,* 18 December 1986–4 January 1987, showing the 20°C and 15°C isotherms located in the middle and bottom of the thermocline, respectively.

temperature is 0.5°C less than surface temperature (e.g. Wyrtki 1964; Levitus 1982).

The 20°C isotherm is in the middle of the thermocline over most of the tropical Pacific (Fig. 2). Depth of the 20°C isotherm is conventionally used to represent thermocline depth in the equatorial Pacific (Donguy and Meyers 1987). It represents the permanent thermocline, not the secondary shallow thermocline that develops during summer at the subtropical extremes of the ETP and in Peru Current water (Wyrtki 1966). Where surface temperature is less than 20°C, thermocline depth is undefined.

I used CTD and hydrocast data from the NODC data set for analyses of surface salinity and 0/500 db dynamic height. NODC screens these data somewhat more thoroughly than the bathythermograph data, so no additional quality control was attempted here. Casts for which the first recorded depth exceeded 10 m (2.5% of the total) and hydrocasts collected prior to 1960 (28.6%) were excluded. This left 18,711 hydrocasts and 8,029 CTD casts in the study area (1960-1988, Fig. A-1), with 26,149 surface salinity observations and 12,440 profiles with sufficient data to calculate 0/500db dynamic height. Tsuchiya (1974) claimed that 500 db is a valid reference level for estimating surface geostrophic flow in the ETP, because waters deeper than 500 m are relatively homogeneous.

Ship drift reports are from the NODC Surface Current Data Set. Most of these data were provided by the U. S. Navy Fleet Numerical Oceanography Center, with some missing data obtained from NODC. For the study region, there were 229,782 ship drift reports for the period 1900–1969 (Fig. A-1). Surface current vectors were averaged seasonally on a 2 × 2-degree latitude-longitude grid. Observations were averaged within ±2 degree latitude and up to ±10 degrees longitude of each grid point, to resolve the predominantly zonal structure of equatorial surface currents. Meehl (1982) showed that surface currents estimated from ship drift were about equal to directly measured currents from drift buoys or current meters, and about twice as large as computed geostrophic currents. McPhaden et al. (1991), however, found that windage can bias ship drift data by up to 3% of the surface wind speed. Richardson (1989) identified 10-degree square and monthly blocks of missing data in the global Surface Current Data Set. Although no gaps were seen in the seasonal distributions of data in our study area, it is possible that missing months or years in some seasonal blocks could confound the patterns of spatial and seasonal variability.

Data were gridded by season on a 2-degree latitude-longitude grid. At each grid point, the mean of at least 20 observations within 2 degrees or more was calculated. Normal probability plots of data for representative seasonal grid points indicate that the data are close to normally distributed in tropical and subtropical waters (Fig. A-2). Although equatorial data tend to be bimodally distributed due to ENSO variability, the mean and standard deviation appear to be appropriate measures of central tendency and dispersion for most of the study area. No attempt was made to correct the bimodality of equatorial data, for instance by treating data from El Niño years separately.

The range of observations around a grid point was increased in increments of one degree to obtain a minimum sample size for each mean (n=20 for

bathythermograph and hydrocast data, n=100 for ship drift data). Thus, local grid resolution decreases in data-poor regions. A larger minimum sample size was used for ship drift data because of the high coefficient of variation of the observations (compare range and mean in Fig. A-2d). In data-poor regions, generally south of the equator, the maximum radius required was 8 degrees for bathythermograph data and 10 degrees for hydrocast and ship drift data (Fig. A-3). Within ±10 degrees longitude of a few grid points, there were less than 100 ship drift observations, but never less than 25.

The standard deviations (rms deviations) and numbers of observations in grid point samples are plotted in Figure A-4. Ranges of standard error (rms error) for 95% of the grid means are 0.04–0.31°C for surface temperature, 0.6–7.0 m for mixed layer depth, 0.8–5.6 m for thermocline depth, 0.01–0.17 psu for surface salinity, 0.4–3.1 dyn cm for surface dynamic height, 0.8–5.0 cm s^{-1} for eastward ship drift, and 0.7–3.6 cm s^{-1} for northward ship drift.

Annual climatologies were computed as averages of the four seasonal grids, to eliminate bias caused by non-uniform sampling over seasons. Seasonal variability is illustrated by contour maps of the seasonal grids and of the seasonal deviations from the climatology (seasonal grid minus climatology).

Surface wind data were obtained as monthly 2 × 2-degree grids of pseudostress (wind components multiplied by wind magnitude, m^2 s^{-2} (Legler and O'Brien 1988) for the period 1961–1989. Pseudostress was converted to wind stress (dyne cm^{-2}) using a constant drag coefficient of 1.4×10^{-3} and an air density of 1.2 kg m^{-3}.

Several parameters were derived from the gridded fields of mixed layer depth, isotherm depths, ship drift, and wind pseudostress or stress. These parameters are thermocline strength, surface current divergence, upwelling velocity, surface wind divergence, wind stress curl, and Ekman pumping velocity.

Thermocline strength was derived from the 20° and 15°C isotherm fields as the temperature gradient between the two isotherms (°C $10m^{-1}$). The 15°C isotherm is typically near the bottom of the thermocline in the tropical Pacific (Fig. 2; Meyers 1979a).

Surface current divergence ($\partial u/\partial x + \partial v/\partial y$, 10^{-6} s^{-1}) was calculated from eastward and northward differences across a grid point of x and y components, respectively, of ship drift averaged between adjacent grid points. Horizontal transports were calculated by assuming that the mean surface currents between grid points, derived from the ship drift data, are uniform through the mixed layer. Upwelling velocity (10^{-3} cm s^{-1}, ≈ m d^{-1}) through the base of the mixed layer was calculated from divergence of the horizontal transports.

Surface wind divergence (10^{-6} s^{-1}) was calculated in the same way as surface current divergence. A similar finite-difference algorithm was used to calculate wind stress curl or vorticity (vertical component, 10^{-8} dyne cm^{-3}):

$$\mathrm{curl}_z(\tau) = \partial\tau_y/\partial x - \partial\tau_x/\partial y,$$

where τ_x and τ_y are the x and y components of wind stress τ.

Ekman pumping velocity, or vertical velocity at the bottom of the Ekman layer (10^{-3} cm s^{-1}), was calculated from wind stress as follows:

$$w_e = \mathrm{curl}_z(\tau/f)/\rho_w,$$

where f is the Coriolis parameter ($2\Omega\sin\theta$, Ω=angular velocity of the earth's rotation, θ=latitude) and ρ_w is water density (1000 kg m^{-3}). Ekman pumping velocity was calculated only for latitudes >6° from the equator: Ekman theory cannot be used to estimate upwelling near the equator, where the Coriolis force is zero and cannot balance wind stress. Coastal upwelling was estimated with this equation by setting $\tau_x = \tau_y = 0$ at the coast.

Seasonal and interannual variability of surface temperature, mixed layer depth and thermocline depth were estimated after averaging each variable in bins of 2 degrees latitude × 5 degrees longitude and two-month intervals from 1960 through 1989. Seasonal and interannual standard deviations were calculated as the standard deviations of bimonthly binned values after subtracting the yearly or bimonthly means for the bins. Sums of squares of MBT and XBT data were calculated separately, because Kessler (1990) noted a deep bias of MBT isotherm depths compared to XBT depths. Seasonal and interannual standard deviations were calculated only for bins with data in at least 15 of the 30 years and 5 of the 6 bimonths. Seasonal and interannual standard deviations of wind stress were calculated from the 1961–1989 monthly 2 × 2-degree grids averaged in bimonths. Standard deviations of the x and y components were calculated separately and summed. Thus, wind stress variability includes variations in both the magnitude and direction of wind stress.

Results

Annual Climatologies

The mean surface temperature field (Fig. A-5) has a band of warm water (>27°C) extending zonally across the ETP north of the equator, centered at 5°N in the

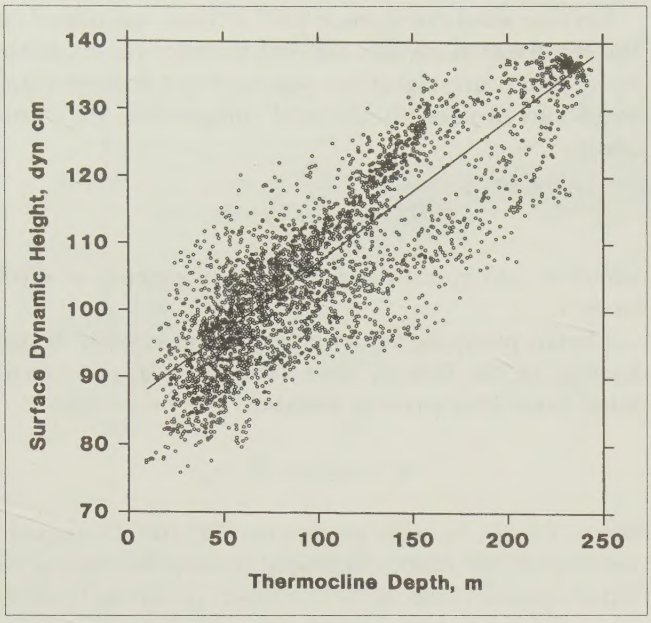

Figure 3
Surface dynamic height (0/500db, dyn cm) versus thermocline depth (m) in the seasonal climatologies. Solid line represents linear regression (r=0.84).

west and 15°N along the coast of Central America. This band is the eastern end of the large warm water resevoir straddling the equator in the western Pacific. East of 130°W, the "thermal equator" lies north of the geographic equator, with the warmest surface water found off the coast of Mexico. The coldest water in the ETP is off Baja California in the north and along the coast of Peru in the south. A band of cool water, the "cold tongue" of Wyrtki (1981), extends along or slightly south of the equator to the west of the Galapagos.

The mean surface salinity field is dominated by a zonal band of low-salinity water along 10°N (Fig. A-5). Salinity decreases to the east and is very low (<32 psu) in the Gulf of Panama. Salinity increases poleward of this band, except off the coast of Baja California. Oceanic surface water of the highest salinity is found south of 10°S.

The climatological fields of temperature and salinity define the three principal surface water masses in the ETP (Wyrtki 1966, 1967). The warm, low-salinity water centered on 10°N is Tropical Surface Water (TSW). The tongue of cool, moderately saline water along the equator is Equatorial Surface Water (ESW). High-salinity Subtropical Surface Water (SSW) is in the subtropical gyres of the North and South Pacific, toward the poleward edges of the ETP. The cold, low-salinity water off Baja California is California Current Water and the cold, moderately saline water off Peru is Peru Current Water.

Mean mixed layer depth increases from about 20–30 m along the coast to >70 m in the subtropical gyres (Fig. A-6). Shoaling of mean mixed layer depth at the poleward extremes of the study area, toward the centers of the gyres, is the result of high seasonal variability. Two zonal ridges in mixed layer depth lie along the equator and 10°N. East of 120°W, the mixed layer is most shallow along the equator, but to the west, it is most shallow along 10°N.

Mean thermocline topography is similar to that of mixed layer depth (Fig. A-6). Thermocline depth increases from 40–60 m along the coast to >150 m in the subtropical gyres. As for mixed layer depth, thermocline topography consists of a series of zonal ridges and troughs. I use the traditional names of ridges and troughs in sea level or surface dynamic height (Wyrtki 1974) to label the corresponding subsurface features in the thermocline topography: equatorial surface trough and thermocline ridge, countercurrent surface ridge and thermocline trough at 4°N, countercurrent surface trough and thermocline ridge at 10°N. The peak at the eastern end of the countercurrent thermocline ridge at 90°W is the Costa Rica Dome, a region of strong, localized upwelling (Wyrtki 1964; Hofmann et al. 1981).

The thermocline is strongest beneath Tropical Surface Water (Fig. A-7). The thermocline is somewhat weaker beneath Equatorial Surface Water, especially directly on the equator. Here the Equatorial Undercurrent, a geostrophically balanced, eastward, subsurface current, lies within the thermocline (Picaut et al. 1989). The thermocline is weakest beneath Subtropical Surface Water and in the Gulf of Panama, where low surface salinity strengthens the pycnocline beneath the surface layer.

The mean topographies of the thermocline and sea surface (surface dynamic height, Fig. A-8) are strongly correlated (Fig. 3, r=0.84). In general, sea level and depths of isotherms in the thermocline are highly correlated in the tropical Pacific (Rebert et al. 1985). Although thermocline topography, with an order of magnitude more data points, is better defined in most of the ETP, the equatorial and countercurrent surface troughs are evident in the mean surface topography. Spatial variations of surface dynamic height and thermocline depth reflect the directional tendencies of the largely zonal, near-surface currents of the ETP, following simple geostrophic theory. In the northern hemisphere, the sea surface will be higher (and the thermocline deeper) to the right of a current as the observer looks downstream. In the southern hemisphere, the opposite is true.

The broadest current in the ETP, the South Equatorial Current (SEC), flows westward through the region, spanning the equator from about 10°S to 4°N

along the equatorial surface trough (thermocline ridge). North of the countercurrent surface trough at 10°N, where the sea surface slopes upward to the north, the North Equatorial Current (NEC) also flows westward. Along the eastern boundary, the downward slope of the sea surface (and upward slope of the thermocline) toward the coasts of Peru and Baja California reflect the equatorward flow of the Peru and California Currents. The North Equatorial Countercurrent, flowing eastward on the southern slope of the countercurrent thermocline ridge between the NEC and SEC, is resolved in the mean surface dynamic height field only to the west of 130°W.

Surface currents from ship drift reports (Fig. A-8) are consistent with the geostrophic flow inferred from surface dynamic height and thermocline topographies. The strongest flow (up to 0.5 m s^{-1}) is within the westward South Equatorial Current, between 5°S and 3°N. The westward North Equatorial Current, north of 10°N, is weaker (about 0.2 m s^{-1}). The North Equatorial Countercurrent appears in the annual mean as a weak eastward flow between 5 and 10°N. The NECC undergoes substantial seasonal variation and is stronger in some seasonal climatologies, as will be seen below. The California and Peru Currents flow equatorward along the eastern boundaries of the ETP, with mean speeds of about 0.1 m s^{-1}.

Surface current divergence (Fig. A-9) is strongest along the equator, between 3°N and 3°S, and along the coast of Ecuador and Costa Rica. There is a strong convergence at 4–9°N, between the SEC and NECC. A strong divergence at 10°N, 86°W coincides with the Costa Rica Dome. Divergence is also strong along the coast of Ecuador and northern Peru. Weak divergences occur along the coast of Mexico and, offshore, at some points along 10°S and between 10°N and 20°N. Upwelling velocity, calculated from the divergence of surface transport in the mixed layer, is >1 x 10^{-3} cm s^{-1} (≈1 m d^{-1}) along the equator west of 110°W. Weaker oceanic upwelling occurs in a band centered on 15°N and south of the equator to the east of 120°W. Coastal upwelling is strongest off Ecuador and Costa Rica, with weaker upwelling along the coasts of Mexico and Peru.

The mean surface wind field shows the northeast and southeast trade winds converging at 10°N (Fig. A-10). Winds tend to be equatorward and longshore near the coast and more easterly to the west, reflecting the geostrophic flow of the trade winds around the North Pacific high pressure center at 35°N, 140°W and the South Pacific high at 30°S, 100°W (Oort 1983). This pattern of prevailing wind direction is summarized in Figure A-11. The mean surface wind divergence field shows the strong convergence of the trade wind belts (Intertropical Convergence Zone, ITCZ) between 5 and 15°N. Winds are weakly divergent over most of the remainder of the ETP.

Mean wind stress (and wind speed) is strongest in two offshore bands to the north of 10°N and south of the equator (Fig. A-11). Mean wind stress is weakest east of 120°W and north of the equator. Wind stress tends to be zonal over the open ocean and more meridional or longshore in coastal waters, except under the ITCZ. Longshore, equatorward winds blow along the coasts of Baja California and Peru, driving offshore transport of surface water and coastal upwelling. A band of weak winds, the doldrums, lies between the trade wind belts in the ITCZ east of 120°W.

The mean wind stress curl field (Fig. A-12) must be interpreted with care. In the northern hemisphere, positive curl is cyclonic. The resulting Ekman transport in the surface layer of the ocean is horizontally divergent and mass balance is conserved by upwelling of subsurface water. In the southern hemisphere, negative curl is cyclonic and forces upwelling into the surface layer. Thus, cyclonic wind stress curl (surface divergence) is found in the ITCZ at 10°N, except between 100°W and 110°W, and just south of the equator out to 130°W. Anticyclonic wind stress curl (surface convergence) is found north and south of the ITCZ in the northern hemisphere and south of 10°S.

The mean Ekman pumping velocity field (Fig. A-12) shows upwelling driven by positive (cyclonic) wind stress curl under the ITCZ along 10°N. The strong positive curl in this band west of 130°W does not result in upwelling because of the strong latitudinal gradient in Coriolis force south of 10°N. The greatest Ekman upwelling velocities are found off the coast of Costa Rica at the Costa Rica Dome, and along the coasts of Baja California and Ecuador-Peru.

Seasonal Climatologies and Deviations

Seasonal climatologies of surface temperature (Fig. A-13a) show that the band of warm Tropical Surface Water extends across the ETP in all seasons. The equatorial cold tongue is very weak in March–May. Surface temperature in much of the ETP varies seasonally by less than ±1°C (Fig. A-13b). Seasonal variation is greater in equatorial and coastal (Baja California and Peru Current) upwelling regions and in northern Subtropical Surface Water north of 20°N. The cool tongue of Equatorial Surface Water, out to 130°W, is 2–5°C warmer in boreal spring (March–May) than in fall (September–November). The nodal (zero deviation) line between seasonal

warming and cooling in the northern and southern hemispheres represents the "thermal equator" and lies between 10°N and 10°S, but usually north of the equator.

Surface salinity does not vary seasonally by more than ±0.1 psu, except along the coast of Central America (especially in the Gulf of Panama) and in the low-salinity core of Tropical Surface Water along 10°N (Fig. A-14). In these regions, surface salinity is low in fall (September–November) and high in spring (March–May).

Mixed layer depth (Fig. A-15) varies seasonally by ±10 m over most of the ETP and ±20–30 m north of 20°N and south of 15°S. The mixed layer shoals in summer and deepens in winter, with a nodal (zero seasonal deviation) line corresponding to the thermal equator in March–May and September–November. The seasonal deviation maps indicate phase differences in this seasonal change along the Mexican Coast (lead) and in equatorial waters west of 110°W (lag).

Thermocline depth (Fig. A-16) undergoes seasonal deviations of ±20 m only at the poleward extremes of the ETP. Seasonal variations of ±10 m, associated with the North Equatorial Countercurrent and equatorial upwelling, occur between 5°S and 15°N. Seasonal variations in the depths of the countercurrent thermocline trough and ridge are out of phase. Therefore, the slope between them is weakest in spring and strongest in fall. Thermocline depth does not vary seasonally directly beneath the core of the NECC at 8°N.

Seasonal climatologies of thermocline strength (Fig. A-17) show a strengthening of the strong thermocline beneath Tropical Surface Water in spring (March–May) and a weakening in fall (September–November). This pattern is not coherent across the ETP. East of 125°W, this strengthening begins in winter and the weakening begins in summer. The equatorial thermocline is weakest in March–May.

Seasonal climatologies and deviations of sea surface dynamic height (Fig. A-18) roughly correspond to those of thermocline depth. For example, positive spring and negative fall deviations of the countercurrent surface trough are accompanied by opposing deviations of the underlying countercurrent thermocline ridge. The meridional sea surface slope associated with the North Equatorial Countercurrent west of 130°W is much steeper in fall than in spring. Sea surface slope along the equator, produced by the piling up of surface water in the western Pacific by trade winds, is seasonally weak in March–May and strong in September–November. In contrast, the zonal sea surface slope associated with the California Current off Baja California is strong in spring (March–May) and weak in fall (September–October).

Seasonal variability of surface currents derived from ship drift reports is greatest between 12°N and 2°S and along the coast of Baja California (Fig. A-19). The South Equatorial Current and North Equatorial Countercurrent are strongest in September–November and weakest in March–May, while the California Current is strongest in March–May and weakest in September–November. These results are consistent with the seasonal variability of geostrophic flow inferred from surface dynamic height and thermocline depth. Note that seasonal variability of the NECC begins east of 120°W, where spring weakening appears in December–February and fall strengthening appears in June–August. Spring weakening and fall strengthening then propogate westward in March–May and September–November, respectively. Little seasonal variability in the North Equatorial Current or Peru Current is evident in the ship drift data.

Seasonal variations of surface current divergence (Fig. A-20) are difficult to interpret, except in coastal regions of high mean divergence. The clearest patterns are the winter maxima along the coast of Mexico and in the region of the Costa Rica Dome (December–February) and south of the equator off Ecuador (June–August). Seasonal variations in coastal upwelling velocity (Fig. A-21) are similar to the patterns in surface divergence. Variations along the equatorial and countercurrent divergences are more coherent in the upwelling velocity fields. Equatorial upwelling west of the Galapagos tends to be stronger in September-February and weaker in March–August. Downwelling between the SEC and NECC (along 5°N west of 110°W) is weakest in March–May and strongest in September–November.

The greatest seasonal variability in surface winds occurs between 16°N and 4°N (Fig. A-22). The ITCZ is south of 10°N in December–May, resulting in northeasterly seasonal deviations in this band. When the ITCZ is north of 10°N, in June–November, the seasonal deviations are southwesterly. As for surface currents, seasonal changes along 10°N begin east of 120°W in winter and summer, and propagate to the west in spring and fall. Moderate seasonal variability also occurs over the subtropical gyres in the northwest and southwest corners of the study region.

Seasonal variability of surface wind divergence reflects the seasonal migration of the ITCZ between 8° and 12°N (Fig. A-23). Seasonal deviations are zero along 10°N, the mean position of the ITCZ. Opposing seasonal deviations of ±1-3 $\times$ 10^{-6} s^{-1} divergence occur between the equator and 20°N. In addition to variability due to seasonal migration, convergence in the ITCZ, and divergence to the south of

the ITCZ towards the equator, is strongest in fall (September–November) and weakest in spring (March–May).

Surface wind stress in the two regional maxima north of the ITCZ and south of the equator is greatest in winter-spring and weakest in summer-fall (Fig. A-24). Seasonal variability of wind stress is greatest (± 0.3 dyne cm^{-2}) at 10–15°N, along the mean northern edge of the ITCZ. Some of the varibility here is due to seasonal movement of the ITCZ: wind stress is high in winter-spring (December–May), when the ITCZ is south of 10°N and this region is exposed to the full strength of the northeast trades, while wind stress is low in summer-fall (June–November), when the ITCZ is north of 10°N. Seasonal variability of wind stress along the equator is relatively low (± 0.1 dyne cm^{-2}), but is stronger in June–November than in December–May.

Seasonal variability of wind stress curl and Ekman pumping velocity reflect the seasonal migration of the ITCZ between 8° and 12°N (Figs. A-25, A-26). Seasonal deviations are zero along 10°N, the mean position of the ITCZ. Opposing seasonal deviations of $\pm 0.4 \times 10^{-8}$ dyne cm^{-3} wind stress curl occur within 5 degrees north and south of 10°N. The maximum curl in the ITCZ is $+0.6 \times 10^{-8}$ dyne cm^{-3}. Cyclonic (negative) wind stress curl south of the equator is weakest in December–February and strongest in June–August. Seasonal variability of Ekman pumping velocity is also affected by migration of the ITCZ, but the pattern is complicated by the strong gradient in the Coriolis parameter (f) near the equator. Coastal upwelling estimated by Ekman theory is strongest in March–May (spring) off Baja California and in June–November (winter-spring) off Ecuador and northern Peru.

Seasonal/Interannual Variability

Surface temperature variability is very low (<1°C) in Tropical and southern Subtropical Surface Water, both seasonally and interannually (Fig. A-27). Seasonal variability is low across the equator to the west of 140°W, from 15°N to 15°S. Seasonal and interannual variability are high (1–2°C) in Equatorial Surface Water, in the Peru Current, and off Baja California. High seasonal variability also occurs in northern Subtropical Surface Water north of Hawaii. Interannual variability exceeds seasonal variability in Tropical Surface Water and in Equatorial Surface Water west of 120°W, where variability on both time scales is low and mean surface temperature is high (see Fig. A-5). Seasonal variability exceeds interannual variability both in coastal Peru and California Current water and in Subtropical Surface Waters.

Mixed layer depth variability increases to the west, as does mean mixed layer depth. Variability is greatest in Subtropical Surface Water north of 20°N and south of 15°S, and along the equator west of 135°W. Seasonal variability exceeds interannual variability, except in Tropical Surface Water east of 120°W and in Equatorial Surface Water west of the Galapagos.

Variability of thermocline depth is less than the variability of mixed layer depth, especially seasonally (Fig. A-29). Thermocline depth variability is greatest, both seasonally and interannually, in Subtropical Surface Water north of 20°N. Interannual variability is low in Tropical Surface Water and higher in Equatorial Surface Water. Seasonal variability is low in a band along 17°N, corresponding to the north equatorial thermocline trough (Fig. A-6). There are three zonal bands in seasonal variability to the south of this band, most obvious to the east of 130°W: a local maximum along 12°N, a minimum along 8°N, and a maximum along 4°N. This pattern reflects the seasonal variation in the slope of the thermocline beneath the North Equatorial Countercurrent caused by opposing variations in depth of the countercurrent thermocline ridge and trough to the north and south of 8°N. Seasonal variability exceeds interannual variability only in this region and in Subtropical Surface Water north of 18°N (123–146°W).

Wind stress variability increases from east to west (Fig. A-30), as does mean wind stress (Fig. A-11). Seasonal variability is very high along 10°N west of 110°W, owing to seasonal movement of the ITCZ. Seasonal variability exceeds interannual variability by more than a factor of two in this region east of 130°W. Seasonal and interannual variability of wind stress along the equator is low compared with variability at tropical and subtropical latitudes.

Discussion

A T-S diagram of eastern tropical Pacific surface waters, using seasonal grid means, shows the principal oceanic surface water masses and eastern boundary current waters (Fig. 4). Tropical Surface Water (TSW) is the warmest, least saline water mass in the ETP. This warm water provides the energy to drive the Hadley cells (including trade winds) over the tropical ocean in both hemispheres (Bjerknes 1966). The "thermal equator" in the ETP lies north of the geographical equator, in Tropical Surface Water. Temperature of TSW varies little, either seasonally or interannually. The warm surface temperature and

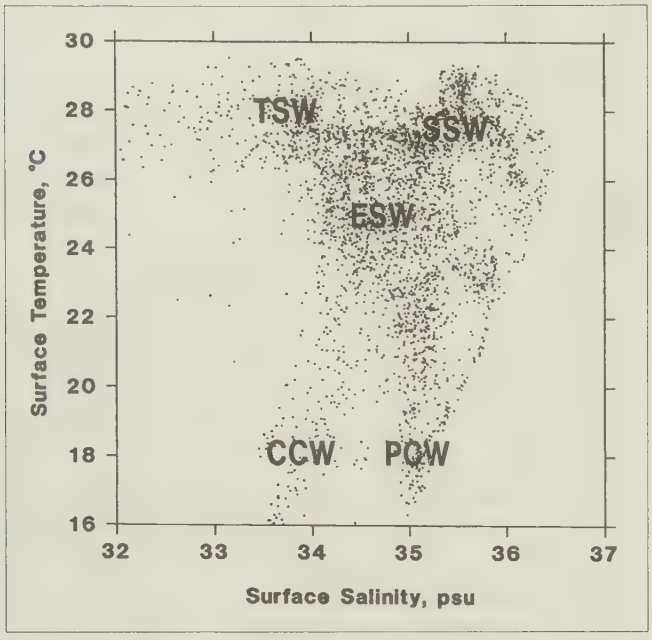

Figure 4
Surface temperature (°C) vs. surface salinity (psu) in seasonal climatologies. TSW = Tropical Surface Water; ESW = Equatorial Surface Water; SSW = Subtropical Surface Water; PCW = Peru Current Water; CCW = California Current Water (Wyrtki 1966, 1967).

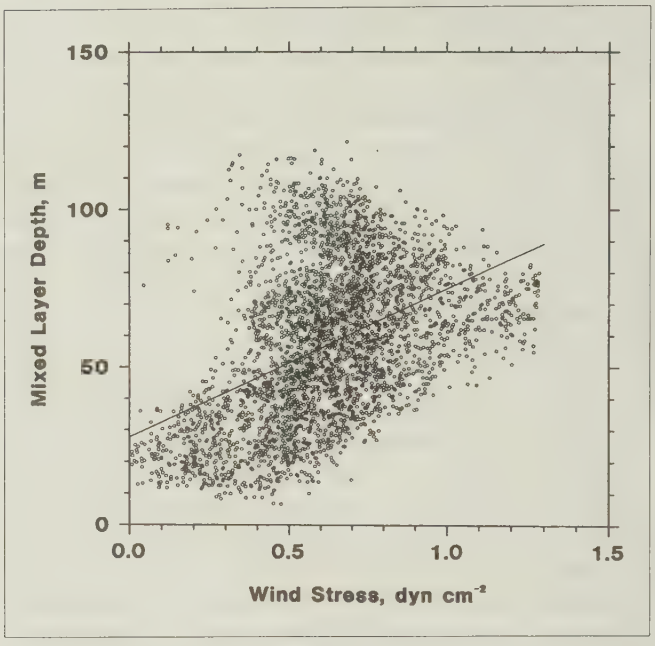

Figure 5
Mixed layer depth (m) versus wind stress (dyne cm^{-2}) in seasonal climatologies. Solid line represents linear regression (r=0.47).

low variability of TSW results in a high degree of thermal stratification and a strong, shallow thermocline. The North Equatorial Countercurrent flows eastward through the core of the TSW, beneath the Intertropical Convergence Zone (ITCZ), where the northeast and southeast tradewinds converge and westward wind stress is at a minimum.

The surface salinity minimum in Tropical Surface Water lies under the ITCZ and is most pronounced in fall. The distribution of rainfall in the tropical Pacific has a pronounced maximum at the ITCZ, with a seasonal maximum in July and August (Dorman and Bourke 1979). Surface wind convergence in the ITCZ is maximum in fall (Fig. A-23a). Rainfall and cloudiness (reduced evaporation) in this convergence produces the surface salinity minimum. The strong, shallow thermocline beneath the surface layer limits mixing of fresh water at the surface with deeper, more saline water.

Mixed layer depth is correlated with wind stress on the sea surface (r=0.47 in the seasonal climatologies, Fig. 5). Wind mixing is theoretically proportional to $(\text{wind speed})^3$ and not wind stress or $(\text{wind speed})^2$. However, log-transformation yields a linear regression exponent of 0.48 (r=0.53), meaning that mixed layer depth is proportional to $(\text{wind speed})^1$. Wind mixing cannot explain all the variability in mixed layer depth: the mixed layer is deepest at intermediate values of wind stress. This occurs at the poleward extremes of the study area, where seasonal variability of mixed layer depth (Fig. A-28) and net surface heat flux (Weare et al. 1980) is greatest. Seasonal variability of surface temperature and thermocline depth is also high in northern Subtropical Surface Water north of 20°N, presumably owing to the variability in heat flux.

Seasonal north-south shifts of the ITCZ result in local changes in the strength and direction of trade winds. Changes in local wind stress cause variations in wind-driven surface currents and in surface dynamic height and thermocline depth through local Ekman dynamics. Ekman pumping explains most of the seasonal thermocline depth variability in the ETP (Meyers 1979b; Kessler 1990). The most prominent signal is the oscillation across the NECC. Wind stress curl is positive (cyclonic) over the countercurrent thermocline ridge at 10°N, causing Ekman upwelling. Wind stress curl over the countercurrent thermocline trough at 5°N is negative (anticyclonic), causing Ekman downwelling. This north-south gradient in wind stress curl sets up the slopes in thermocline depth and surface dynamic height across the NECC. As the ITCZ migrates from its northern extreme in fall to its southern extreme in spring, the gradients in wind stress curl and Ekman pumping velocity weaken, thermocline and sea sur-

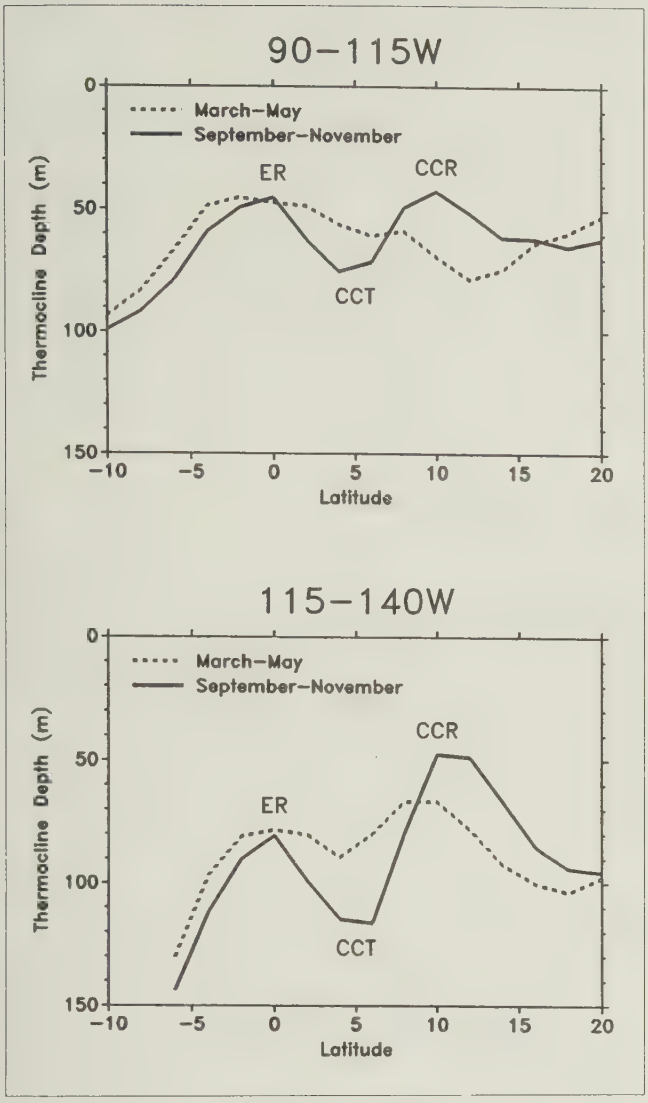

Figure 6
Seasonal average meridional profiles of thermocline (20°C isotherm) depth. ER = equatorial ridge; CCT = countercurrent trough; CCR= countercurrent ridge.

face slopes flatten, and flow of the NECC diminishes. Meridional sections of thermocline depth (Fig. 6) show this seasonal variability in thermocline slope. The slope is weaker, almost flat in spring, east of 115°W. Seasonal north-south migration of the countercurrent thermocline ridge, and to a lesser extent of the trough at 4°N, causes a meander in the NECC (Kessler and Taft 1987).

Sverdrup, Johnson, and Fleming (1942) presented evidence of surface divergence and upwelling at two sites in the equatorial current system: along the equator (equatorial divergence) and between the NECC and NEC at 10°N (countercurrent divergence). The countercurrent thermocline ridge is evidence of upwelling in the countercurrent divergence, although generally warm temperatures and low nutrient concentrations suggest that the effects of upwelling do not reach the surface (Cromwell 1953). The seasonal climatologies of surface divergence from ship drift show that divergence is weak and discontinuous in the countercurrent divergence, compared to the equatorial divergence. Upwelling rates are 0.5–2.0 $\times$ 10^{-3} cm s^{-1} along the equator, but generally <0.2 $\times$ 10^{-3} cm s^{-1} in the countercurrent divergence (up to 0.6 $\times$ 10^{-3} cm s^{1} at the Costa Rica Dome in winter).

Ekman theory gives upwelling rates of about 0.1 $\times$ 10^{-3} cm s^{-1} due to cyclonic wind stress curl along 10°N, with a peak of 0.2 $\times$ 10^{-3} cm s^{-1} in winter at the Costa Rica Dome, compared to coastal upwelling rates off Peru and Ecuador of >0.5 cm s^{-1}. Estimates of vertical velocities at the base of the mixed layer along the equator in the eastern Pacific, from indirect measurement (Halpern et al. 1989), mass budgets (Wyrtki 1981; Quay et al. 1983), and three-dimensional general circulation models (Bryden and Brady 1985; Philander et al. 1987), range between 0.3 and 5.0 $\times$ 10^{-3} cm s^{-1}. Thus, upwelling rates in the countercurrent divergence along 10°N average about 10% (never more than 25%) of equatorial or coastal upwelling rates in the ETP.

Equatorial Surface Water (ESW) is the coldest oceanic water mass in the ETP (Fig. 4). Surface temperature variability is high, both seasonally and interannually, in these waters. Interannual variability of thermocline depth is also high. However, variability of local wind stress is low, indicating remote forcing. El Niño – Southern Oscillation (ENSO) variability in zonal wind stress in the central and western equatorial Pacific, and the resulting sea surface and thermocline slopes along the equator, cause interannual variability in the temperature and thickness of Equatorial Surface Water (Wyrtki 1985).

Seasonal variability of the temperature of ESW is only partially related to wind-driven upwelling and its effects on thermocline depth. The equatorial thermocline shoals in March-May when wind stress is low, zonal sea surface slope is reduced, and ESW is warmest. Conflicting theories suggest that the average state of the ESW cold tongue is maintained either by equatorial upwelling and advection of cold water from the Peru Current by the SEC (Wyrtki 1981) or by the eastward advection of cold water by the Equatorial Undercurrent as it rises to the surface near 95°W (Bryden and Brady 1985). Whichever mechanism may be correct for the average state, advection of water by the SEC may play an important role in variations of surface temperature in the cold tongue. Observations show that seasonal temperature variations are larger near the coast (Fig. A-27) and that the phase of the variations propagates westward from

the coast (Horel 1982). For example, the coldest surface temperature relative to the annual mean occurs in August-September near the coast and in November at 140°W (Horel 1982).

The South Equatorial Current (especially north of the equator) and North Equatorial Countercurrent vary synchronously in the ETP. Both currents are weak, or even absent, in spring and strong in fall (Fig. A-19). This is consistent with earlier analyses of ship drift (Wyrtki 1966) and dynamic topography (Wyrtki 1975). In the central Pacific, however, the NECC varies in phase with the North Equatorial Current and in opposition to the SEC (Wyrtki 1974; Kessler and Taft 1987). Here, the NECC does not peak until December (Wyrtki 1974), consistent with the westward propagation of seasonal change in surface winds and surface currents observed in the ETP. The westward propagation of seasonal deviations (change of phase in the annual cycle) of surface winds in the ITCZ seen in Fig. A-22b was also observed by Horel (1982).

Eastern boundary currents also vary seasonally in the ETP. Along the coast of Baja California, equatorward winds are strong in spring (March–May) and weak in fall (September–November, Fig. A-22). Weaker offshore Ekman transport of surface water in fall reduces the zonal slope of the sea surface adjacent to the coast (Fig. A-18). Therefore, the California Current is strong in spring and weak in fall (Fig. A-19). Northeast trade winds blowing across southern Mexico and Central America are strongest in winter (December–February, Fig. A-22). These winds drive coastal upwelling, especially in the Gulf of Tehuantepec at 15°N, 95°W (McCreary et al. 1989), where the winter surface temperature deviation is <–1°C. In contrast, the variability of winds and surface currents in the Peru Current is very low in the seasonal climatologies.

Interannual variability in the ETP is analogous, in some respects, to seasonal variability (Philander 1989). When the southeast trade winds are weak (March–April or El Niño years), the South Equatorial Current is weak, the equatorial thermocline slope is flatter, and Equatorial Surface Water is warm. When the southeast trades are strong (September–October or La Niña years), the South Equatorial Current is strong, the equatorial thermocline slope is steeper, and Equatorial Surface Water is cold. A zonal redistribution of surface waters occurs on both time scales. Interannual variability of the North Equatorial Countercurrent, however, is not analogous to seasonal variability. During El Niño, when the southeast trades are weak, the NECC intensifies out of phase with the weakened SEC. The resulting eastward transport of warm waters causes warming and thermocline depression in both the Tropical and Equatorial Surface Water masses of the ETP.

In general, seasonal variability of physical oceanographic variables in the eastern tropical Pacific Ocean is comparable, in magnitude and relationships among most variables, to interannual variability associated with the El Niño-Southern Oscillation. Patterns and magnitude of environmental variability differ significantly among surface water masses, and thus among biological habitats. These results should be considered in studies of biological responses of populations and ecosystems to environmental variability in this important region of the world's oceans.

Acknowledgments

I thank James Stricherz and James O'Brien of Florida State University for providing the gridded wind data, Craig Nelson of NOAA/Center for Ocean Analysis and Prediction for providing ship drift data, Norman Hall of NOAA/NOS/National Ocean Data Center for assistance with data, and Dave Behringer of NOAA/NWS/Climate Analysis Center for advice and software.

Citations

Barber, R.T. and F.P. Chavez.
1986. Ocean variability in relation to living resources during the 1982–83 El Niño. Nature 319:279–285.

Bjerknes, J.
1966. A possible response of the atmospheric Hadley circulation to equatorial anomalies of ocean temperature. Tellus 4:820–829.

Blackburn, M., R.M. Laurs, R.W. Owen, and B. Zeitschel.
1970. Seasonal and areal changes in standing stocks of phytoplankton, zooplankton and micronekton in the eastern tropical Pacific. Mar. Biol. 7:14–31.

Bryden, H.L., and E.C. Brady.
1985. Diagnostic model of the three-dimensional circulation in the upper equatorial Pacific Ocean. J. Phys. Oceanogr. 15:1255–1273.

Cromwell, T.
1953. Circulation in a meridional plane in the central equatorial Pacific. J. Mar. Res. 12:196–213.
1958. Thermocline topography, horizontal currents, and "ridging" in the eastern tropical Pacific. Bull. Inter-American Tropical Tuna Commission 111:135–164.

Donguy, J.R., and G. Meyers.
1987. Observed and modelled topography of the 20°C isotherm in the tropical Pacific. Oceanol. Acta 10:41–48.

Dorman, C.E., and R.H. Bourke.
1979. Precipitation over the Pacific Ocean, 30°S to 60°N. Mon. Weather Rev. 107:896–910.

Enfield, D.B.
1989. El Niño, past and present. Rev. Geophys. 27:159–187.

Halpern, D., R.A. Knox, D.S. Luther, and S.G.H. Philander.
1989. Estimates of equatorial upwelling between 140° and 110°W during 1984. J. Geophys. Res. 94:8018–8020.

Heinrich, A.K.
1962. The life histories of plankton animals and seasonal cycles of plankton communities in the oceans. J. Cons. Perm. Intern. Explor. Mer 27:15–24.

Hickey, B.
1975. The relationship between fluctuations in sea level, wind stress and sea surface temperature in the equatorial Pacific. J. Phys. Oceanogr. 5:460–475.

Hofmann, E.E., A.J. Busalacchi, and J.J. O'Brien.
1981. Wind generation of the Costa Rica Dome. Science 214:552–554.

Horel, J.D.
1982. On the annual cycle of the tropical Pacific atmosphere and ocean. Mon. Weather Rev. 110:1863–1878.

Kessler, W.S.
1990. Observations of long Rossby waves in the northern tropical Pacific. J. Geophys. Res. 95:5183–5217.

Kessler, W.S., and B.A. Taft.
1987. Dynamic heights and zonal geostrophic transports in the central tropical Pacific during 1979–1984. J. Phys. Oceanogr. 17:97–122.

Legler, D.M., and J.J. O'Brien.
1988. Tropical Pacific wind stress analysis for TOGA. *In* Time series of ocean measurements, vol. 4., 11–18 IOC Tech. Ser. 33, UNESCO, Paris.

Levitus, S.
1982. Climatological atlas of the world ocean. NOAA Professional Paper No. 13, 173 p.

McCreary, J.P., H.S. Lee, and D.B. Enfield.
1989. The response of the coastal ocean to strong offshore winds: with application to circulations in the Gulfs of Tehuantepec and Papagayo. J. Mar. Res. 47:81–109.

McPhaden, M.J., D.V. Hansen, and P.L. Richardson.
1991. A comparison of ship drift, drifting buoy, and current meter mooring velocities in the Pacific South Equatorial Current. J. Geophys. Res. 96:775–781.

Meehl, G.A.
1982. Characteristics of surface current flow inferred from a global ocean current data set. J. Phys. Oceanogr. 12:538–555.

Meyers, G.
1979a. Annual variation in the slope of the 14°C isotherm along the equator in the Pacific Ocean. J. Phys. Oceanogr. 9:885–891.
1979b. On the annual Rossby wave in the tropical North Pacific Ocean. J. Phys. Oceanogr. 9:663–674.

Oort, A.H.
1983. Global atmospheric circulation statistics, 1958–1973. NOAA Professional Paper No. 14, 180 p.

Owen, R.W., and B. Zeitschel.
1970. Phytoplankton production: seasonal change in the oceanic eastern tropical Pacific. Mar. Biol. 7:32–36.

Philander, S.G.H., W.J. Hurlin, and A.D. Seigel.
1987. Simulation of the seasonal cycle of the tropical Pacific Ocean. J. Phys. Oceanogr. 17:1986–2002.
1989. El Niño, La Niña, and the Southern Oscillation. Acad. Press, 293 p.

Picaut, J., S.P. Hayes, and M.J. McPhaden.
1989. Use of the geostrophic approximation to estimate time-varying zonal currents at the equator. J. Geophys. Res. 94:3228–3236.

Quay, P.D., M. Stuiver, and W.S. Broecker.
1983. Upwelling rates for the equatorial Pacific Ocean derived from the bomb ^{14}C distribution. J. Mar. Res. 41:769–792.

Rebert, J.P., J.R. Donguy, G. Eldin, and K. Wyrtki.
1985. Relations between sea level, thermocline depth, heat content, and dynamic height in the tropical Pacific Ocean. J. Geophys. Res. 90:11,719–11,725.

Reilly, S.B.
1990. Seasonal changes in distribution and habitat differences among dolphins in the eastern tropical Pacific. Mar. Ecol. Prog. Ser. 66:1–11.

Richardson, P.L.
1989. Worldwide ship drift distributions identify missing data. J. Geophys. Res. 94:6169–6176.

Sournia, A.
1969. Cycle annuel du phytoplancton et de la production primaire dans les mers tropicales. Mar. Biol. 3:287–303.

Sverdrup, H.U., M.W. Johnson, and R.H. Fleming.
1942. The oceans: their physics, chemistry, and general biology. Prentice-Hall, 1087 p.

Topoly, P.J., P.R. Hadsell, and R.J. Abram.
1989. National Oceanographic Data Center experimental CD-ROM NODC-01: Pacific Ocean temperature and salinity profiles. NODC Informal Report No. 10, 22 p.

Tsuchiya, M.
1974. Variation of the surface geostrophic flow in the eastern intertropical Pacific Ocean. Fish. Bull., U.S. 72:1075–1086.

Walsh, J.J.
1978. The biological consequences of interaction of the climatic, El Niño, and event scales of variability in the eastern tropical Pacific. Rapp. P.-v. Réun. Cons. int. Explor. Mer 173L:182–192.

Weare, B.C., P.T. Strub, and M.D. Samuel.
1980. Marine climate atlas of the tropical Pacific Ocean. Univ. California, Davis, 147 p.

Wyrtki, K.
1964. Upwelling in the Costa Rica Dome. Fish. Bull., U.S. 63:355–372.
1966. Oceanography of the eastern equatorial Pacific Ocean. Oceanogr. Mar. Biol. Ann. Rev. 4:33–68.
1967. Circulation and water masses in the eastern equatorial Pacific Ocean. Int. J. Oceanol. Limnol. 1:117–147.
1974. Equatorial currents in the Pacific 1950 to 1970 and their relations to trade winds. J. of Phys. Oceanogr. 4:372–380.
1975. Fluctuations of the dynamic topography in the Pacific Ocean. J. Phys. Oceanogr. 5:450–459.
1981. An estimate of equatorial upwelling in the Pacific. J. Phys. Oceanogr. 11:1205–1214.
1985. Water displacements in the Pacific and the genesis of El Niño cycles. J. Geophys. Res. 90:7129–7132.

Appendix

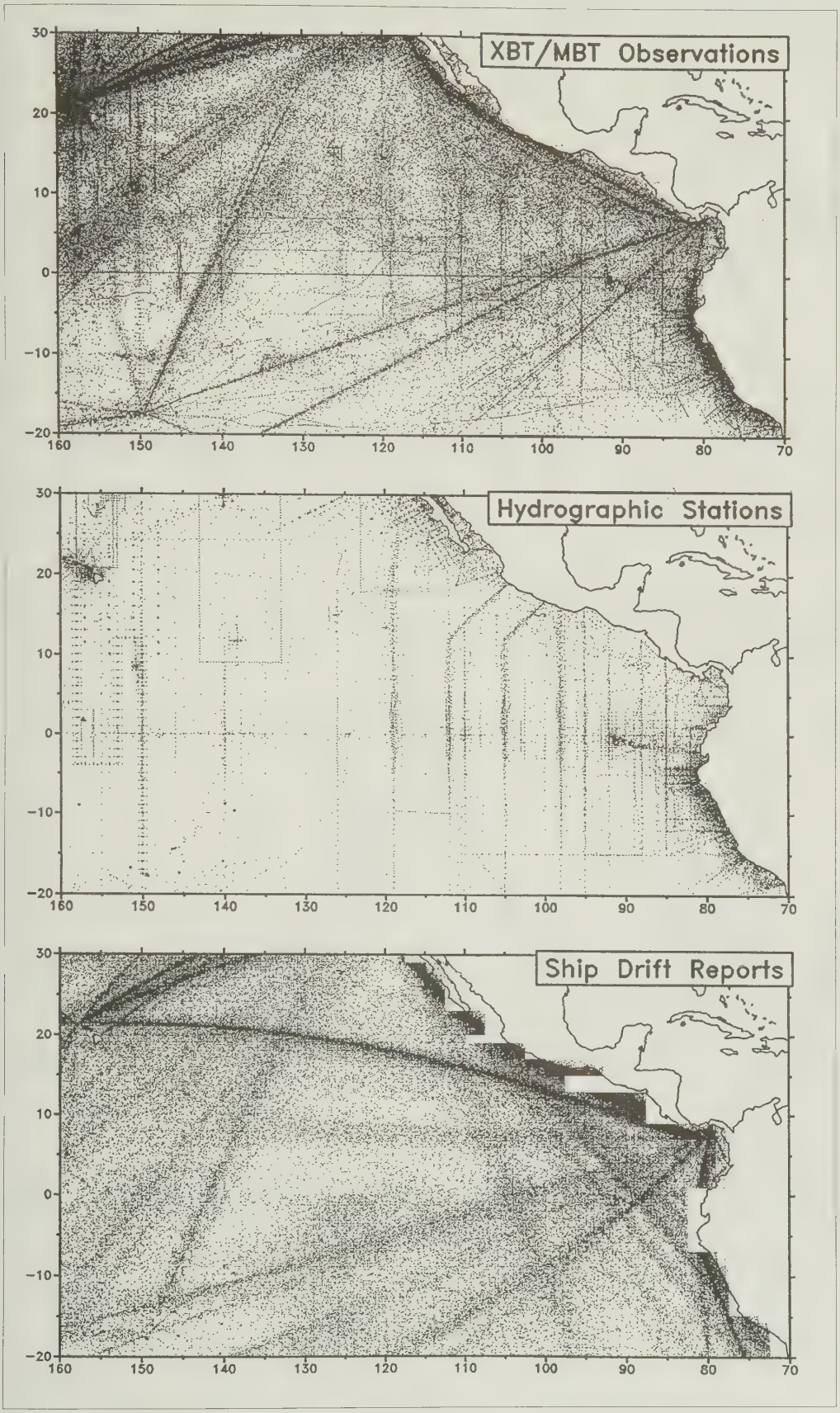

Figure A-1
(Top) XBT and MBT (bathythermograph) observations, 1960–1990, in combined PMEL (Kessler 1990) and NODC data set, $n = 137{,}867$. **(Middle)** hydrographic stations (bottle cast and STD), 1960-1988, in NODC data set, $n = 26{,}149$. **(Bottom)** ship drift reports, 1900-1969, $n = 229{,}782$.

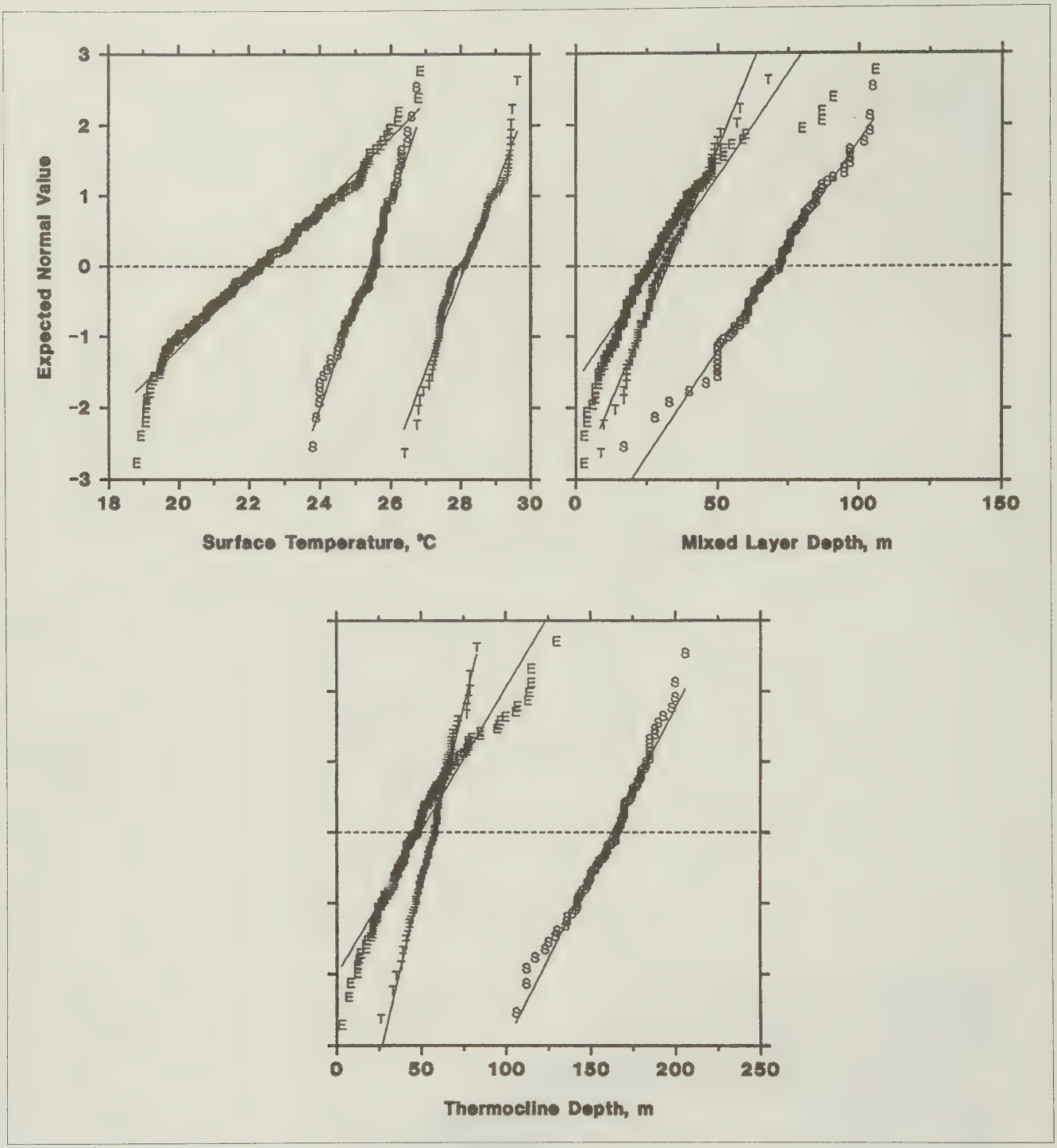

Figure A-2a

Normal probability plots of surface temperature, mixed layer depth, and thermocline depth at representative grid points in September–November: E = Equatorial (0°N,100°W); T = Tropical (10°N,110°W); and S = Subtropical (20°N,150°W). Local grid resolution = 2 degrees.

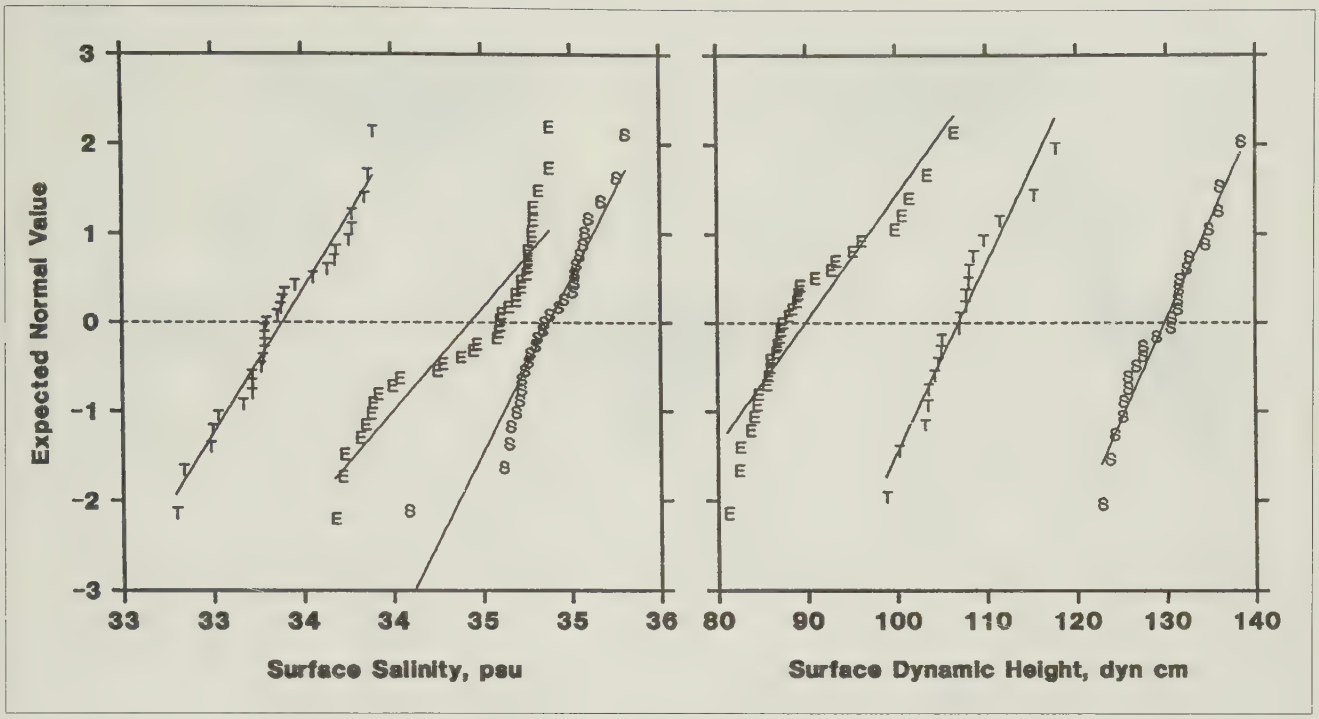

Figure A-2b

Normal probability plots of surface salinity and surface dynamic height (0/500db) at representative grid points in September–November: E = Equatorial (0°N,100°W); T = Tropical (10°N,110°W); and S = Subtropical (20°N,150°W). Local grid resolution for surface salinity = 3 degrees. Local grid resolution for surface dynamic height = 4(E), 6(T), and 3(S) degrees.

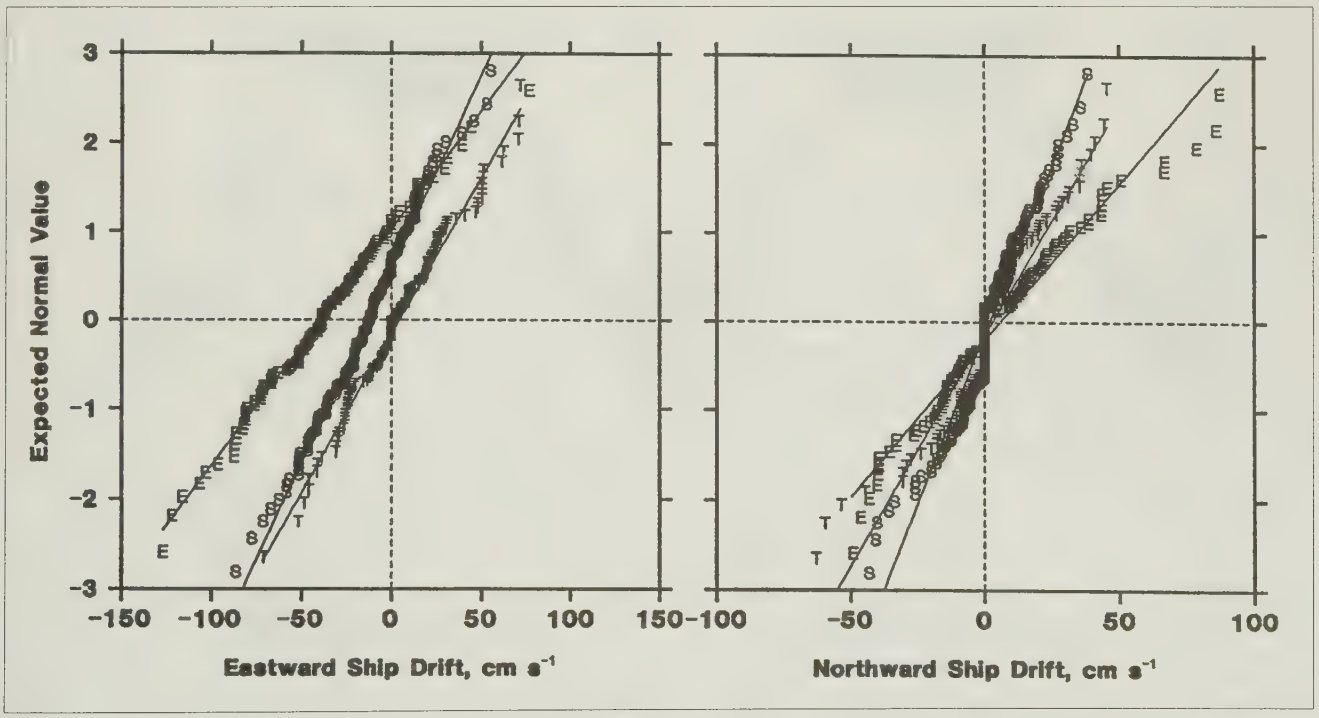

Figure A-2c

Normal probability plots of ship drift at representative grid points in September-November: E = Equatorial (0°N,100°W); T = Tropical (10°N,110°W); and S = Subtropical (20°N,150°W). Local grid resolution = 3(E), 5(T), and 2(S) degrees longitude.

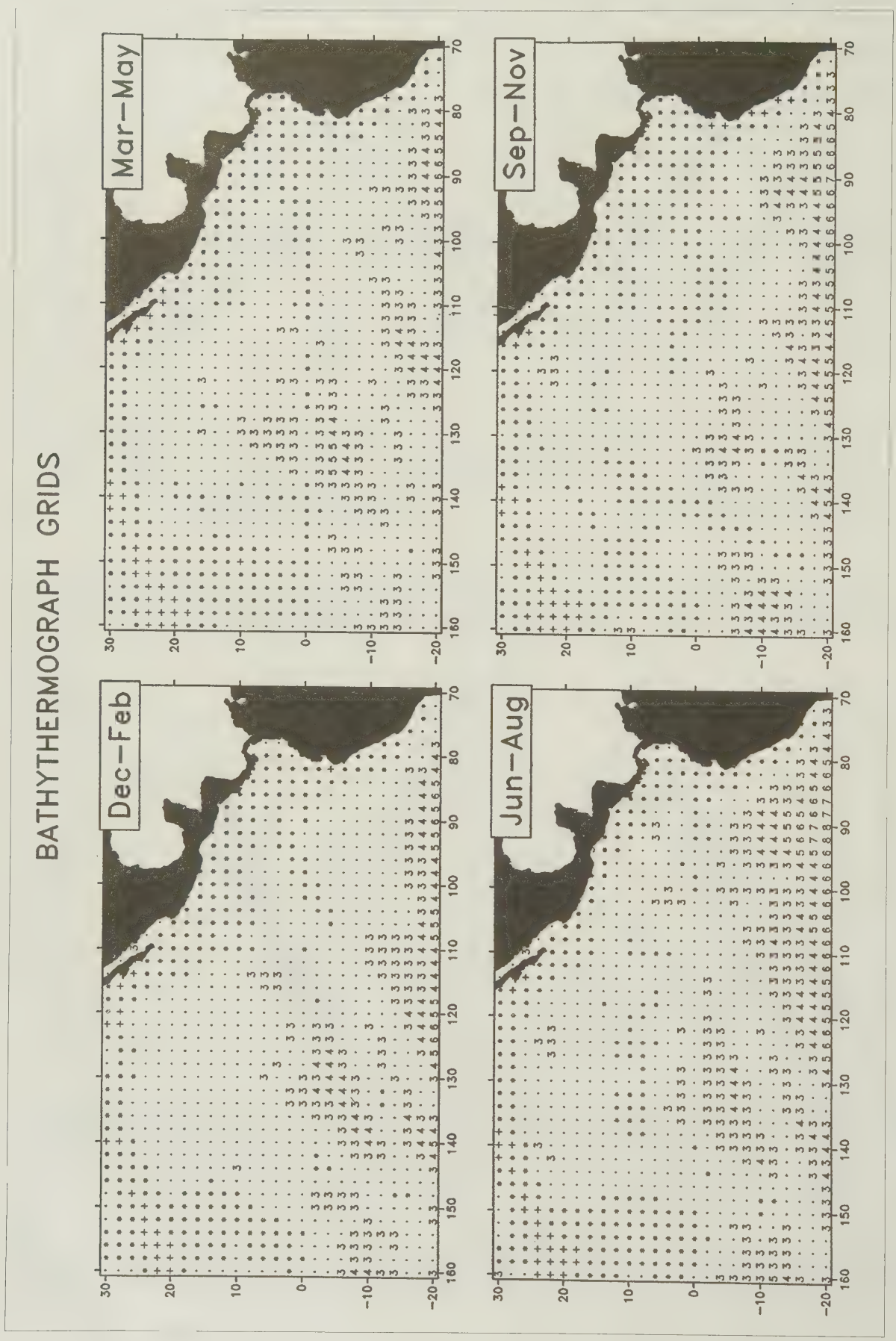

Figure A-3a

Grid sample size and local resolution for bathythermograph data (surface temperature, mixed layer depth and thermocline depth). For grid points with sufficient observations within a radius of 2 degrees: $n \geq 20$ (·), ≥ 100 (*), or $n \geq 500$ (+). For grid points with <20 observations within a radius of 2 degrees, number equals radius in degrees within which $n \geq 20$.

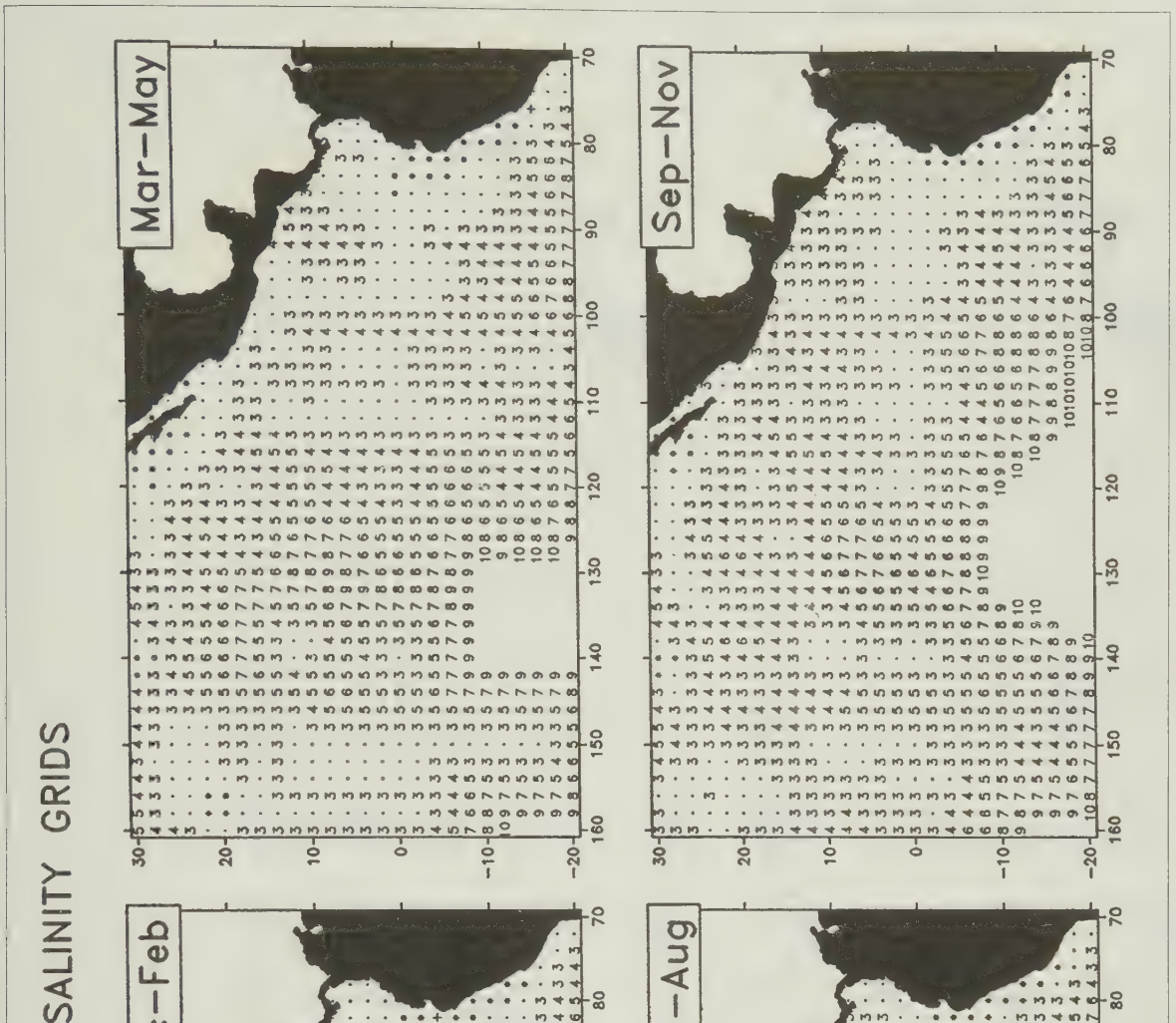

Figure A-3b

Grid sample size and local resolution for surface salinity data. For grid points with sufficient observations within a radius of 2 degrees: $n \geq 20$ (·) or $n \geq 100$ (*). For grid points with <20 observations within a radius of 2 degrees, number equals radius in degrees within which $n \geq 20$. Missing grid points had insufficient observations within a radius of 10 degrees.

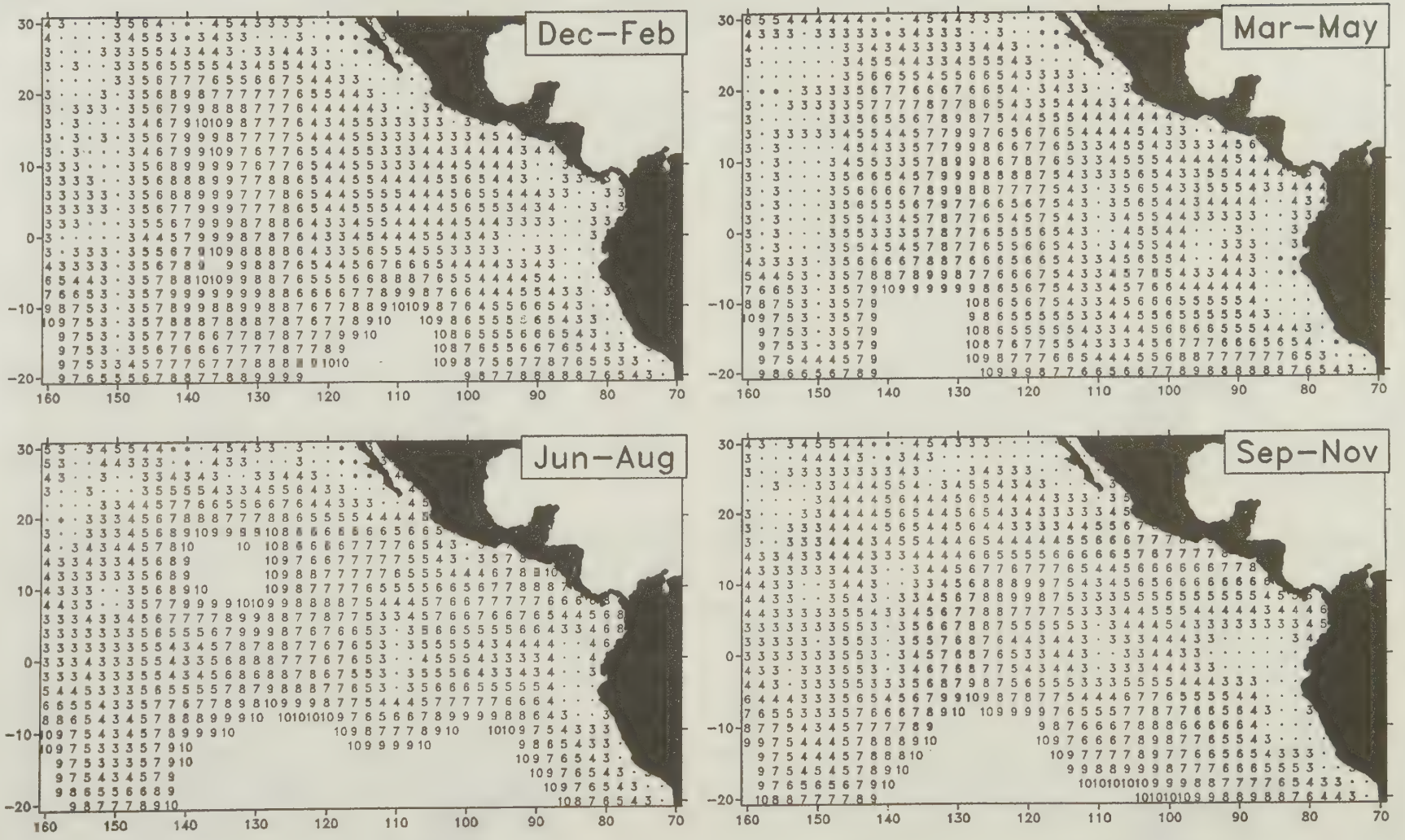

Figure A-3c

Grid sample size and local resolution for surface dynamic height data. For grid points with sufficient observations within a radius of 2 degrees: $n \geq 20$ (·) or $n \geq 100$ (*). For grid points with <20 observations within a radius of 2 degrees, number equals radius in degrees within which $n \geq 20$. Missing grid points had insufficient observations within a radius of 10 degrees.

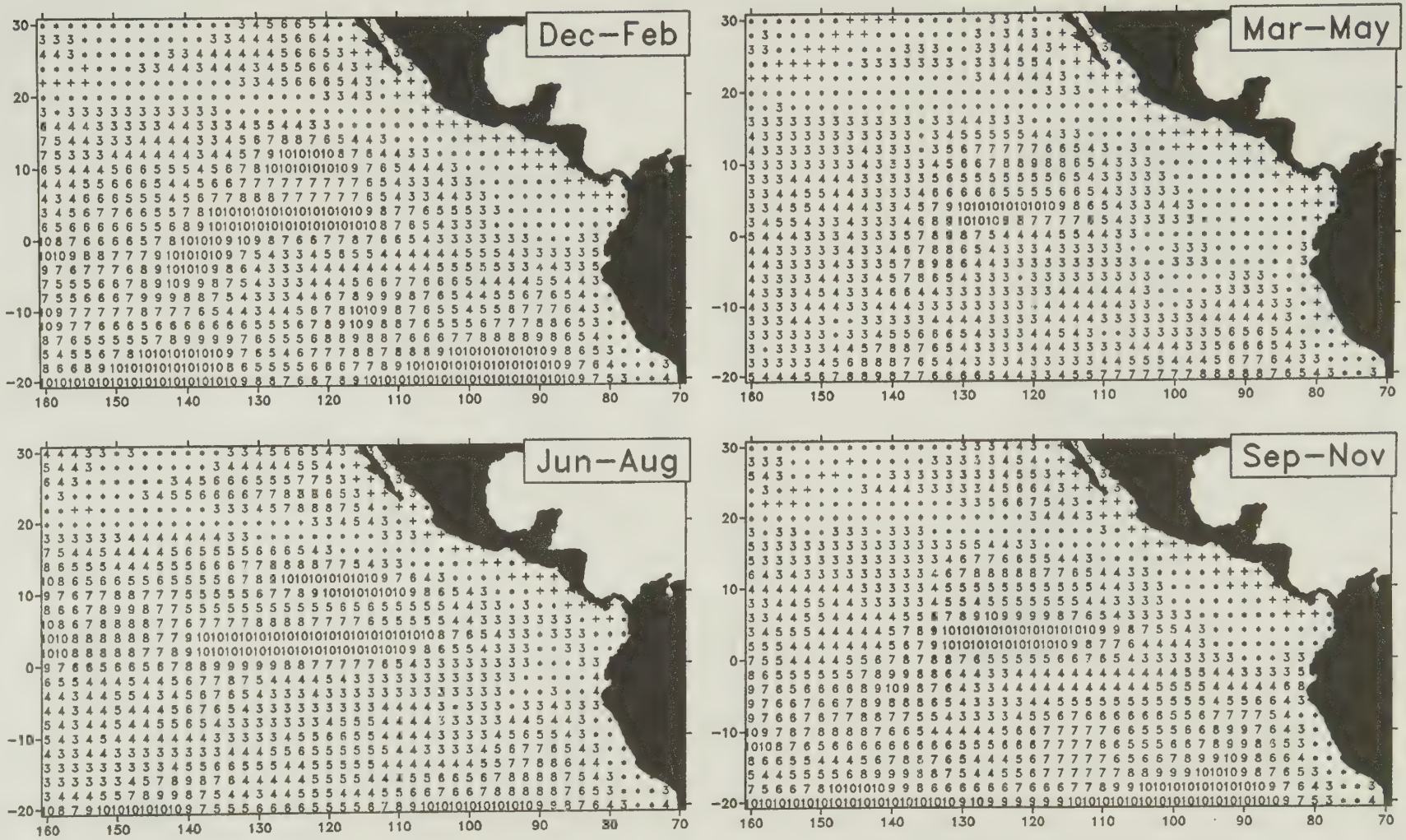

Figure A-3d

Grid sample size and local resolution for ship drift data. For grid points with sufficient observations within a radius of 2 degrees: $n \geq 100$ (*) or $n \geq 500$ (+). For grid points with <100 observations within a radius of 2 degrees, number equals degrees of longitude within which $n \geq 100$.

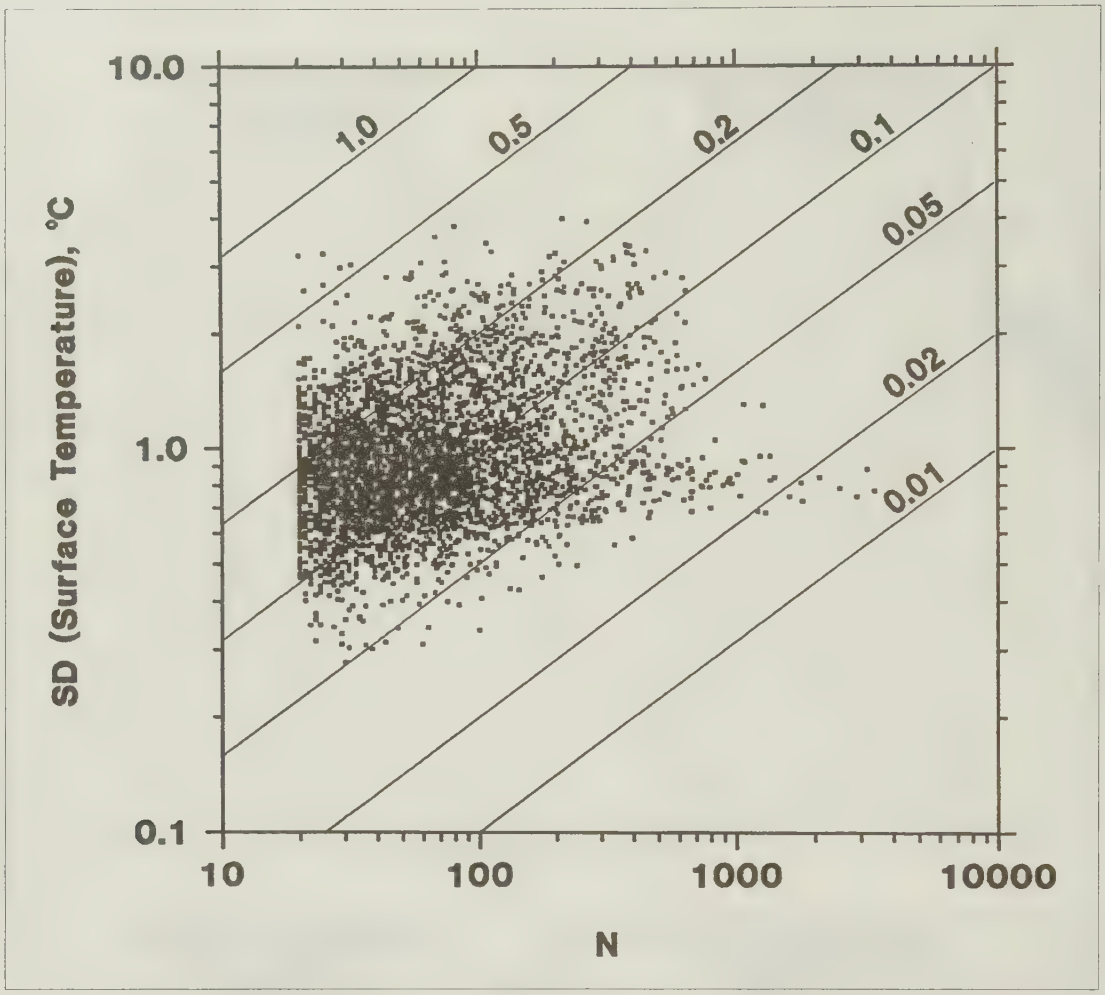

Figure A-4a
Standard deviation (SD) versus sample size (N) in seasonal grids of surface temperature. Solid lines represent corresponding standard errors ($SD/\sqrt{N}$) of the grid means.

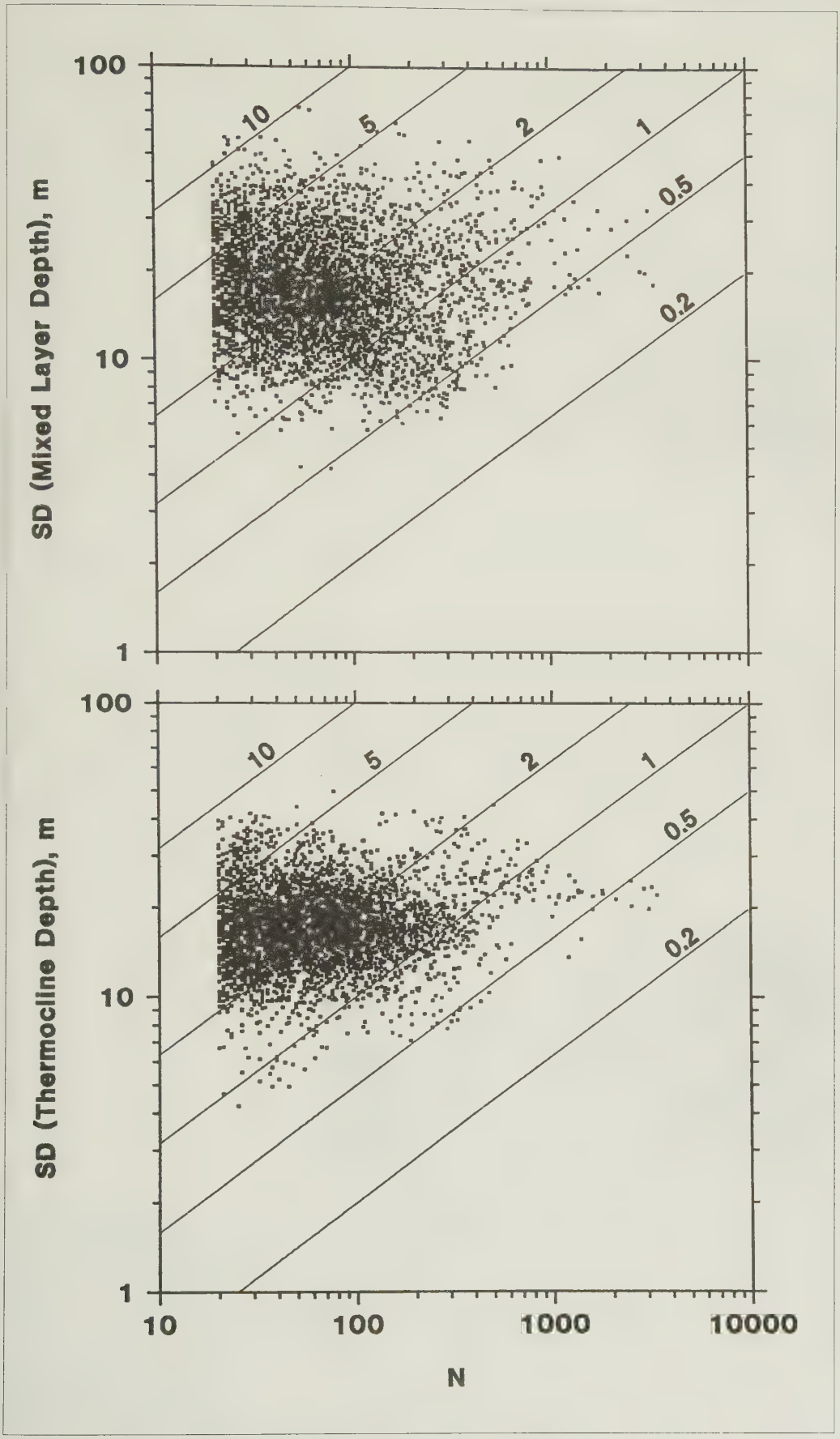

Figure A-4b
Standard deviation (SD) versus sample size (N) in seasonal grids of mixed layer depth (**top**) and thermocline depth (**bottom**). Solid lines represent corresponding standard errors ($SD/\sqrt{N}$) of the grid means.

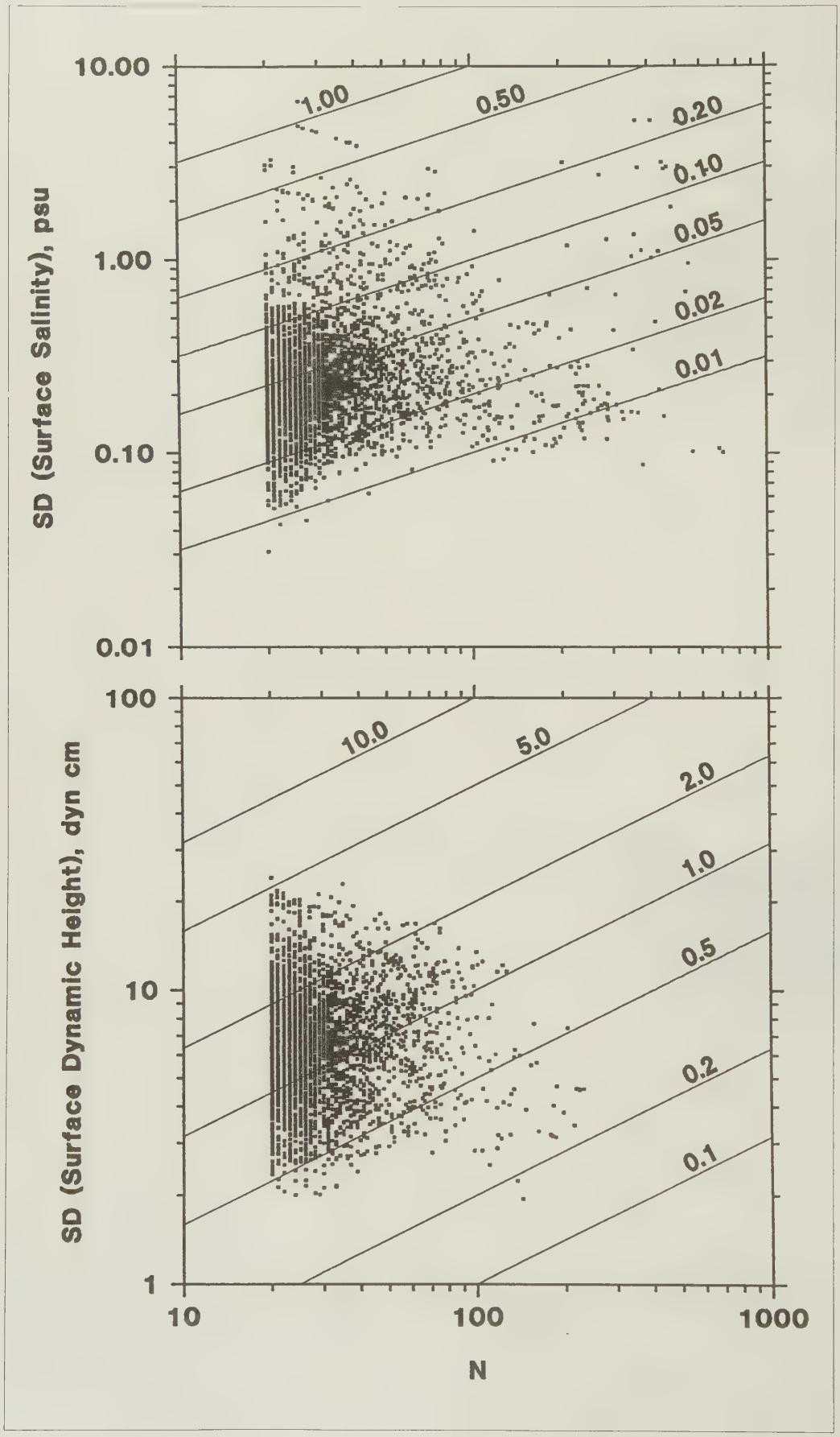

Figure A-4c
Standard deviation (SD) versus sample size (N) in seasonal grids of surface salinity (**top**) and surface dynamic height (0/500db, **bottom**). Solid lines represent corresponding standard errors ($SD/\sqrt{N}$) of the grid means.

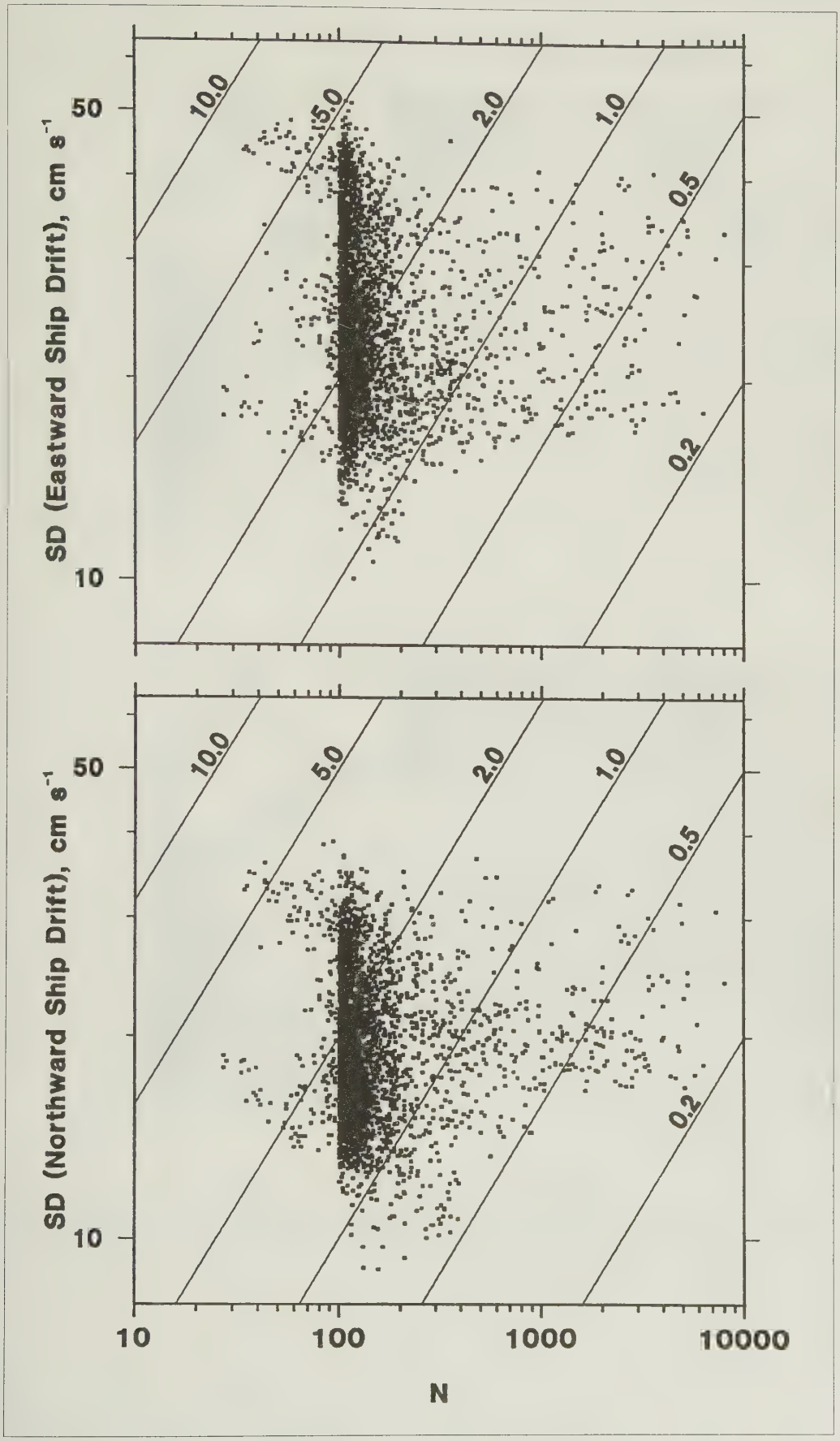

Figure A-4d
Standard deviation (SD) versus sample size (N) in seasonal grids of ship drift. Solid lines represent corresponding standard errors ($SD/\sqrt{N}$) of the grid means.

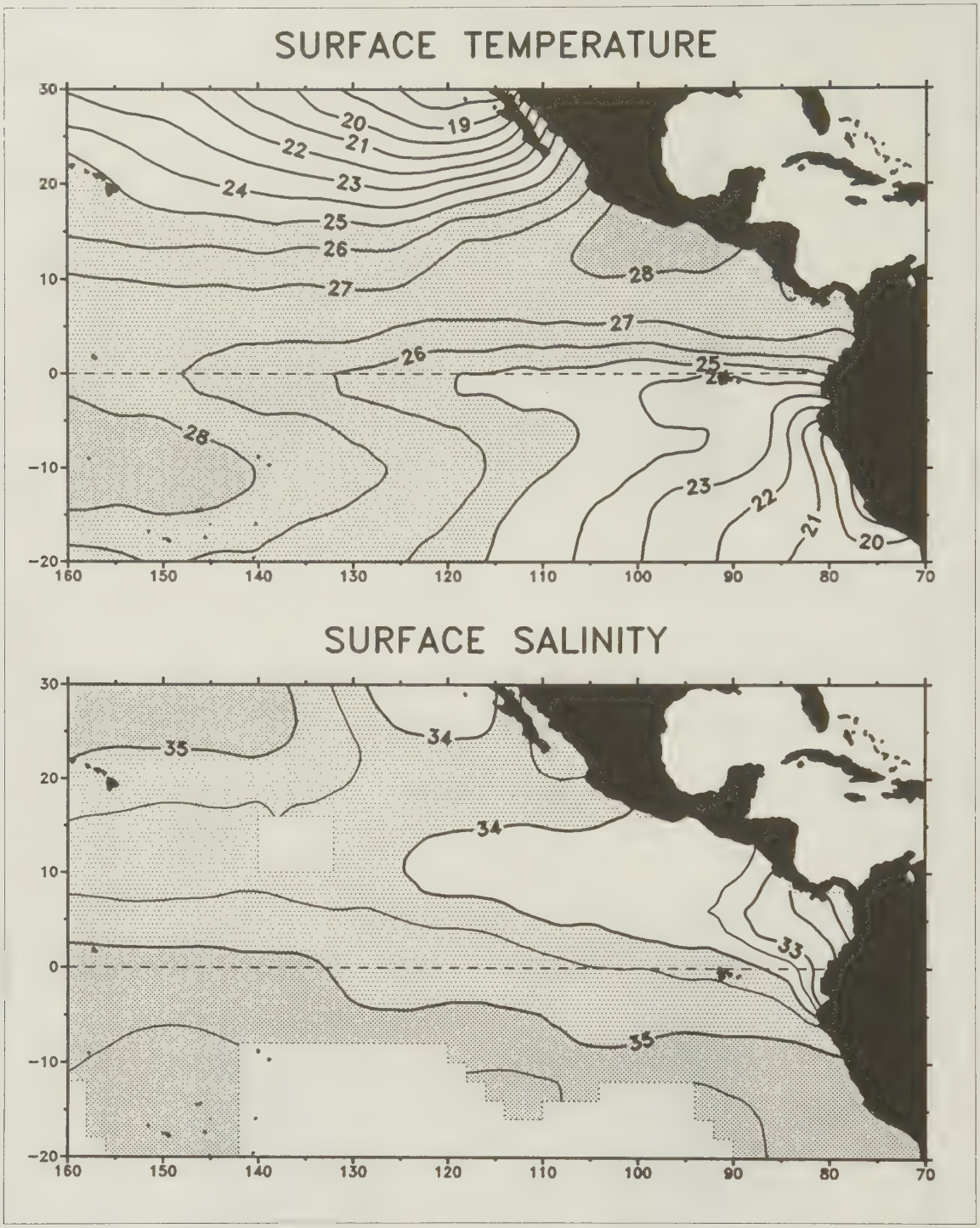

Figure A-5
Annual climatologies of surface temperature (°C), from 1960–1990 bathythermograph data, and surface salinity (psu), from 1960–1988 hydrographic data.

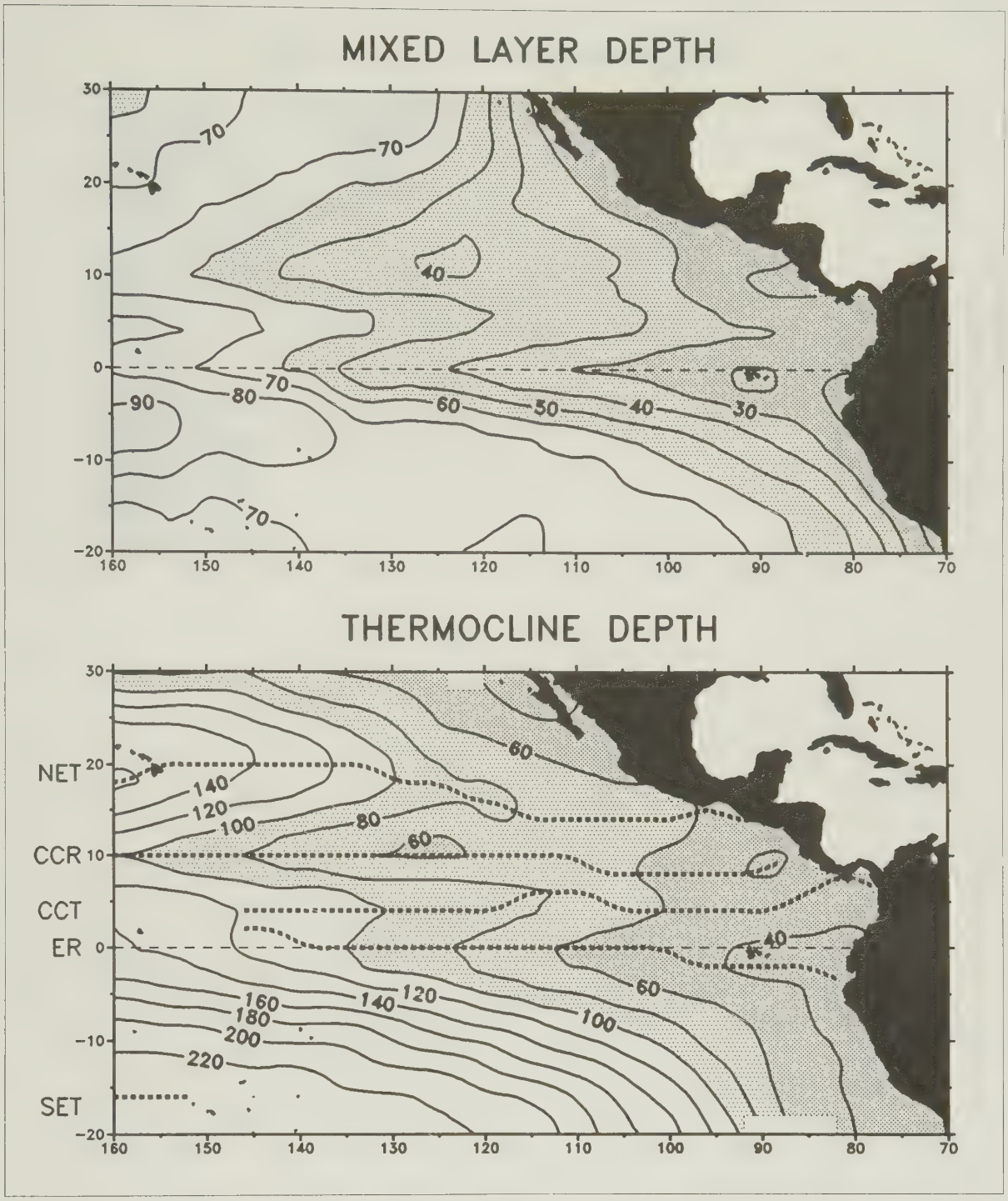

Figure A-6

Annual climatologies of mixed layer depth (m) and thermocline depth (20°C isotherm depth, m), from 1960–1990 bathythermograph data. For thermocline depth, NET = North Equatorial Trough; CCR = Countercurrent Ridge; CCT = Countercurrent Trough; ER = Equatorial Ridge; SET = South Equatorial Trough.

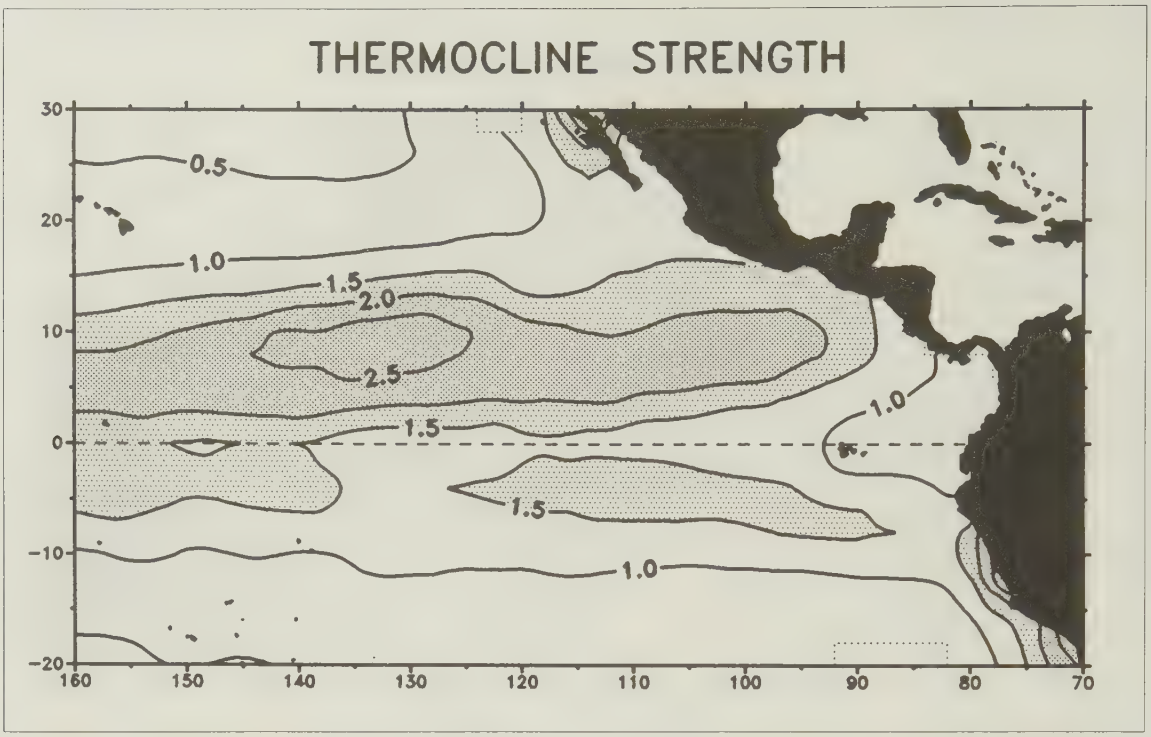

Figure A-7
Annual climatology of thermocline strength (°C $10m^{-1}$ between 20° and 15°C isotherms), derived from 1960–1990 bathythermograph data.

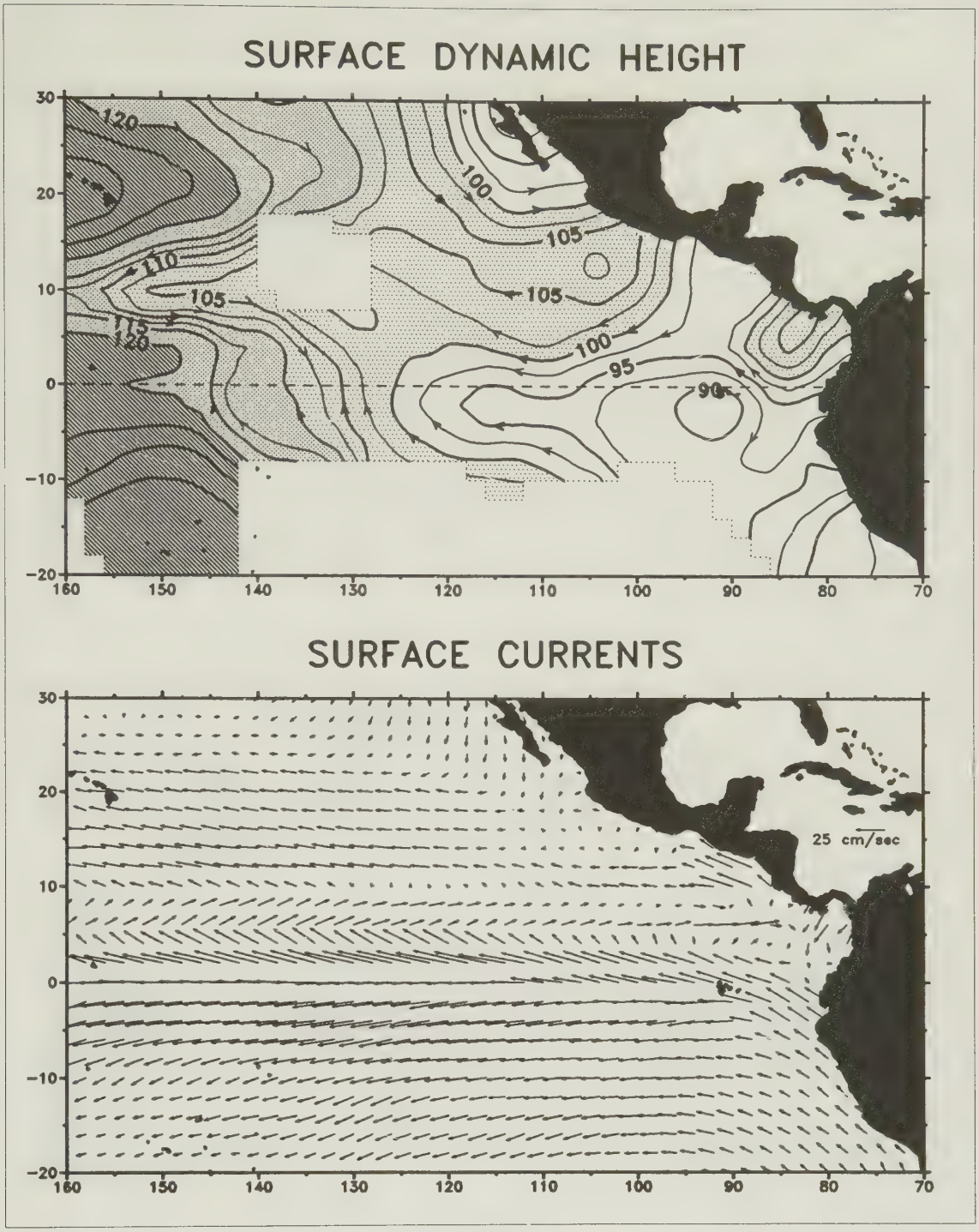

Figure A-8

Annual climatologies of surface dynamic height (relative to 500 db, dyn cm), from 1960–1988 hydrographic data, and surface current velocity, from 1900–1969 ship drift reports.

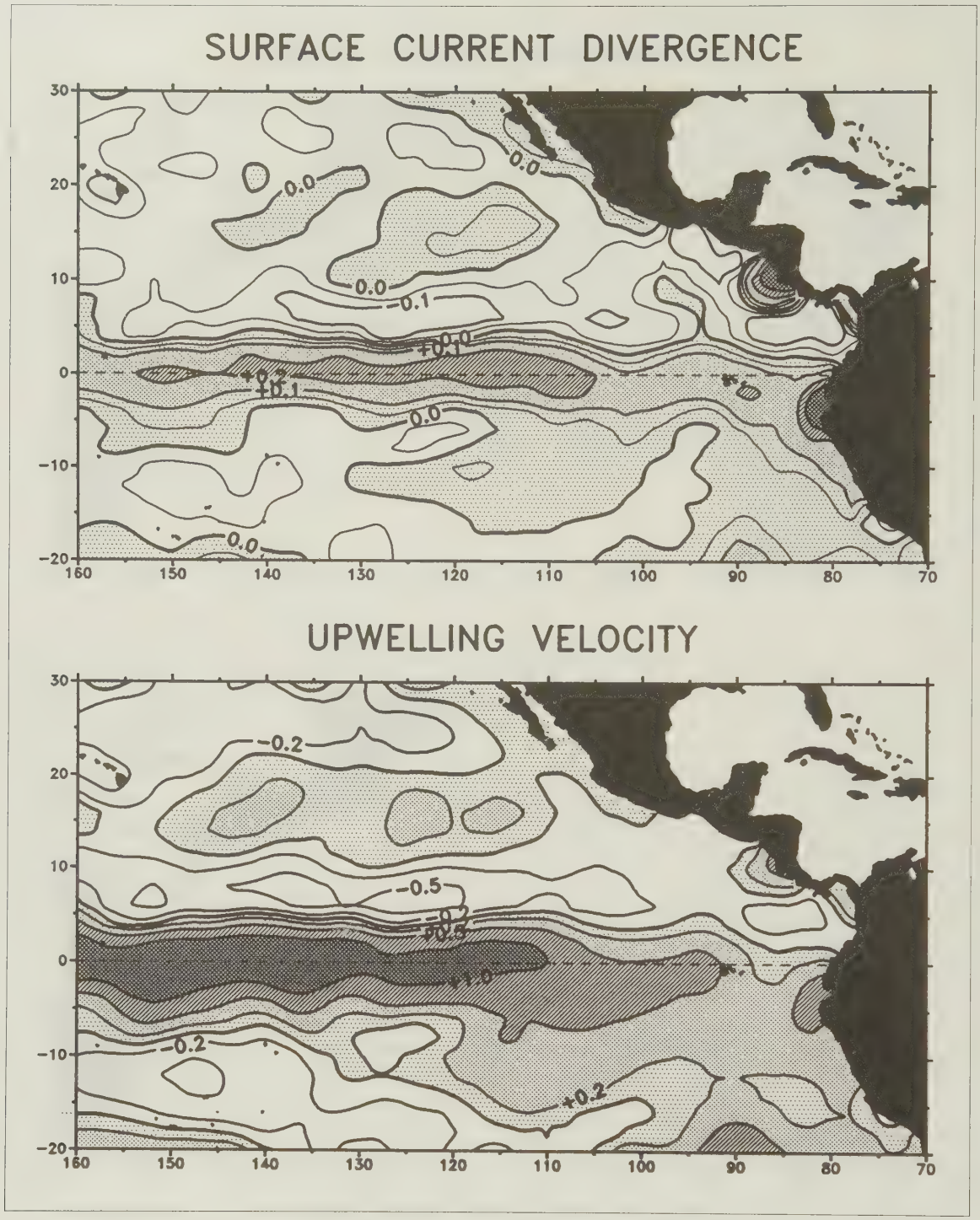

Figure A-9

Annual climatologies of surface current divergence (10^{-6} s^{-1}), derived from 1900–1969 ship drift reports, and upwelling velocity (10^{-3} cm s^{-1}), calculated from divergence of horizontal transports in the mixed layer.

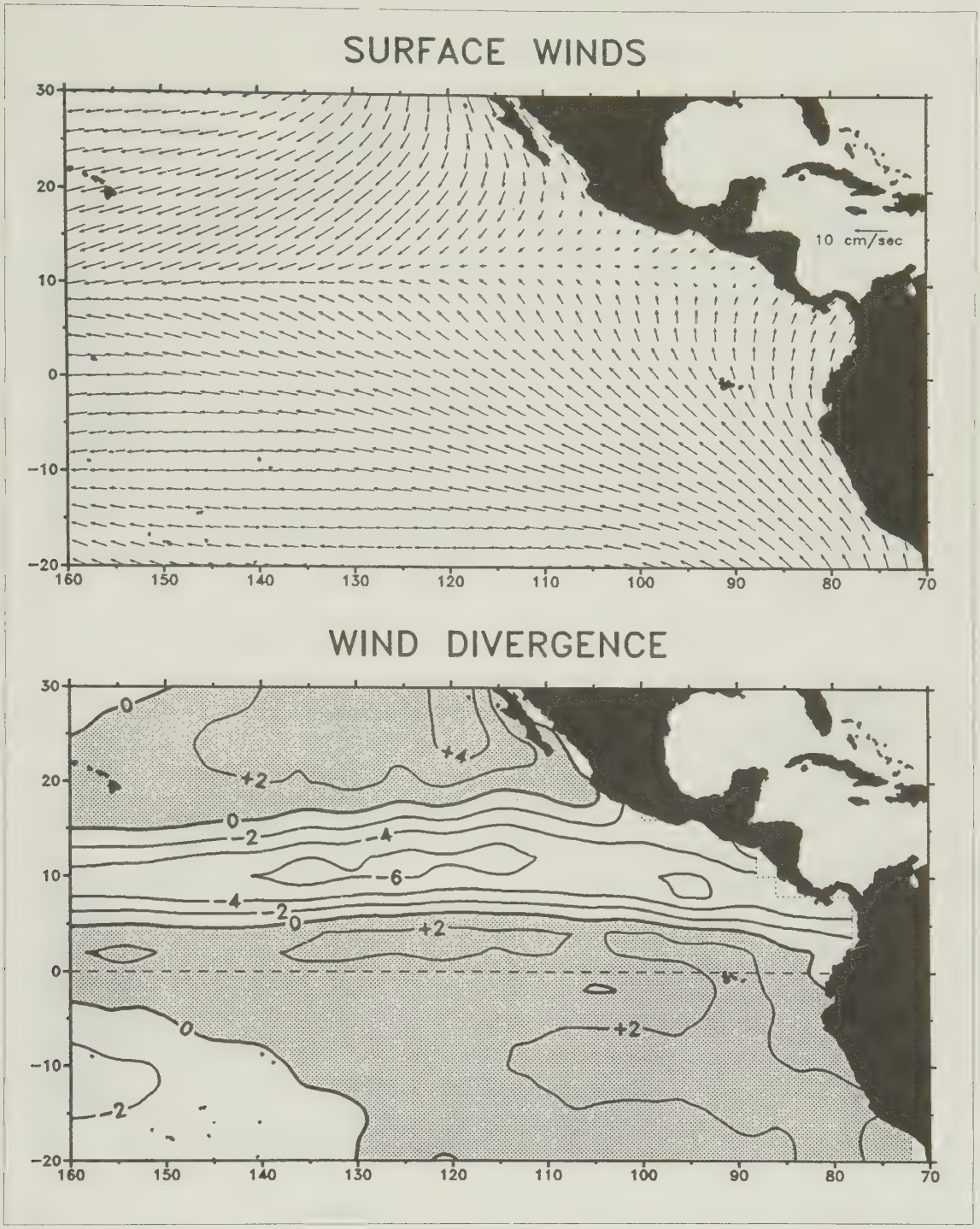

Figure A-10

Annual climatologies of surface wind velocity and wind divergence (10^{-6} sec^{-1}), from 1961–1989 Florida State University monthly gridded fields of pseudostress. The band of strong negative divergence along 10°N is the intertropical convergence zone (ITCZ).

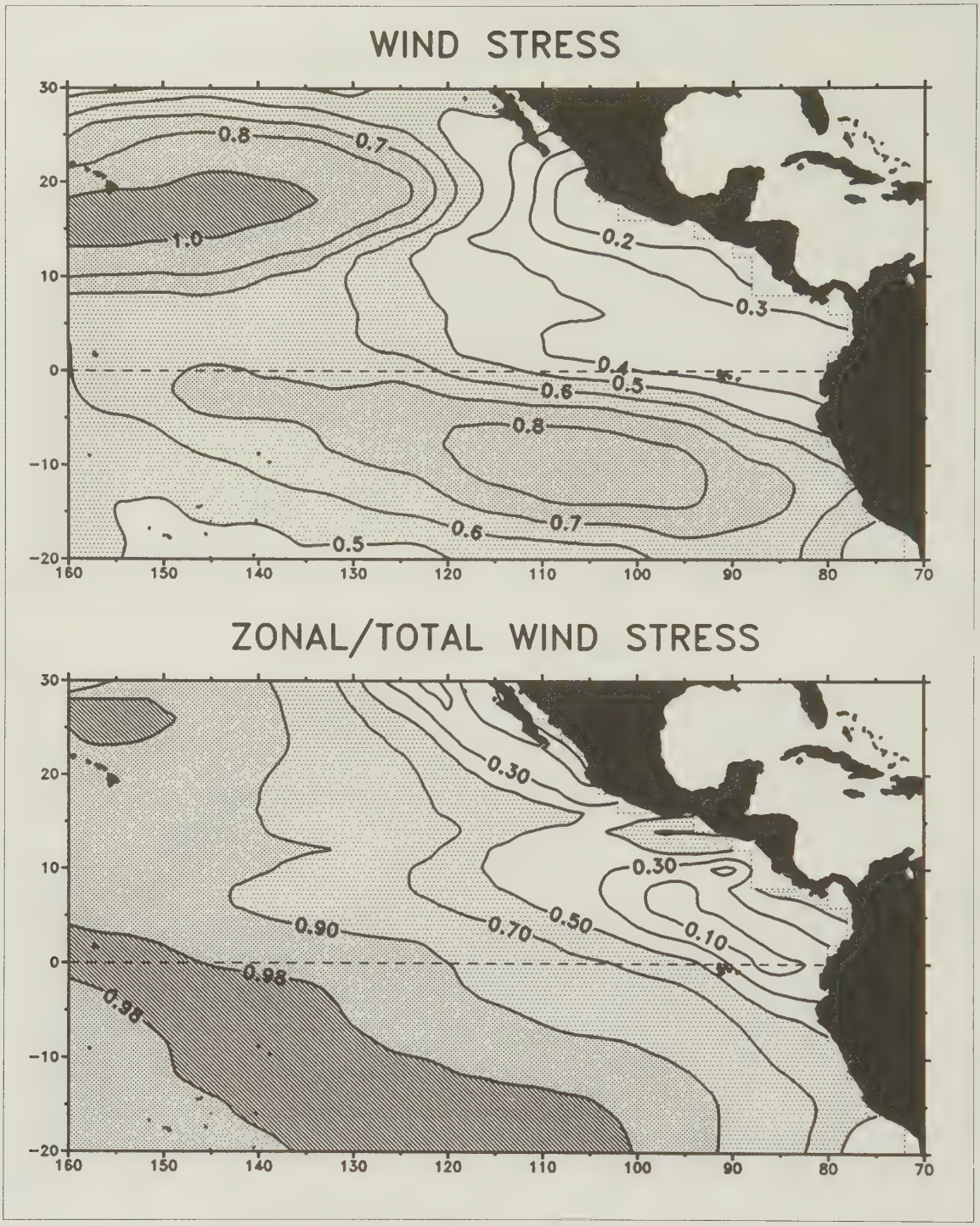

Figure A-11

Annual climatology of surface wind stress (dyne cm^{-2}) and ratio of zonal to total wind stress in annual climatologies, from 1961–1989 Florida State University monthly gridded fields of pseudostress.

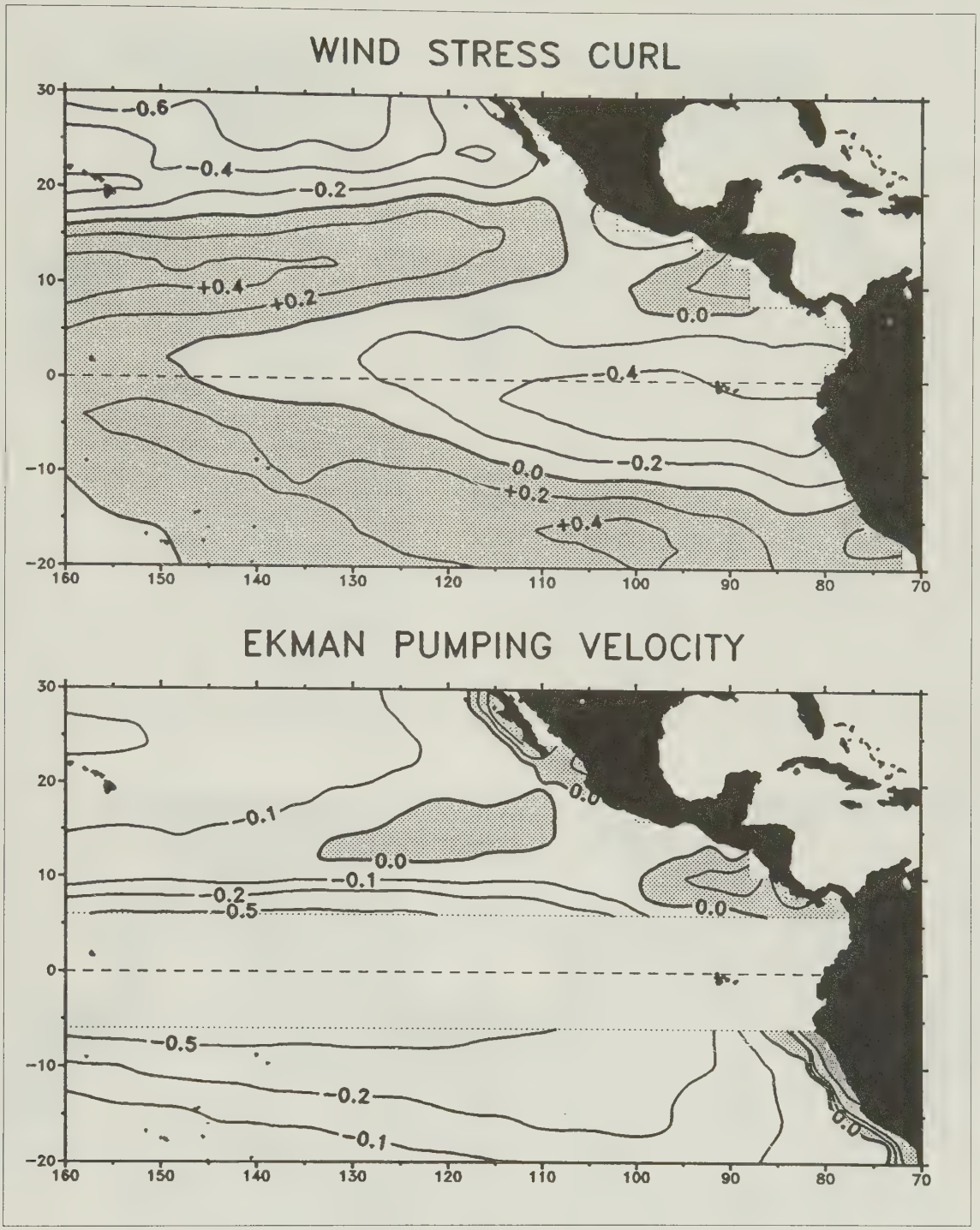

Figure A-12

Annual climatologies of surface wind stress curl (10^{-8} dyne cm^{-3}) and Ekman pumping velocity (10^{-3} cm s^{-1}), derived from 1961–1989 Florida State University monthly gridded fields of pseudostress. Ekman pumping velocity is undefined within 6 degrees of the equator.

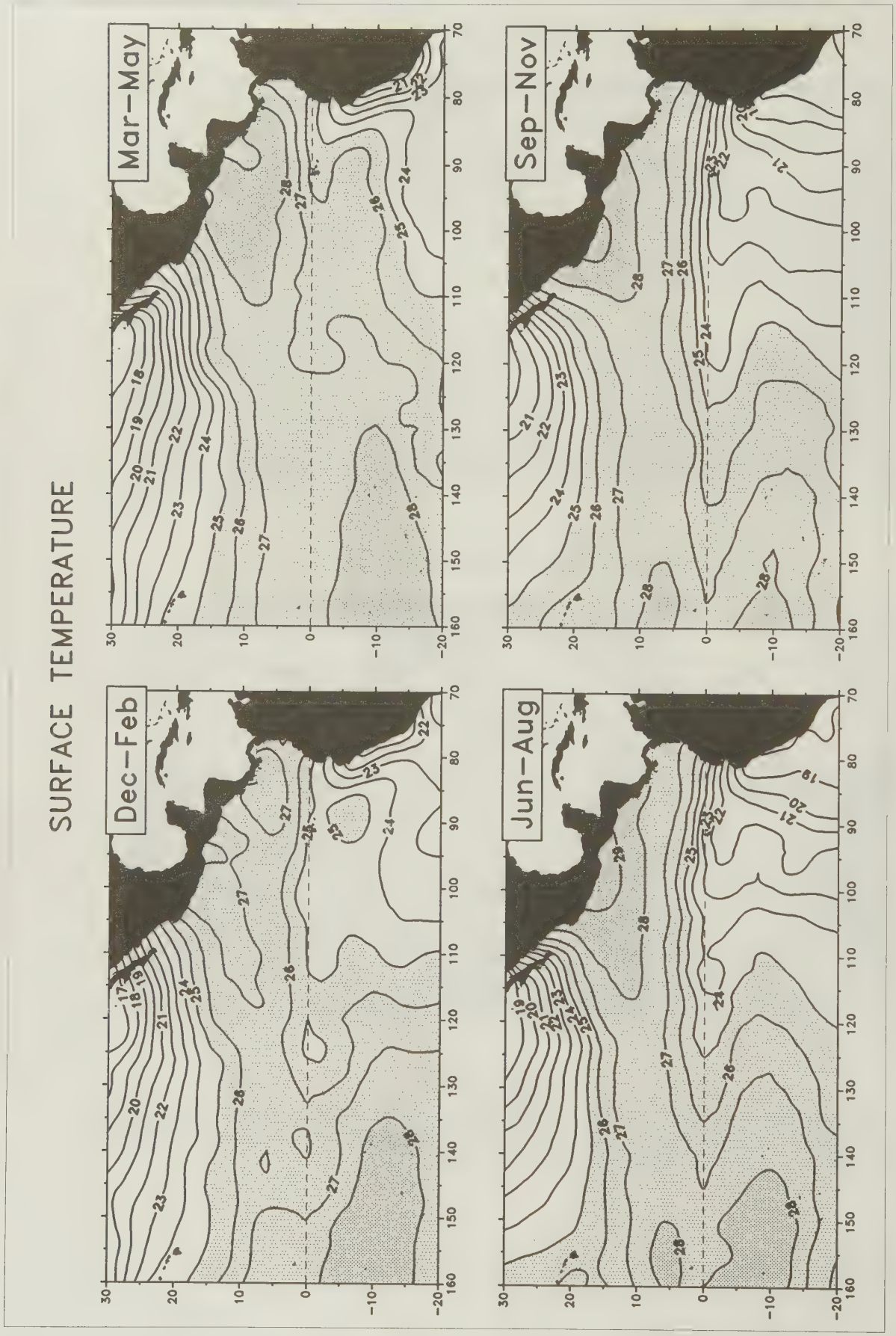

Figure A-13a
Surface temperature seasonal climatologies (°C), from 1960–1990 bathythermograph data.

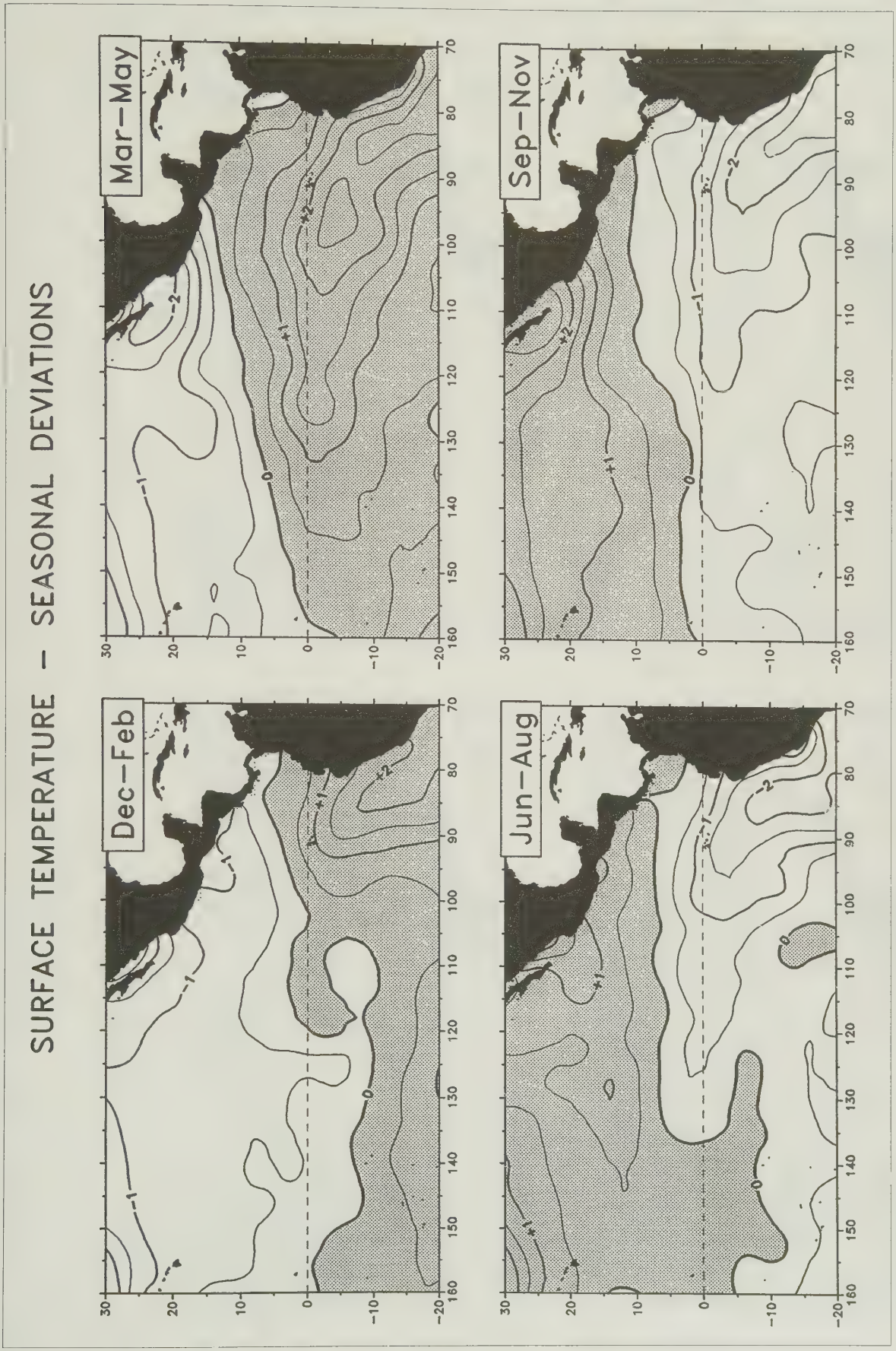

Figure A-13b
Surface temperature seasonal deviations from annual climatology (°C).

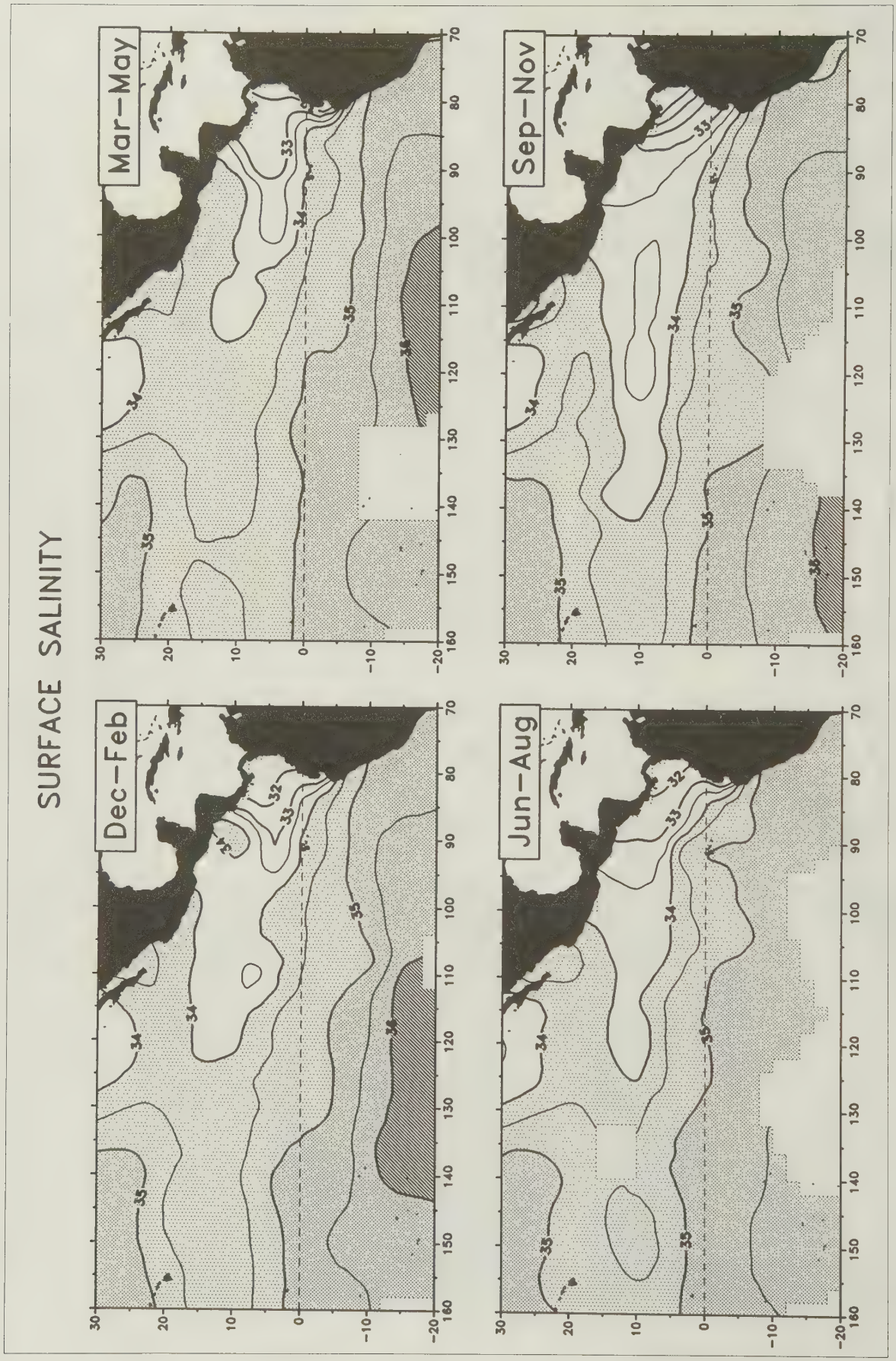

Figure A-14a
Surface salinity seasonal climatologies (psu), from 1960–1988 hydrographic data.

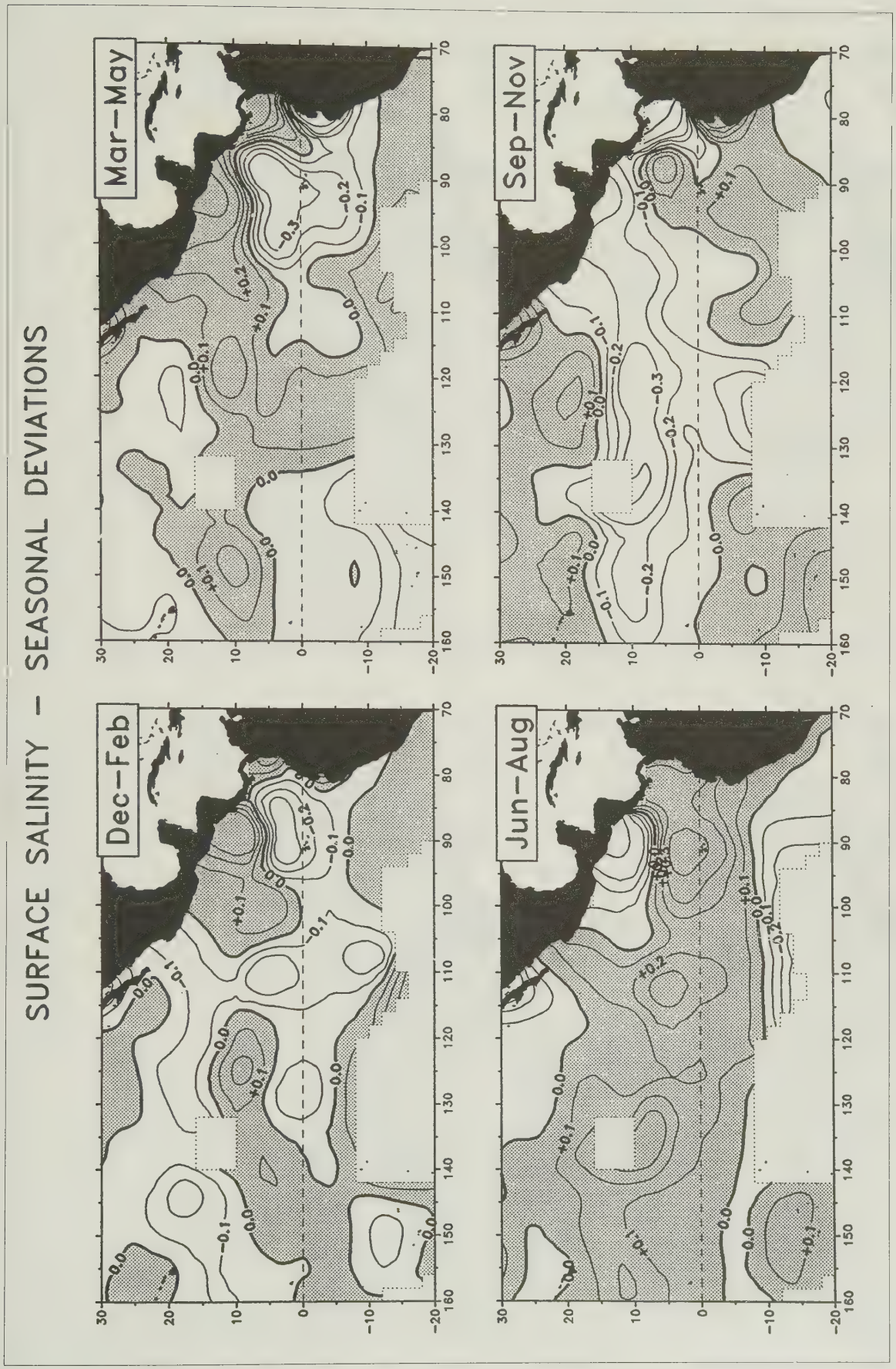

Figure A-14b
Surface salinity seasonal deviations from annual climatology (psu).

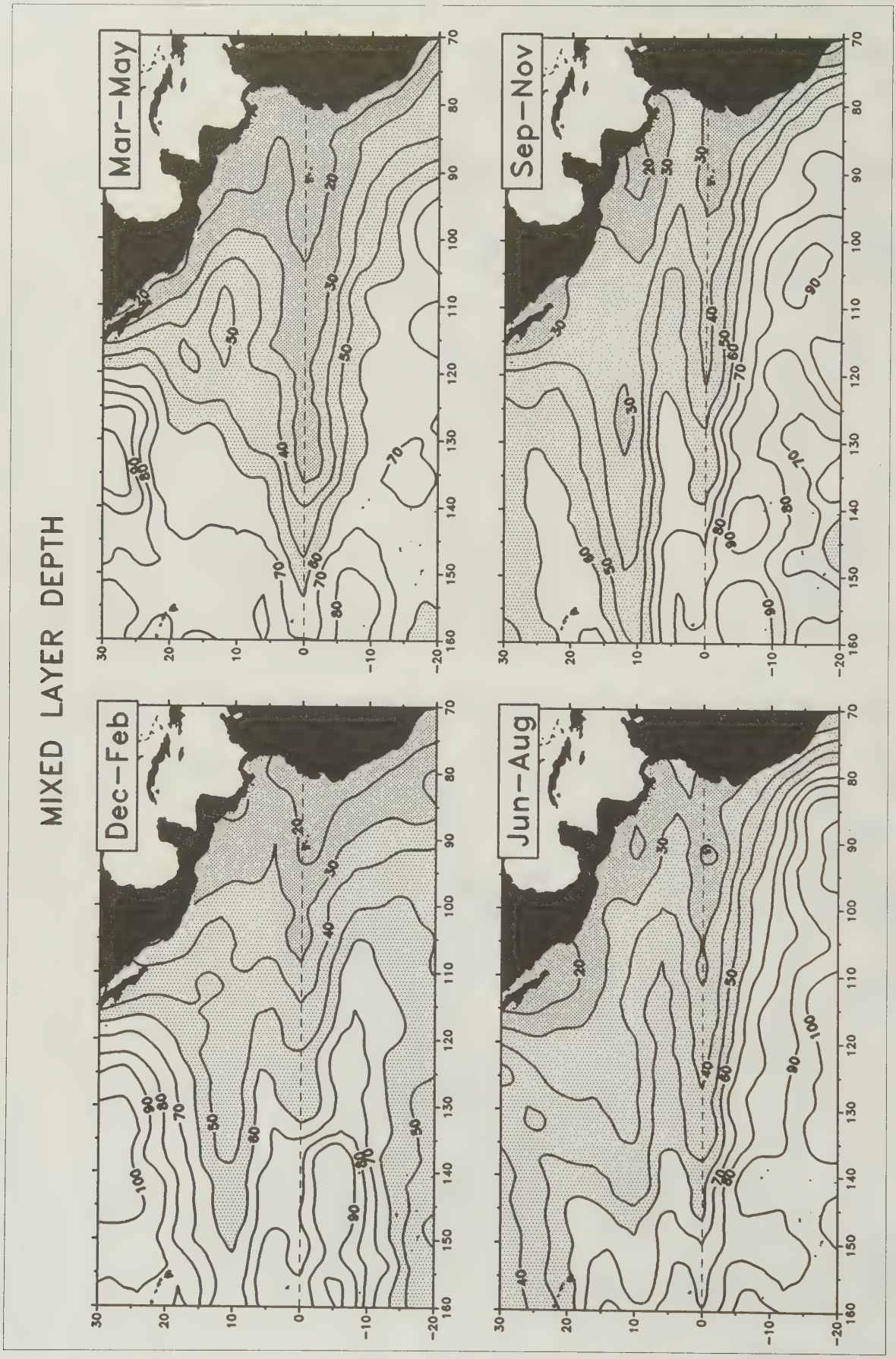

Figure A-15a
Mixed layer depth seasonal climatologies (m), from 1960–1990 bathythermograph data.

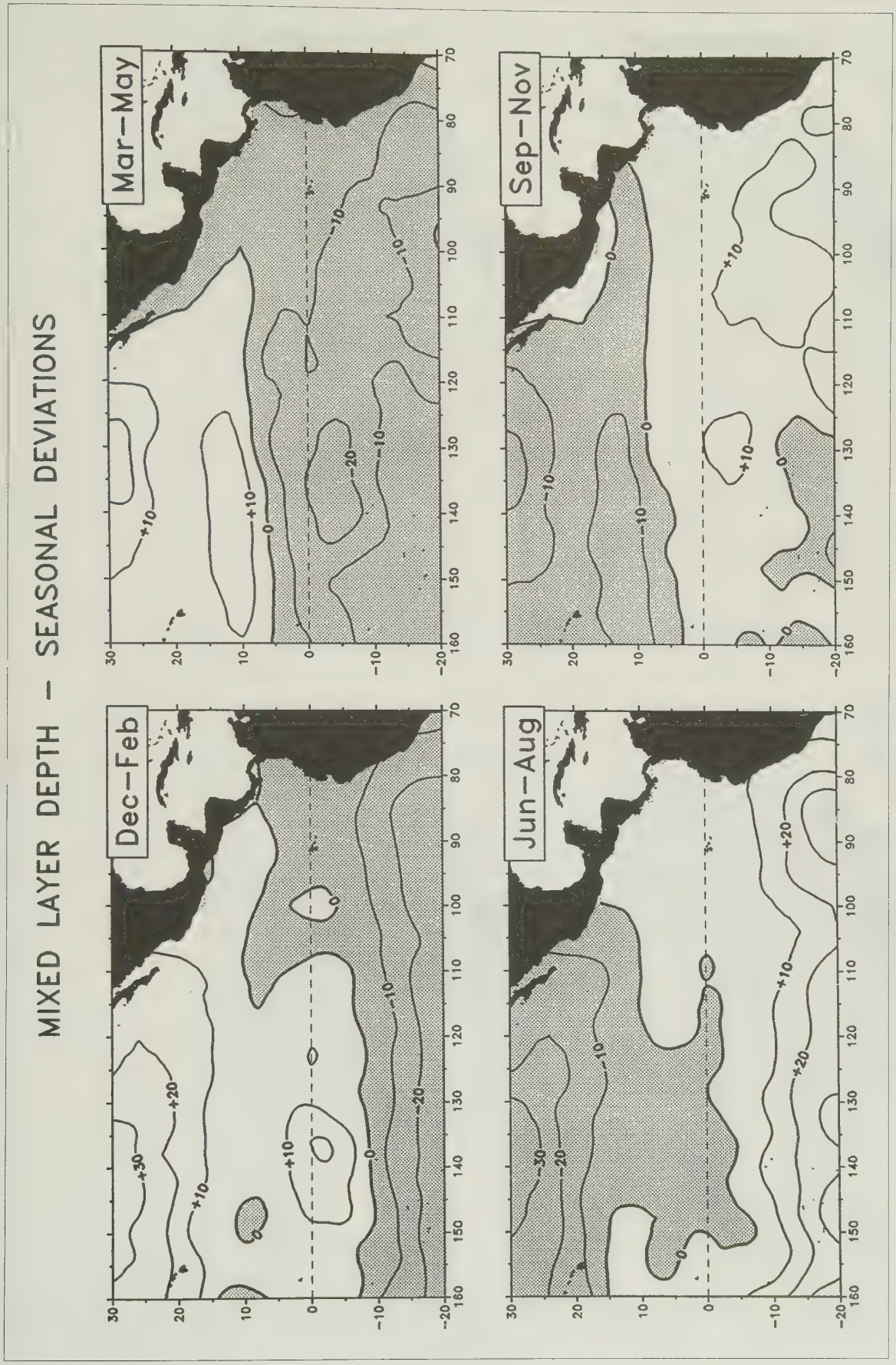

Figure A-15b
Mixed layer depth seasonal deviations from annual climatology (m).

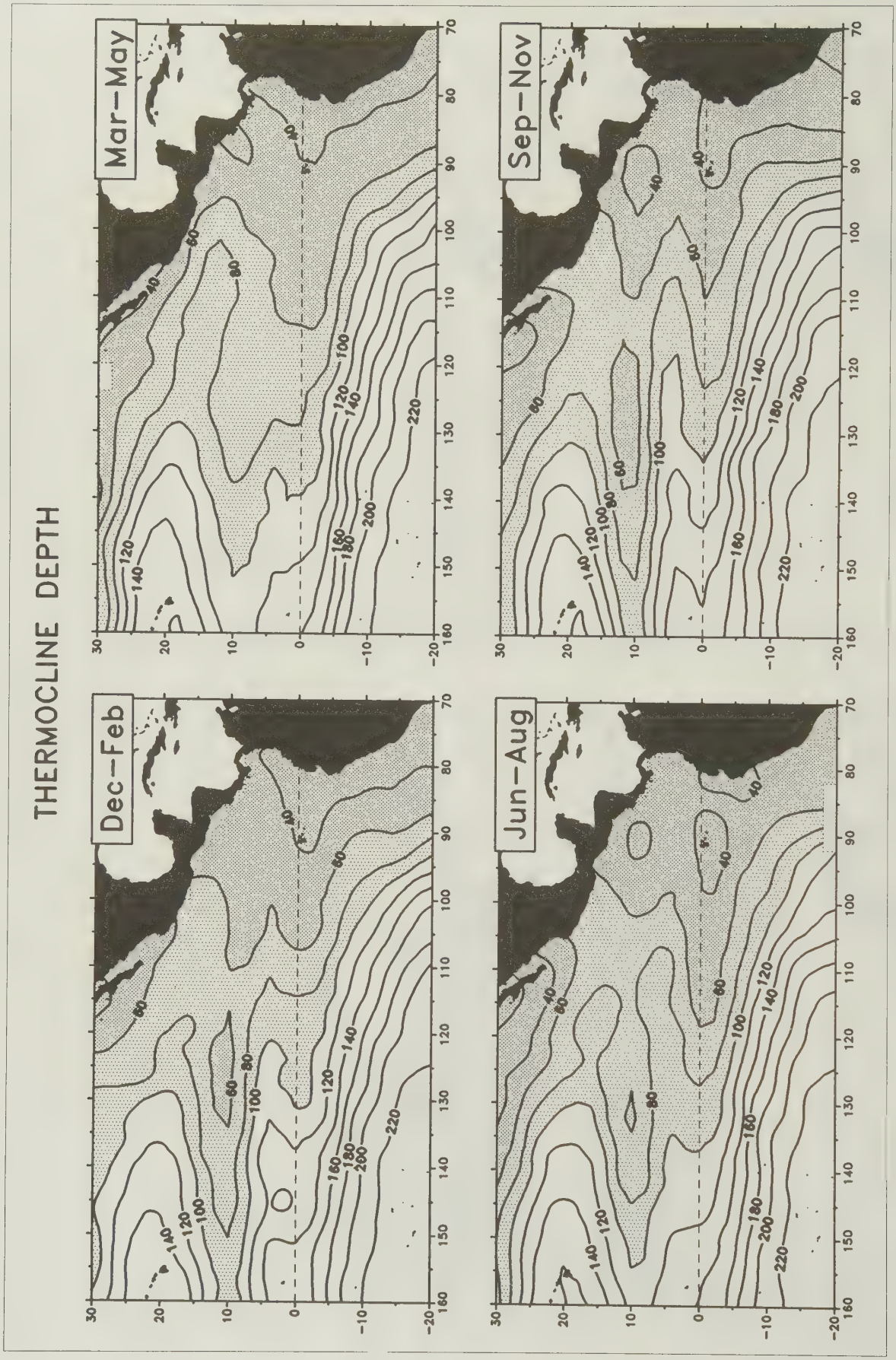

Figure A-16a
Thermocline (20°C isotherm) depth seasonal climatologies (m), from 1960–1990 bathythermograph data.

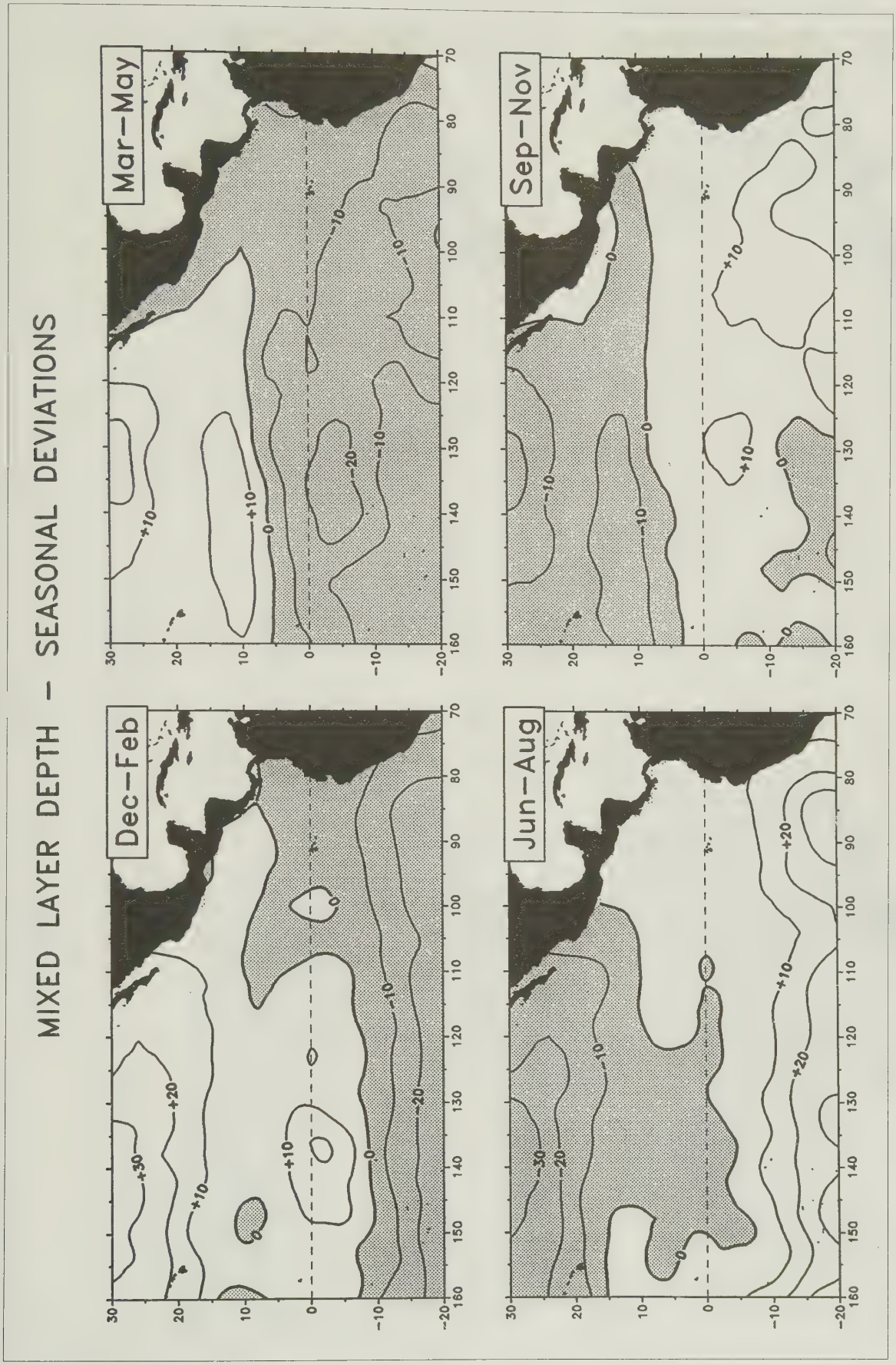

Figure A-15b
Mixed layer depth seasonal deviations from annual climatology (m).

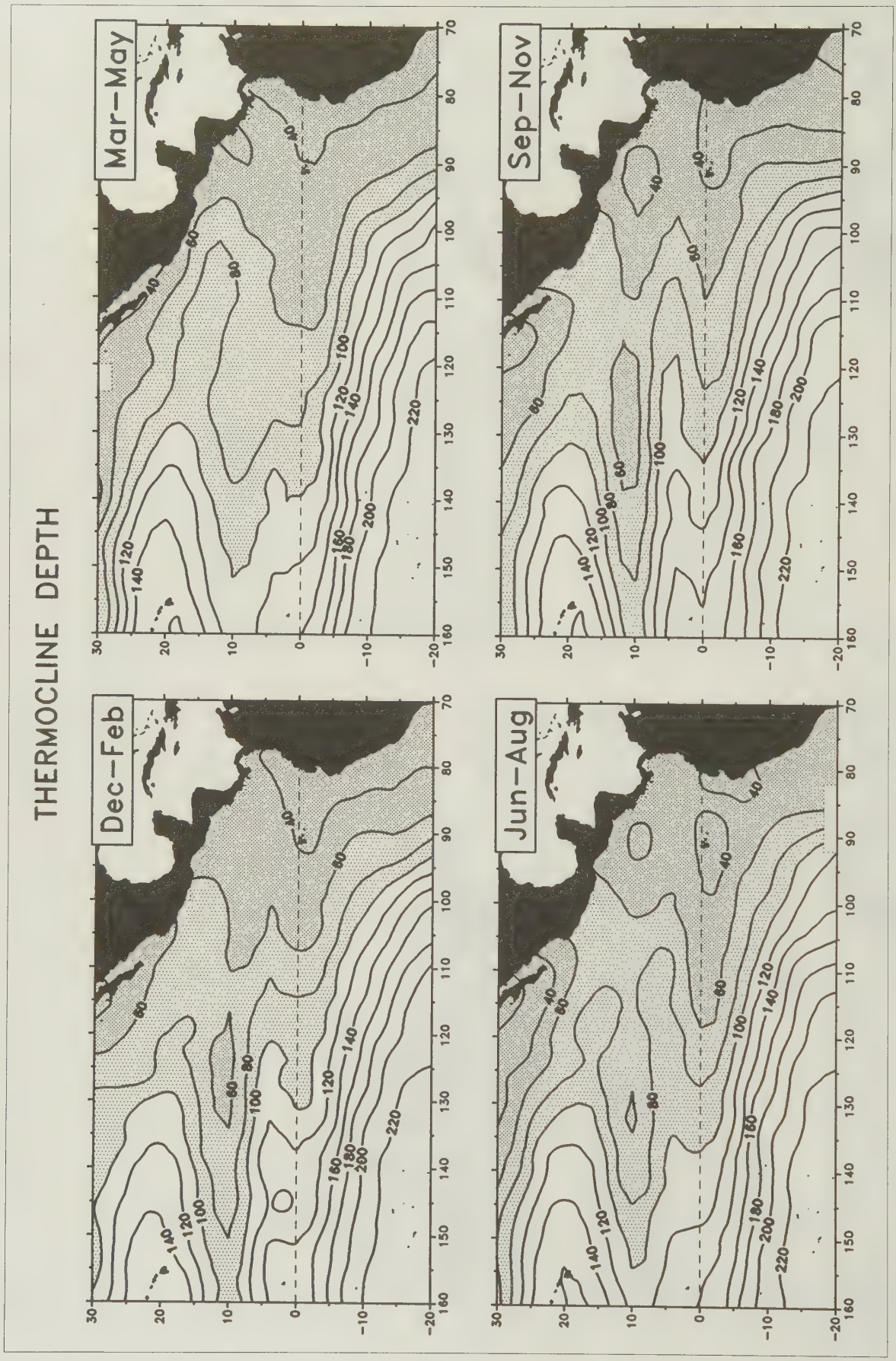

Figure A-16a
Thermocline (20°C isotherm) depth seasonal climatologies (m), from 1960–1990 bathythermograph data.

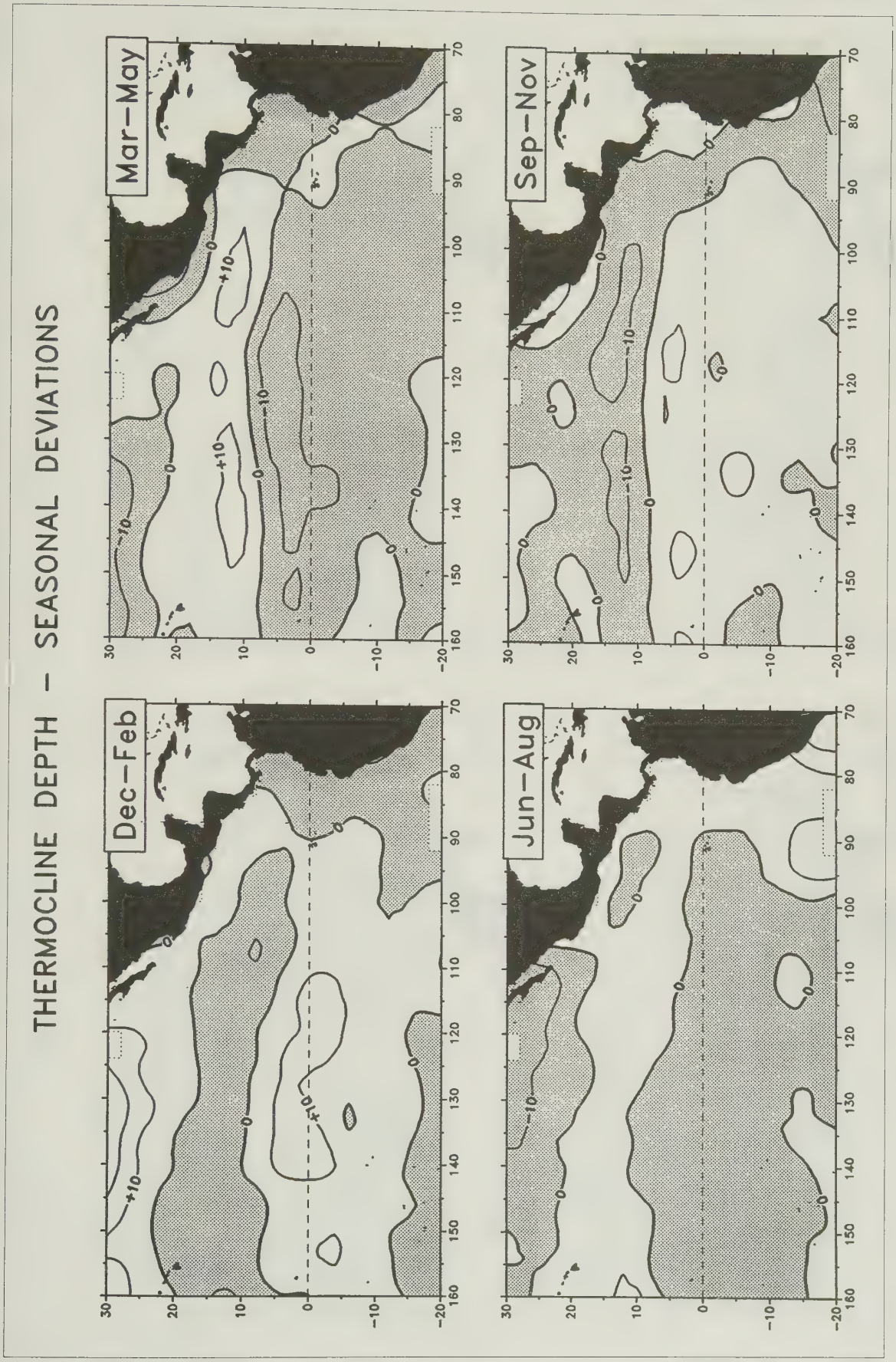

Figure A-16b
Thermocline (20°C isotherm) depth seasonal deviations from annual climatology (m).

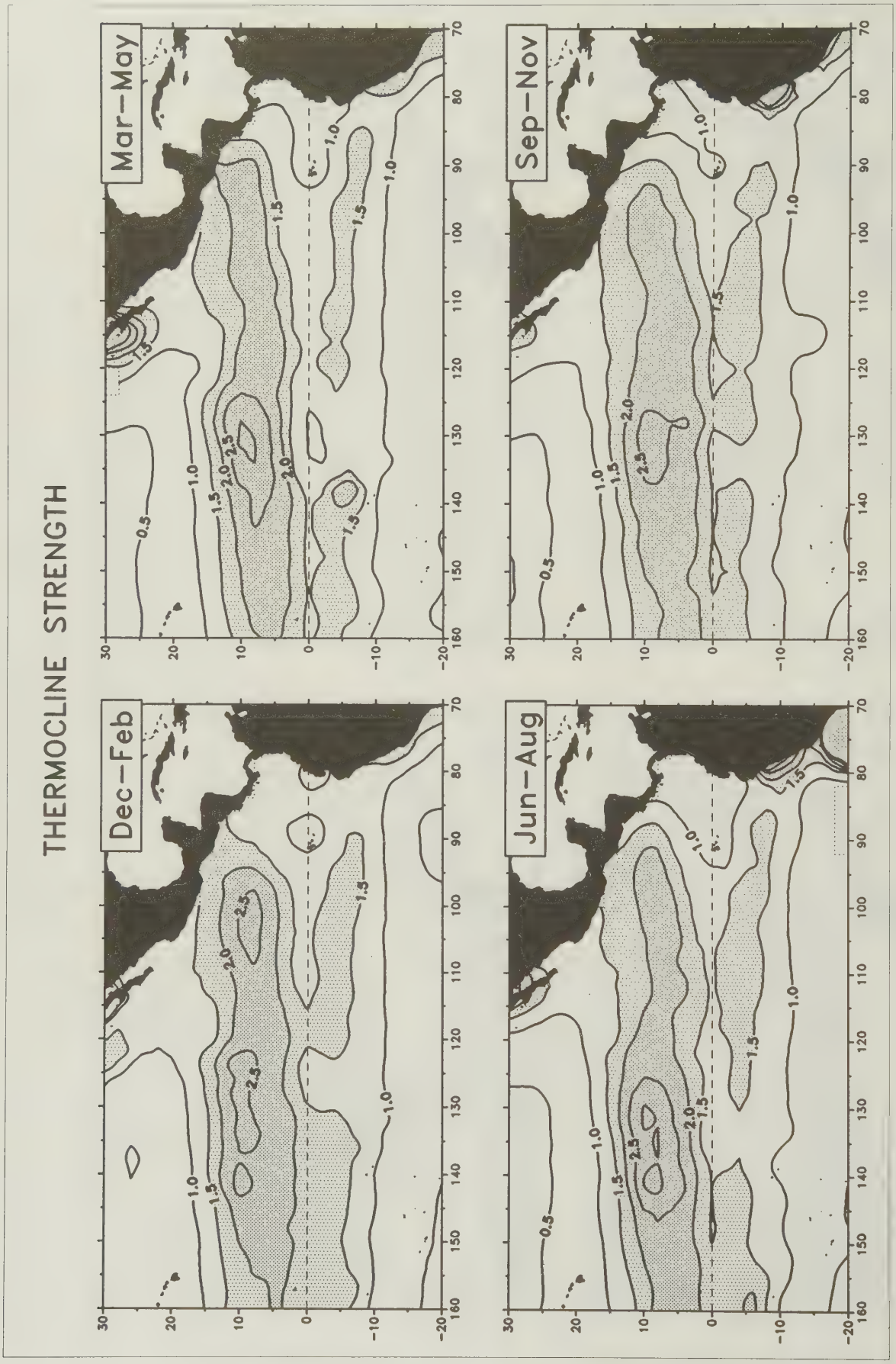

Figure A-17a

Thermocline strength seasonal climatologies (°C $10m^{-1}$ between 20 and 15°C isotherms), derived from 1960–1990 bathythermograph data.

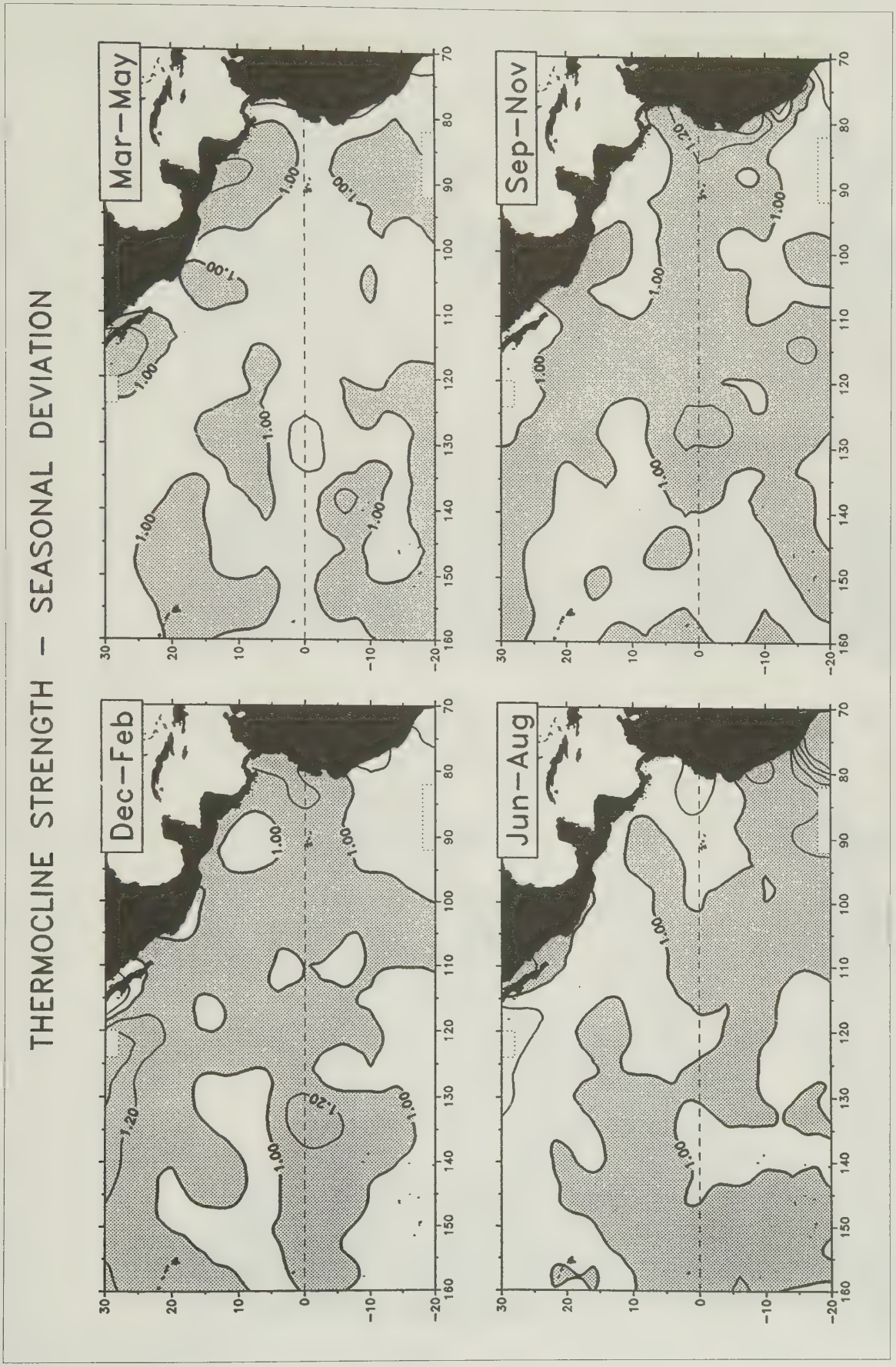

Figure A-17b
Thermocline strength ratio of seasonal to annual climatologies.

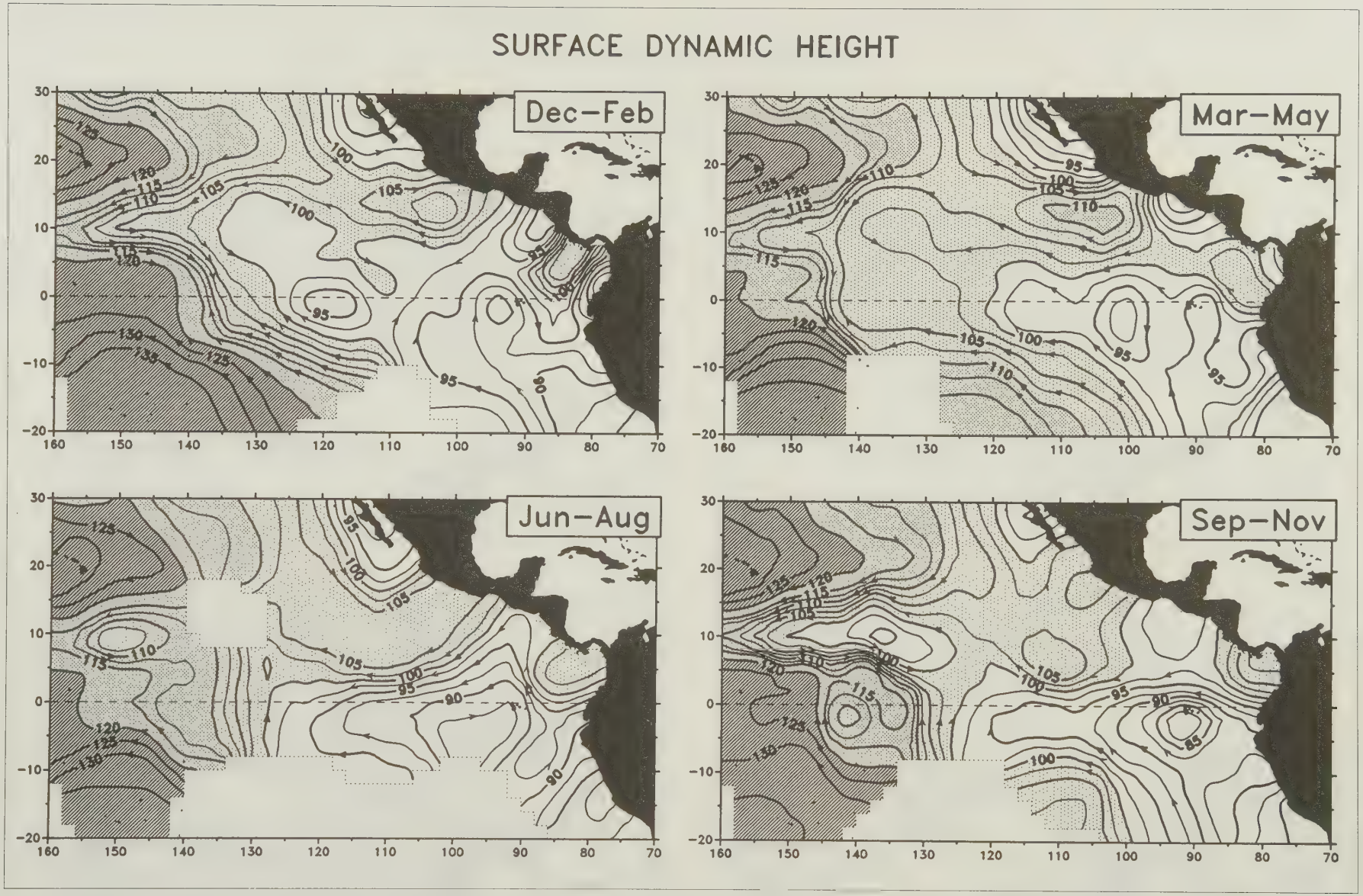

Figure A-18a
Surface dynamic height (relative to 500db) seasonal climatologies (dyn cm), from 1960–1988 hydrographic data.

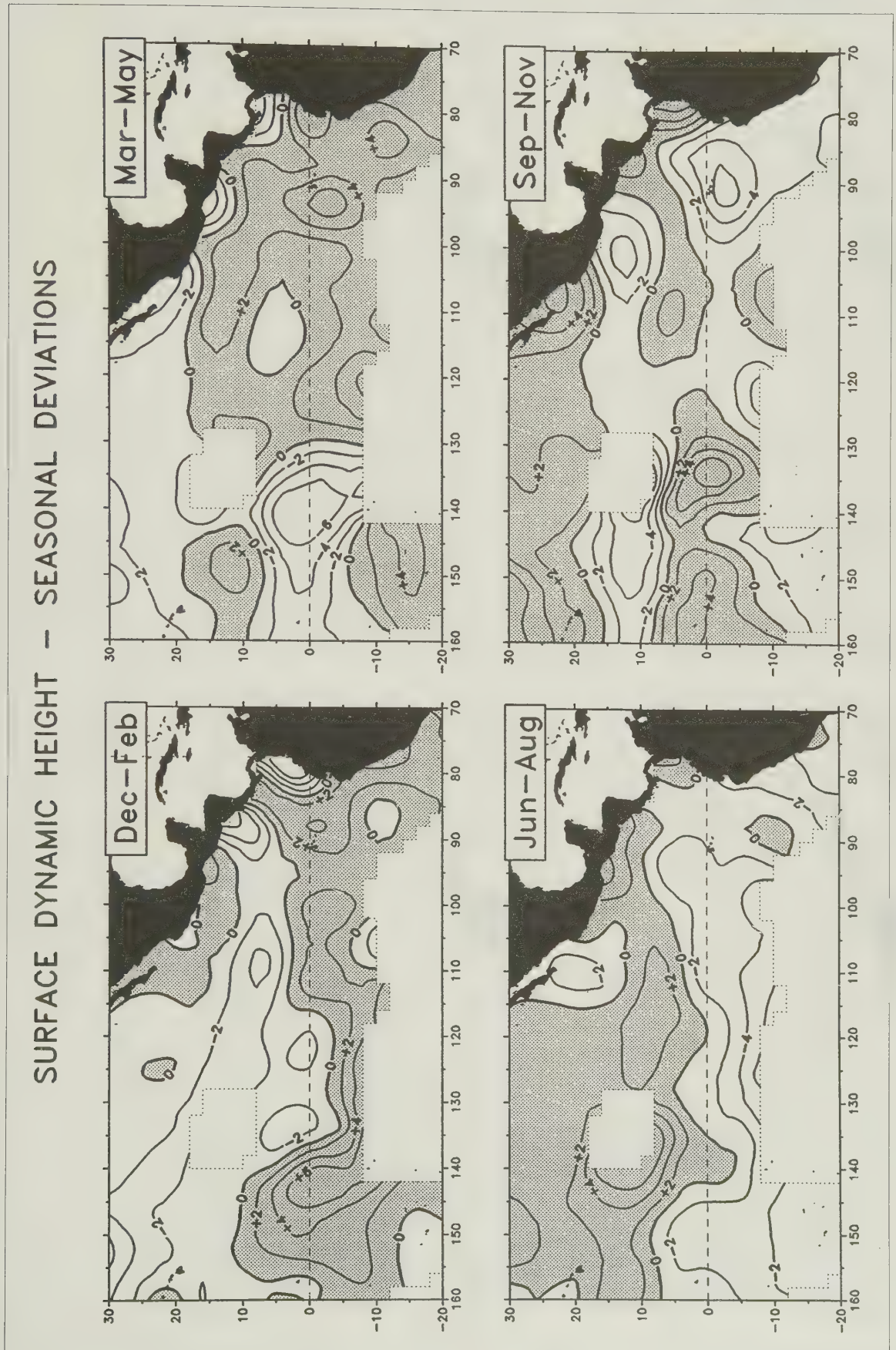

Figure A-18b
Surface dynamic height (relative to 500db) seasonal deviations from annual climatology (dyn cm).

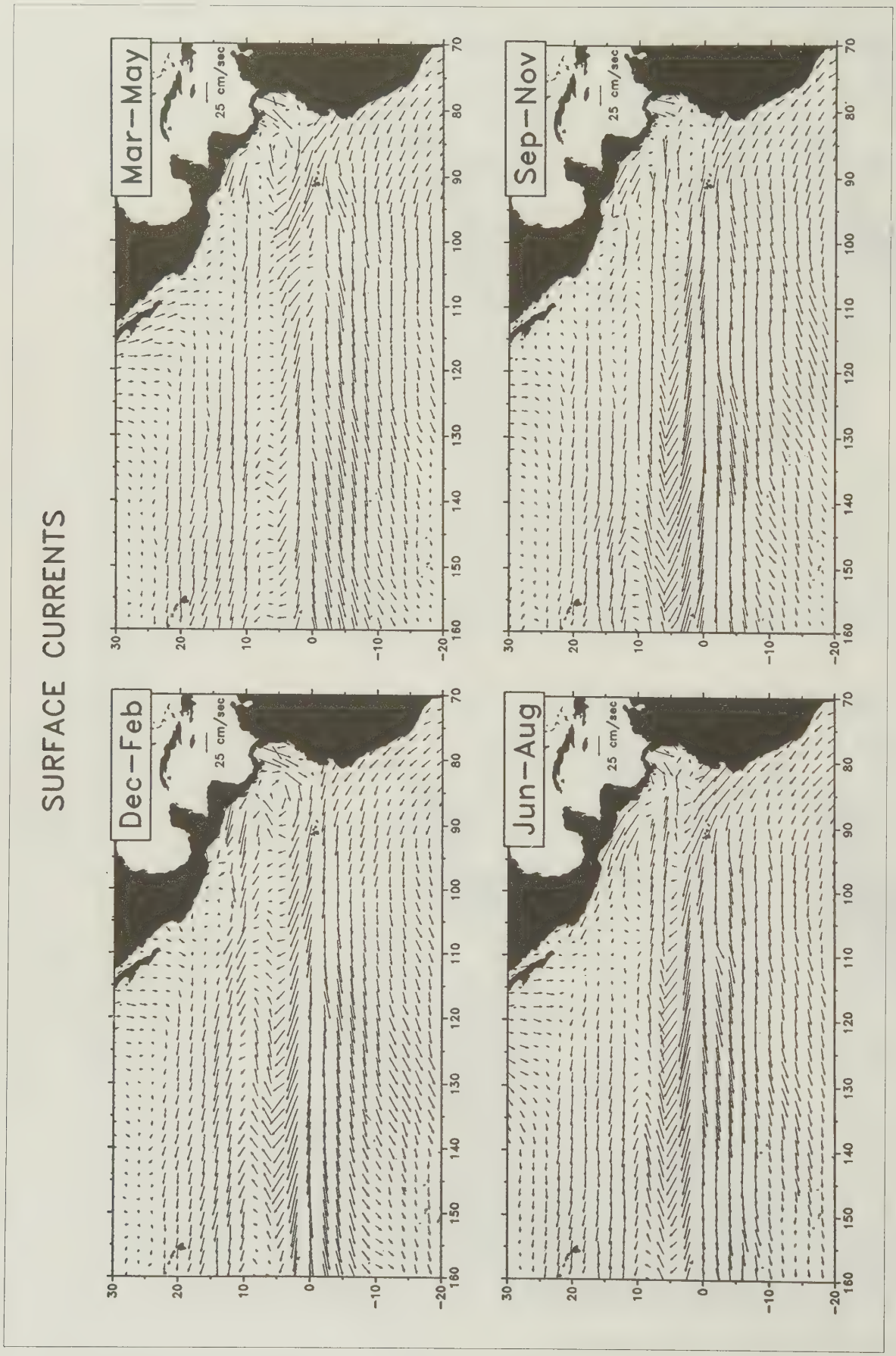

Figure A-19a
Surface current velocity (from ship drift) seasonal climatologies, from 1900–1969 ship drift reports.

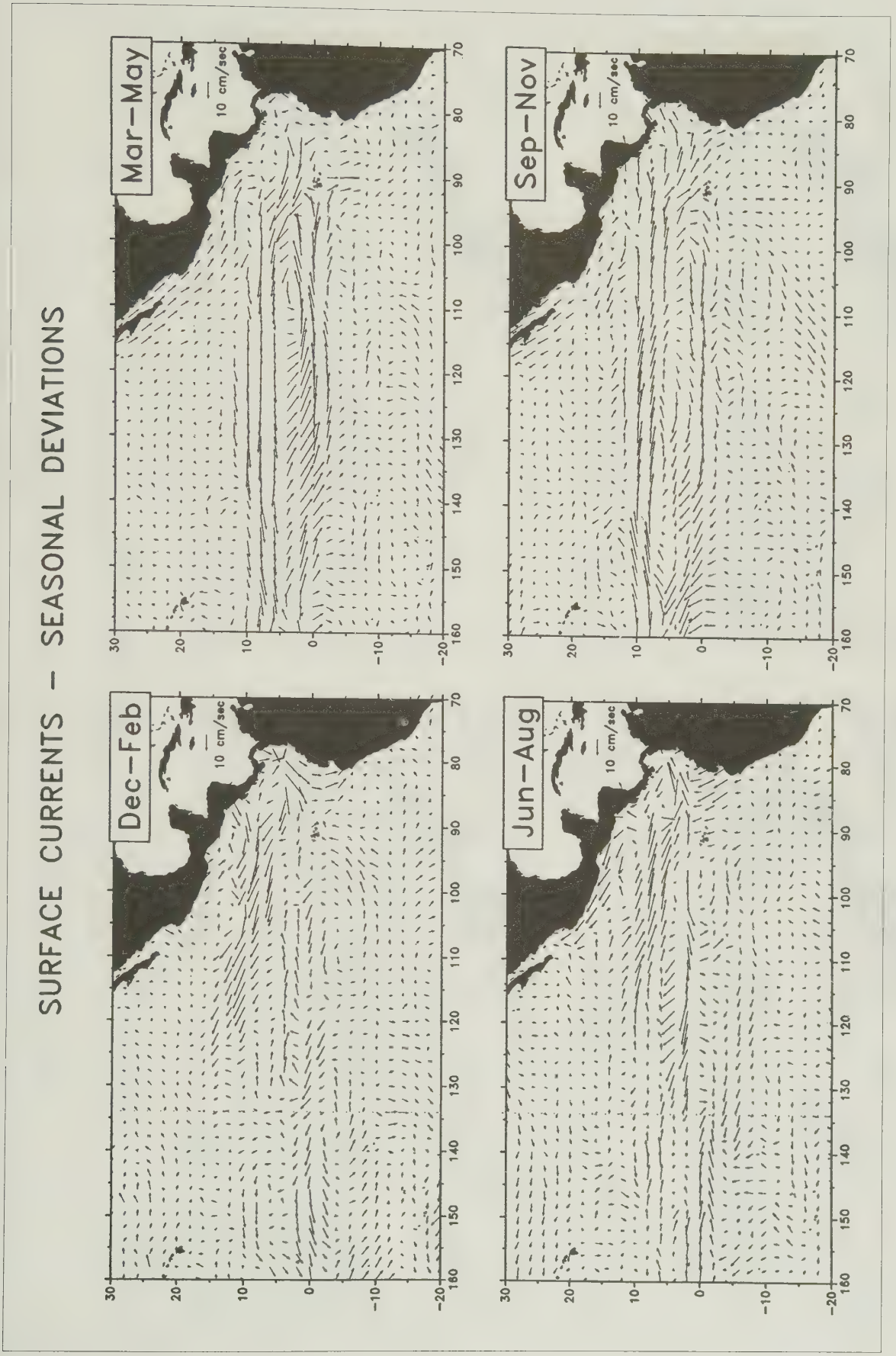

Figure A-19b
Surface current velocity seasonal deviations from annual climatology.

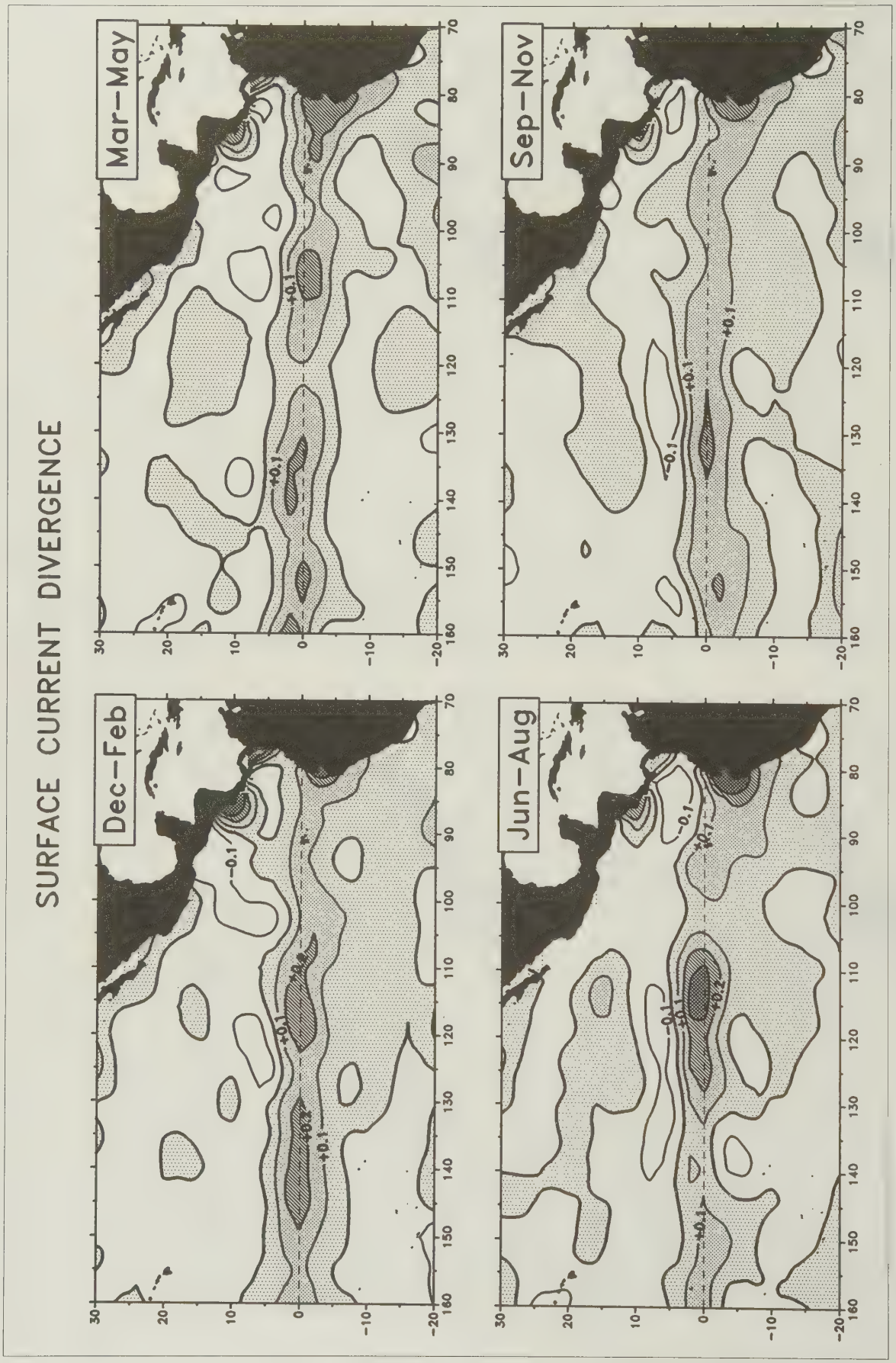

Figure A-20a
Surface current divergence seasonal climatologies (10^{-6} s^{-1}), derived from 1900–1969 ship drift reports.

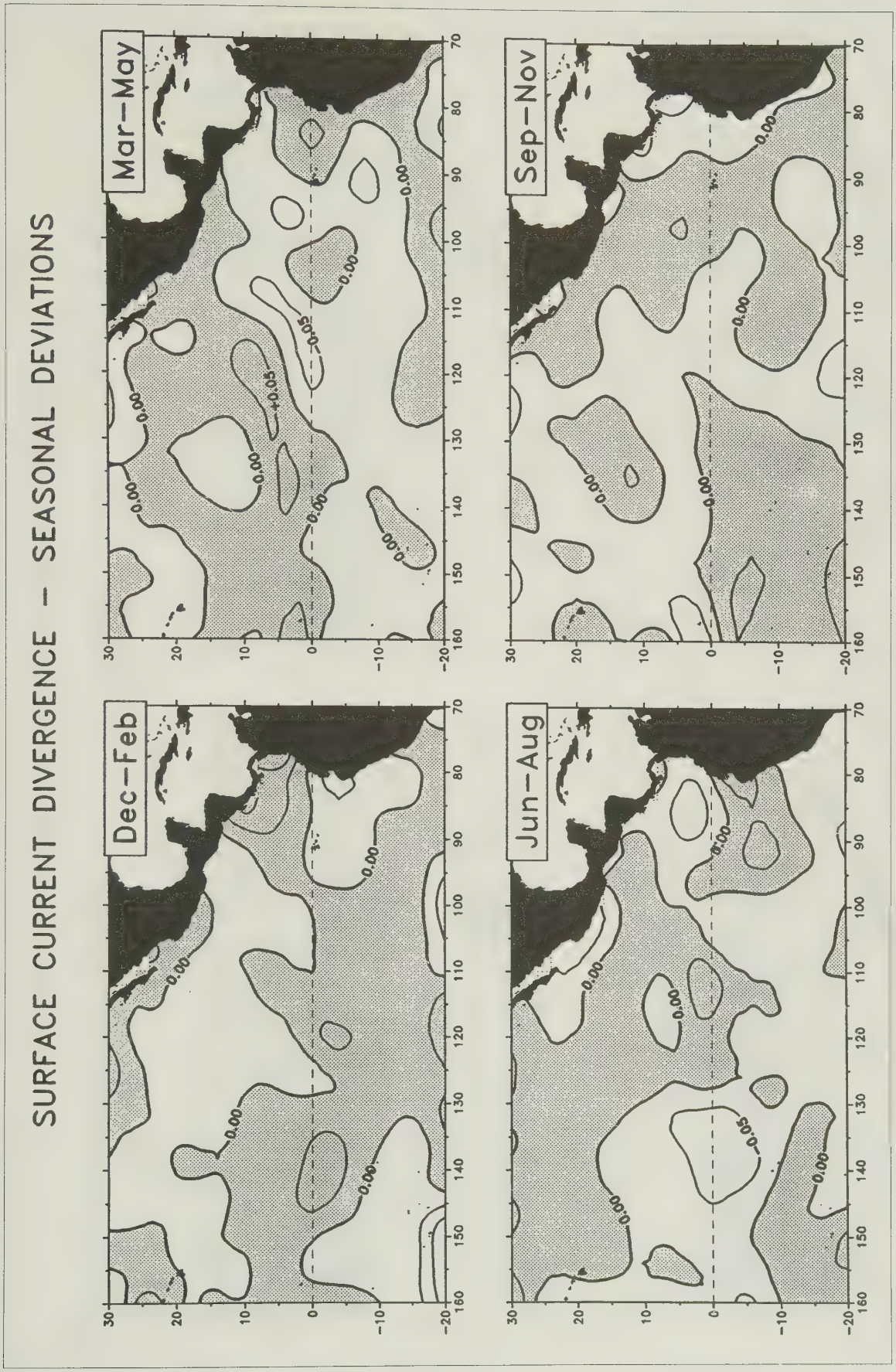

Figure A-20b
Surface current divergence seasonal deviations from annual climatology (10^{-6} s^{-1}).

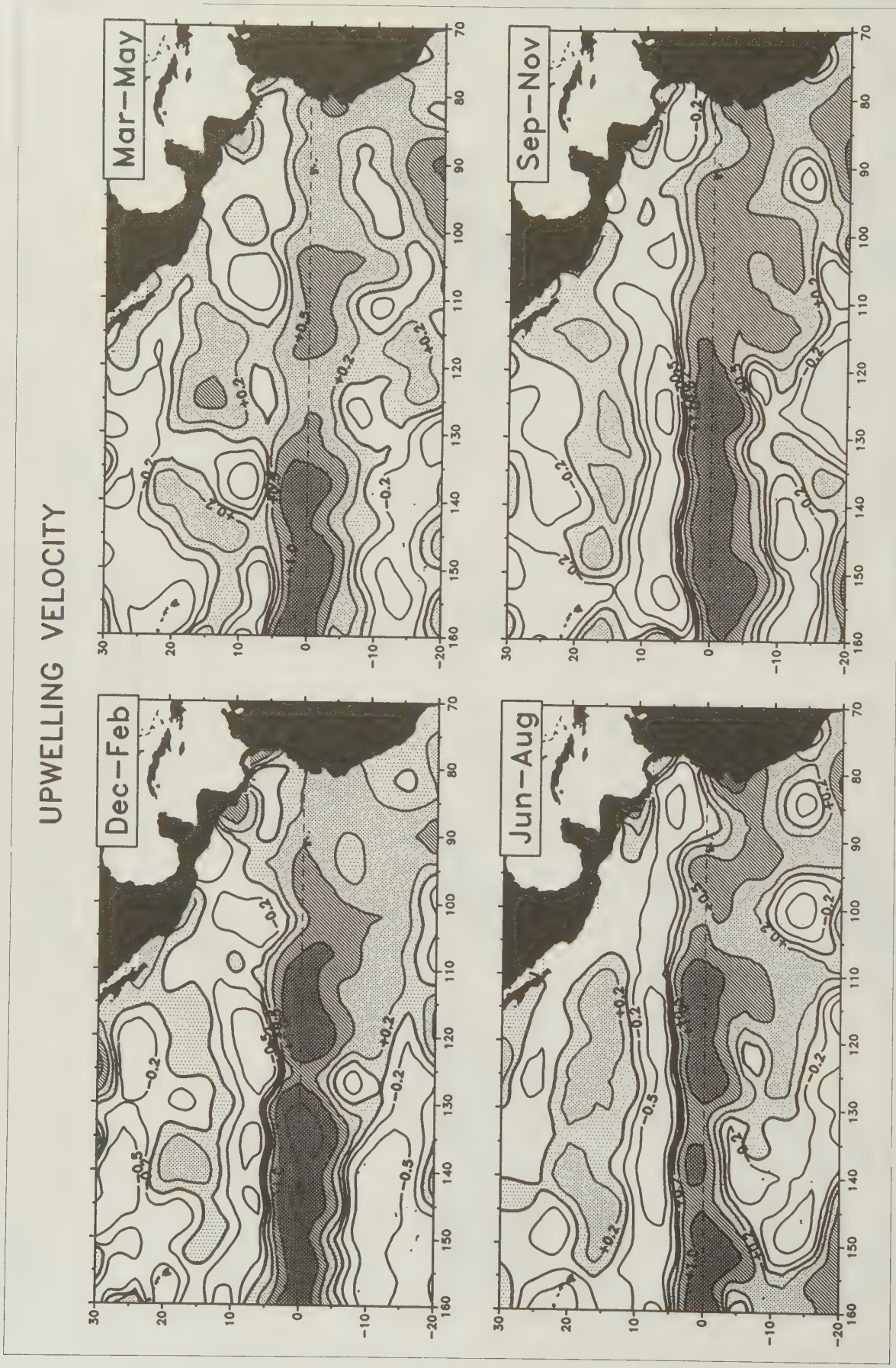

Figure A-21a
Upwelling velocity seasonal climatologies (10^{-3} cm s^{-1}), calculated from divergence of horizontal transports in the mixed layer.

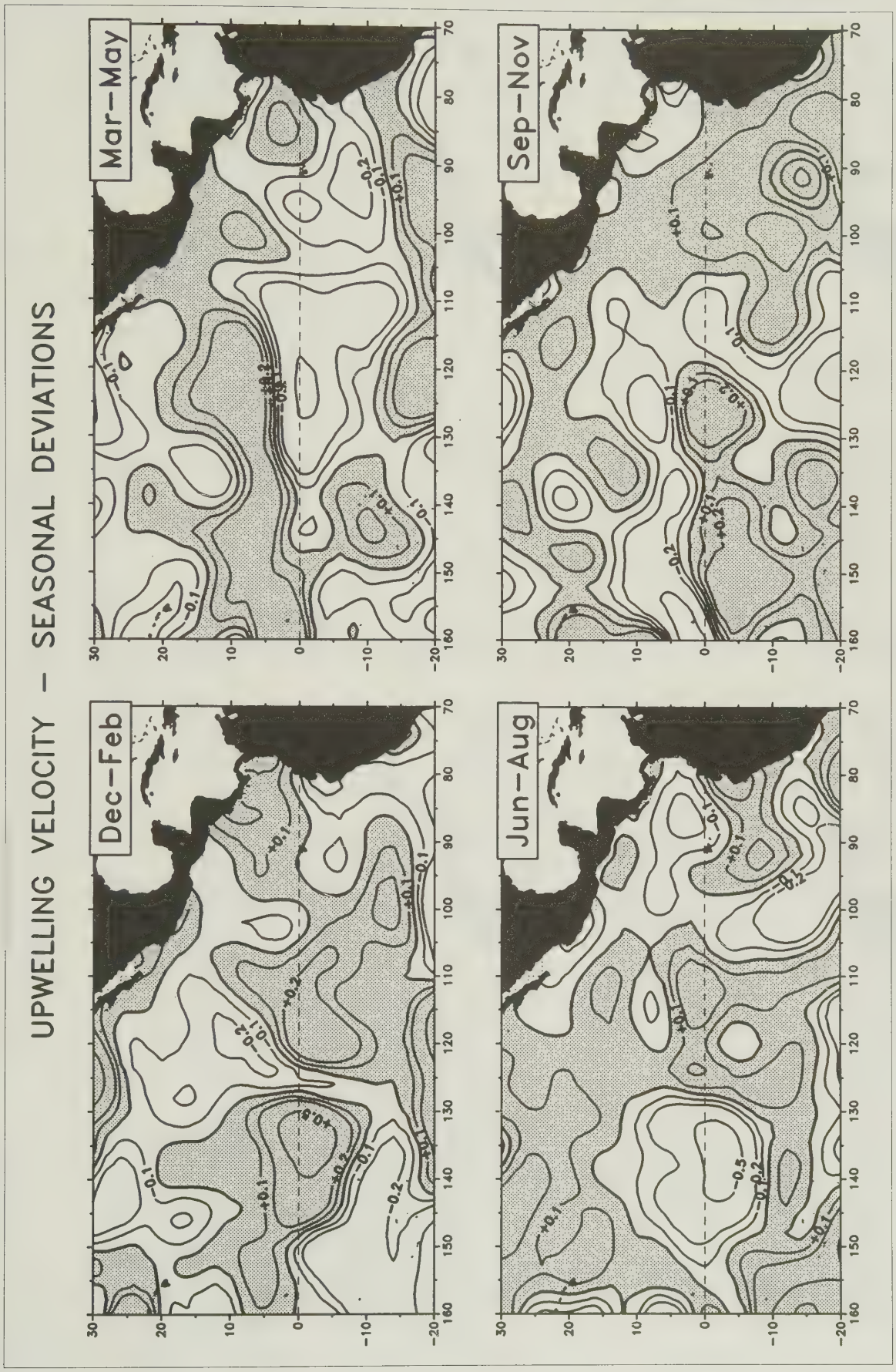

Figure A-21b
Upwelling velocity seasonal deviations from annual climatology (10^{-3} cm s^{-1}).

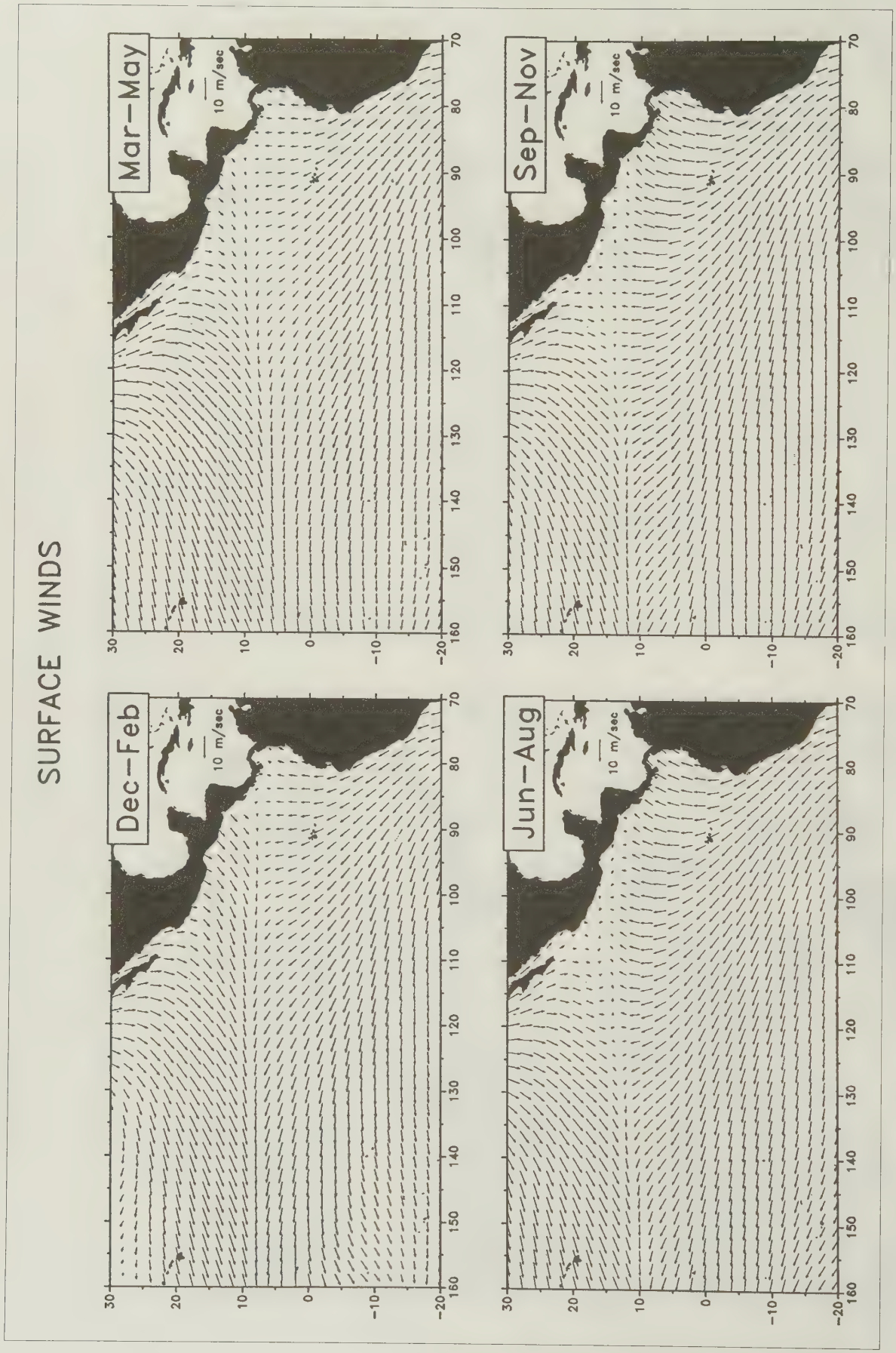

Figure A-22a
Surface wind velocity seasonal climatologies, from 1961–1989 Florida State University monthly gridded fields of pseudostress.

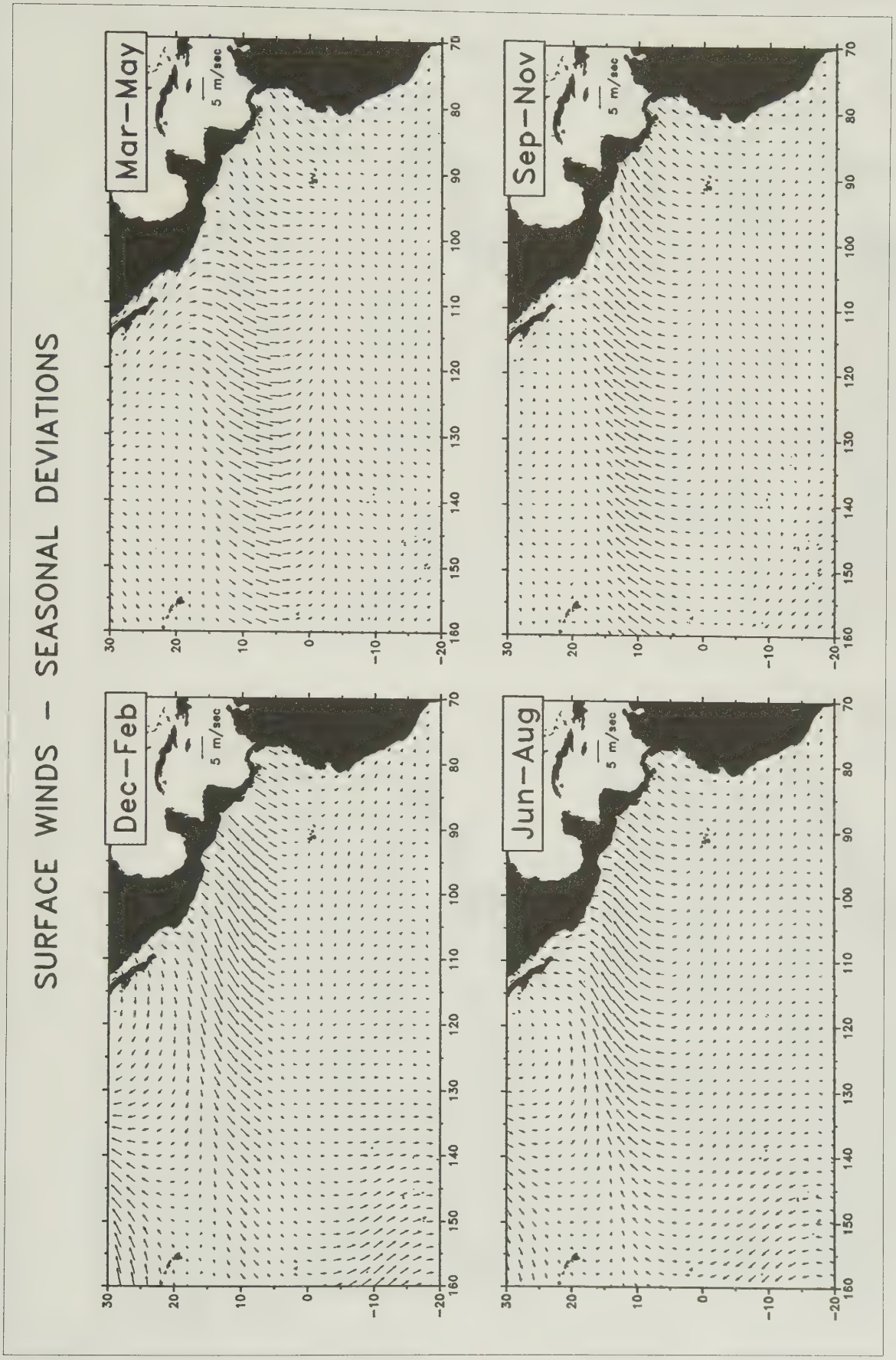

Figure A-22b
Surface wind velocity seasonal deviations from annual climatology.

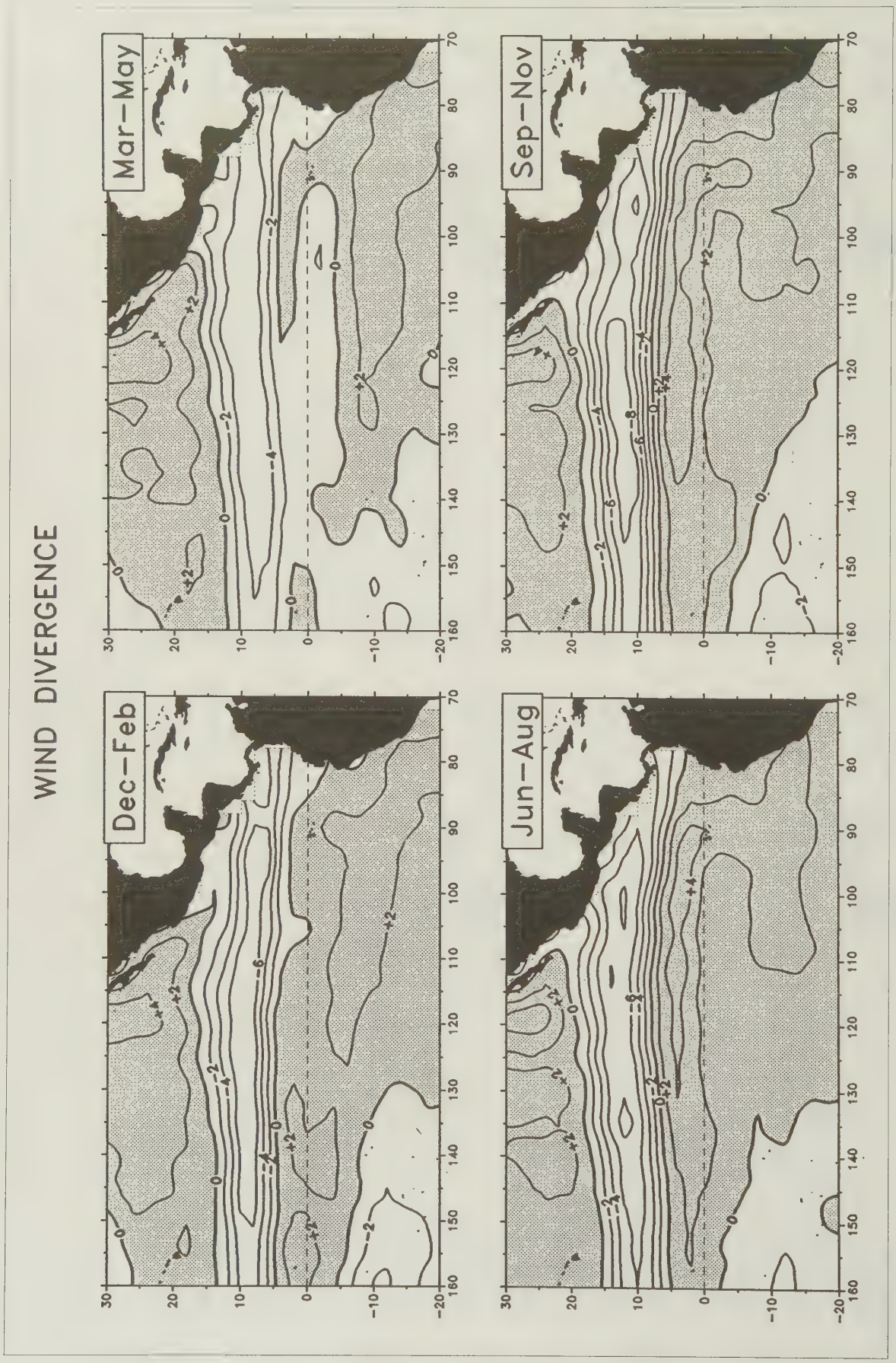

Figure A-23a

Surface wind divergence seasonal climatologies (10^{-6} s^{-1}), derived from 1961–1989 Florida State University monthly gridded fields of pseudostress.

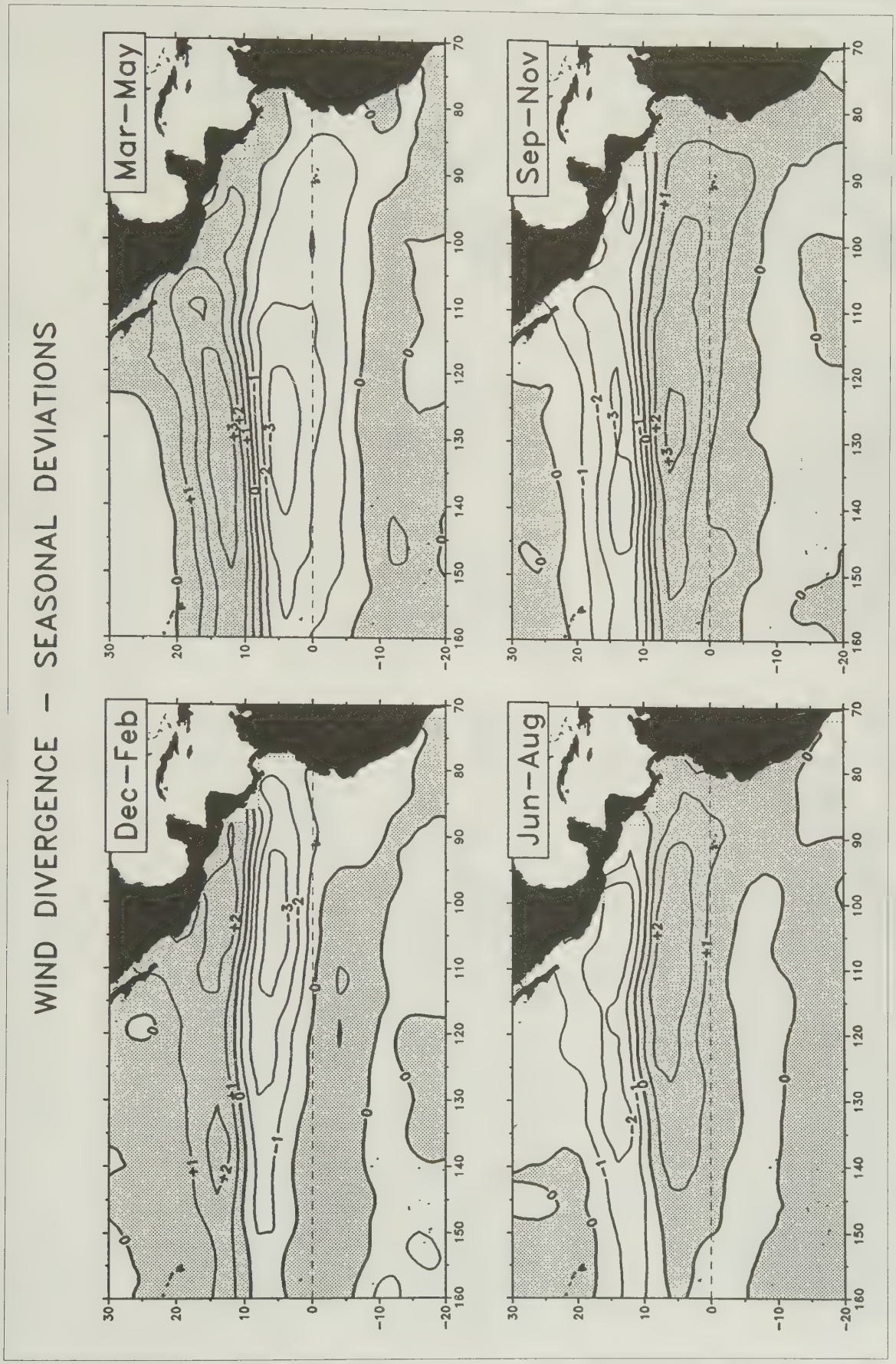

Figure A-23b
Surface wind divergence seasonal deviations from annual climatology (10^{-6} s^{-1}).

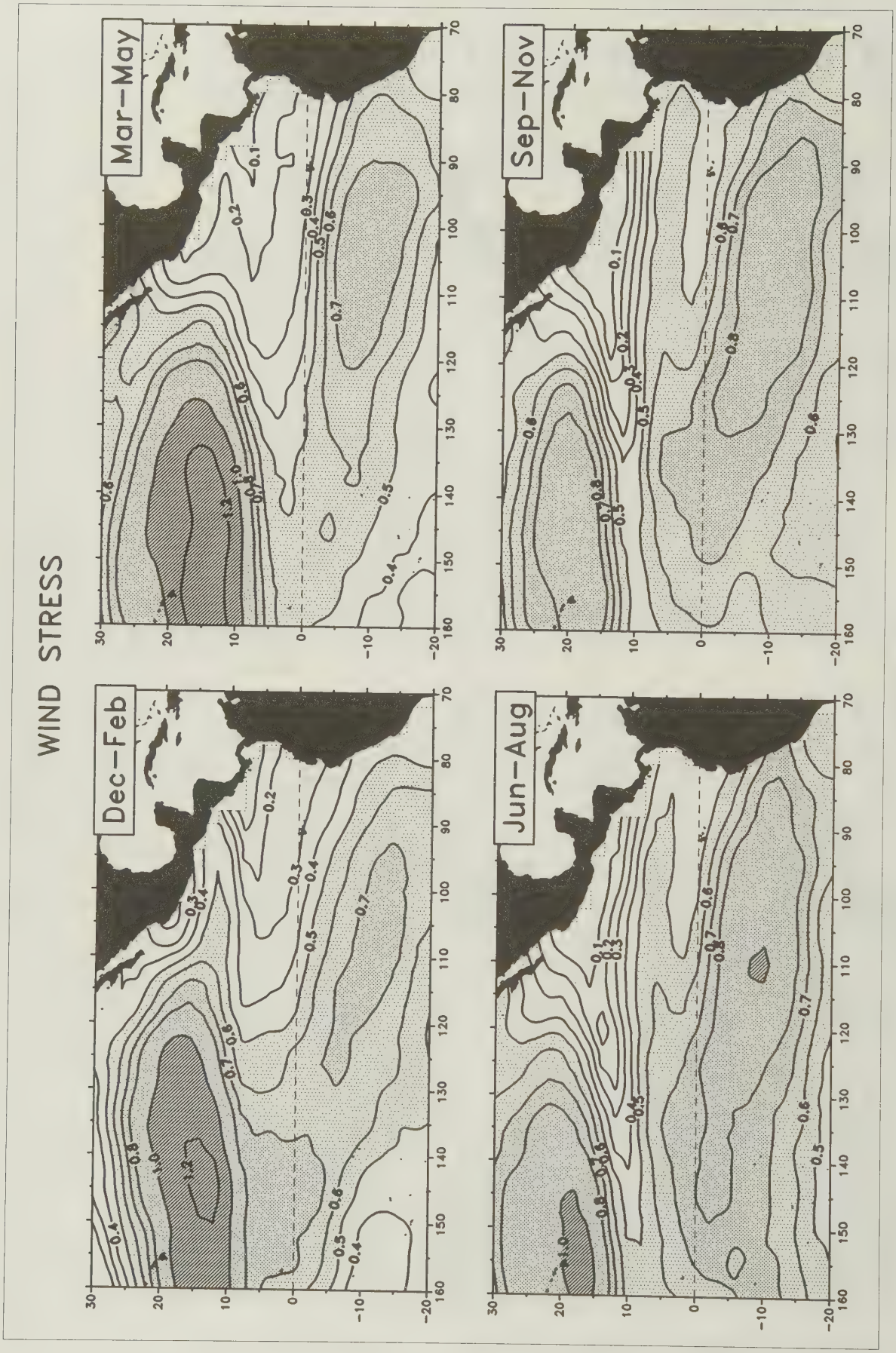

Figure A-24a
Surface wind stress seasonal climatologies (dyne cm^{-2}), derived from 1961–1989 Florida State University monthly gridded fields of pseudostress.

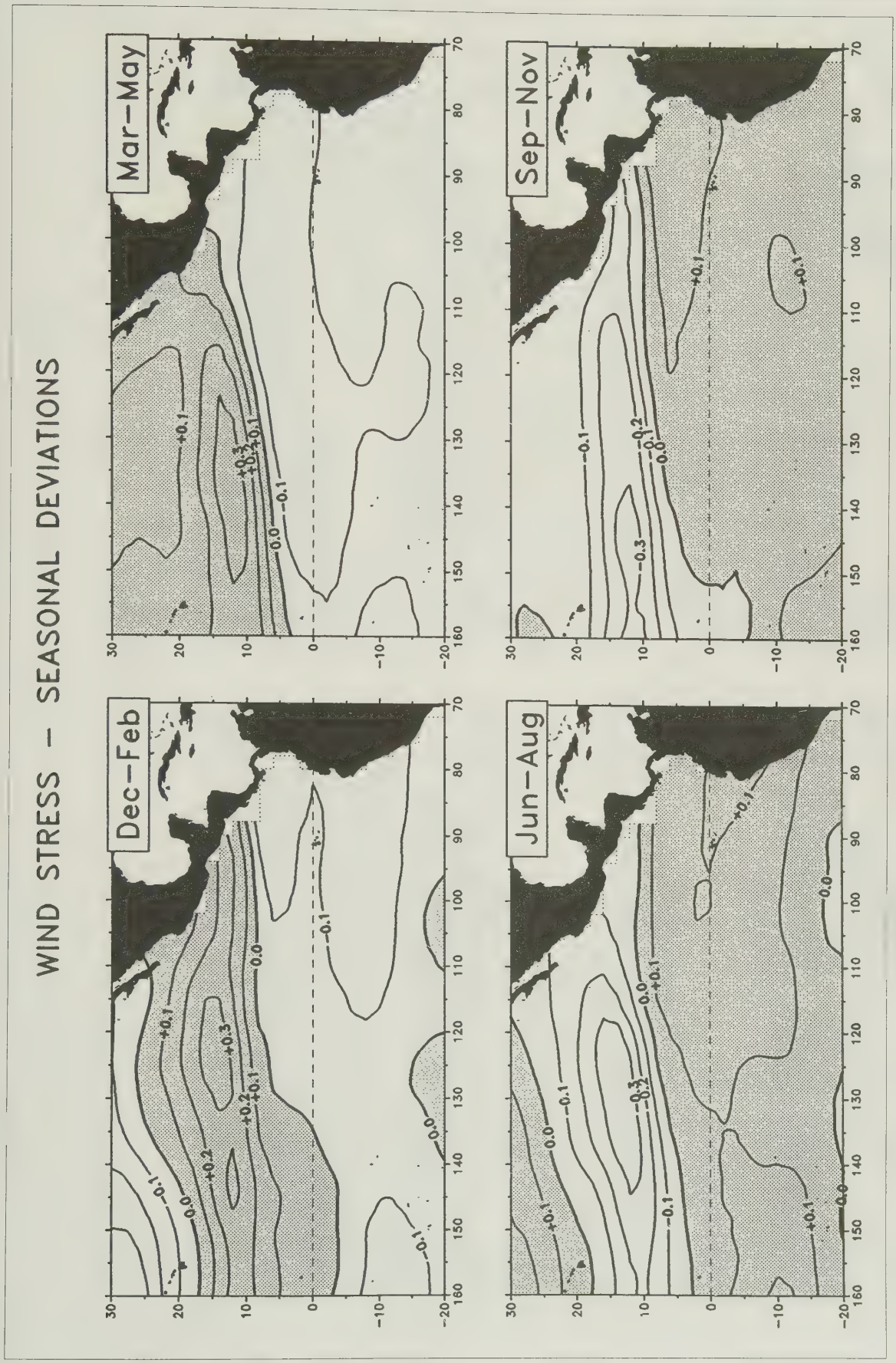

Figure A-24b
Surface wind stress seasonal deviations from annual climatology (dyne cm^{-2}).

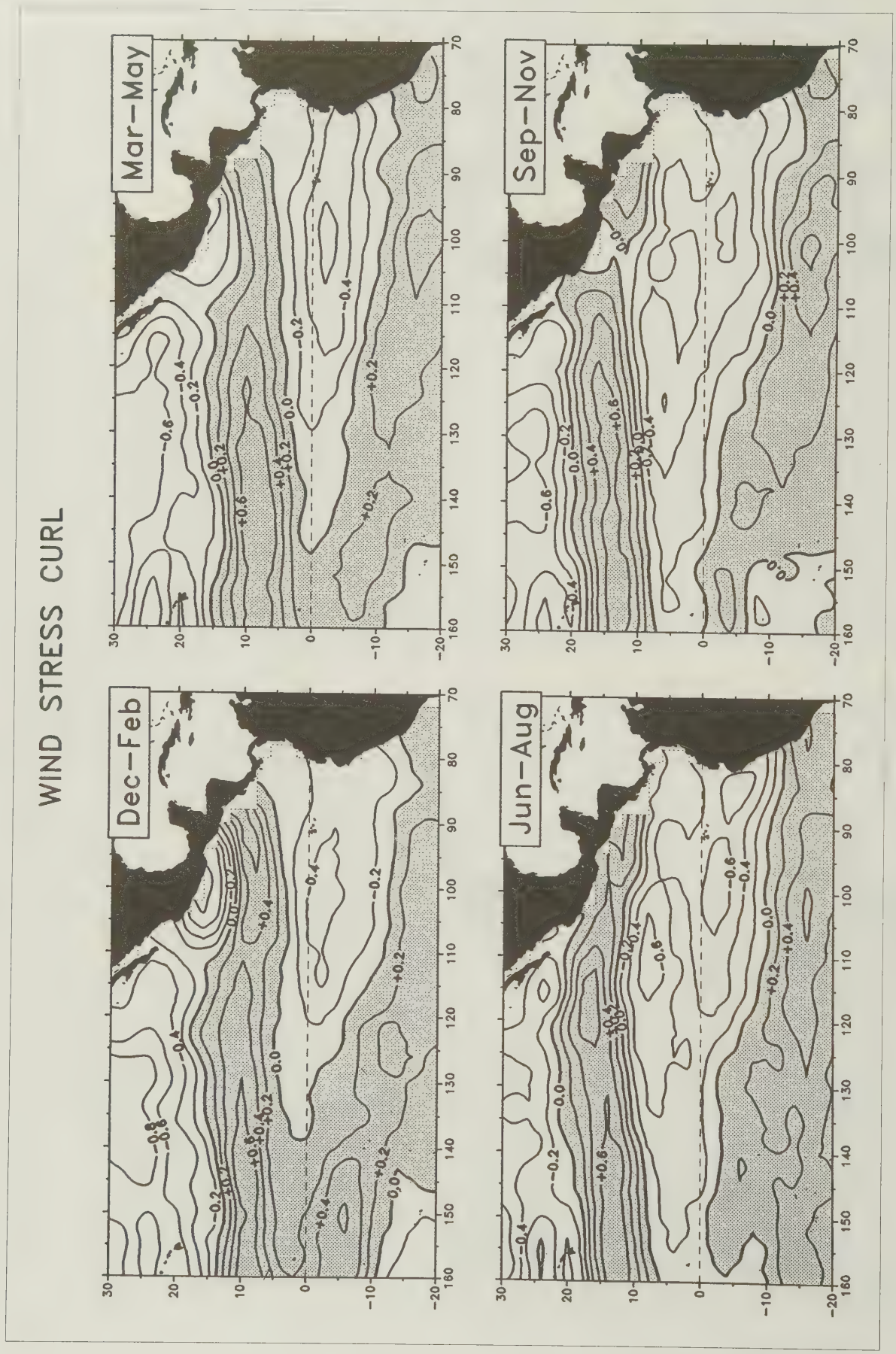

Figure A-25a

Wind stress curl seasonal climatologies (10^{-8} dyne cm^{-3}), derived from 1961–1989 Florida State University monthly gridded fields of pseudostress.

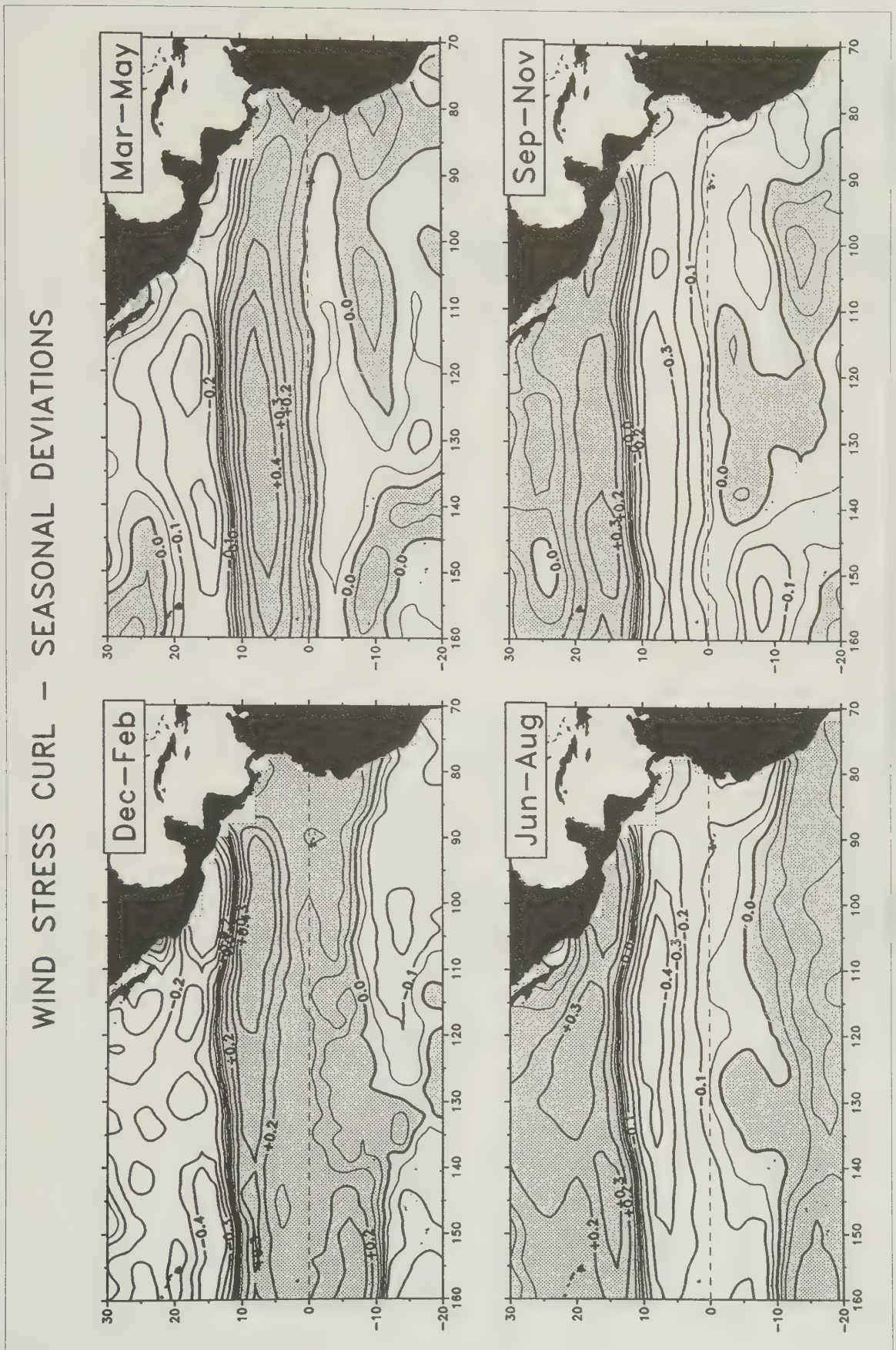

Figure A-25b
Wind stress curl seasonal deviations from annual climatology (10^{-8} dyne cm^{-3}).

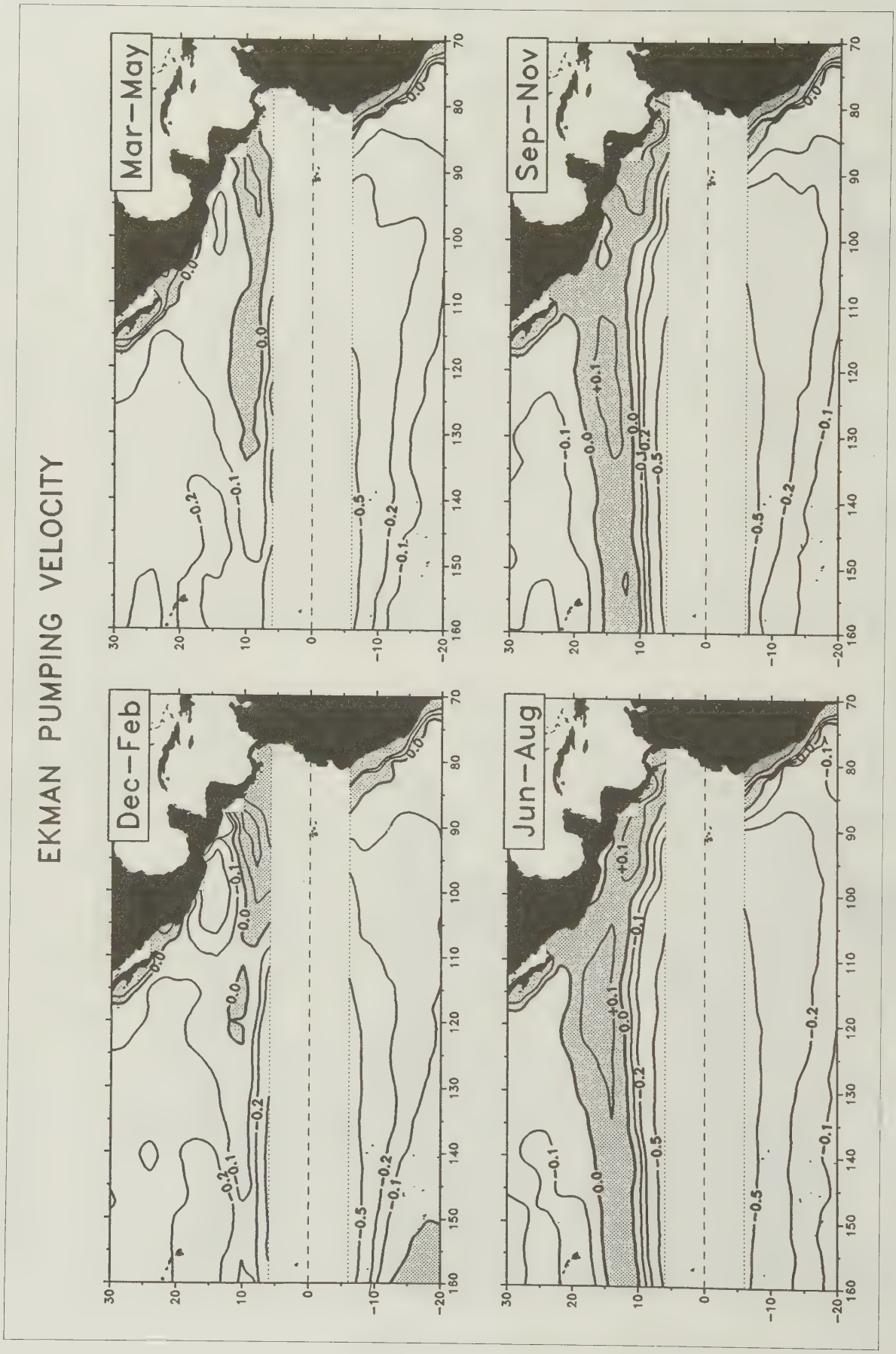

Figure A-26a

Ekman pumping velocity seasonal climatologies (10^{-3} cm s^{-1}), derived from 1961–1989 Florida State University monthly gridded fields of pseudostress.

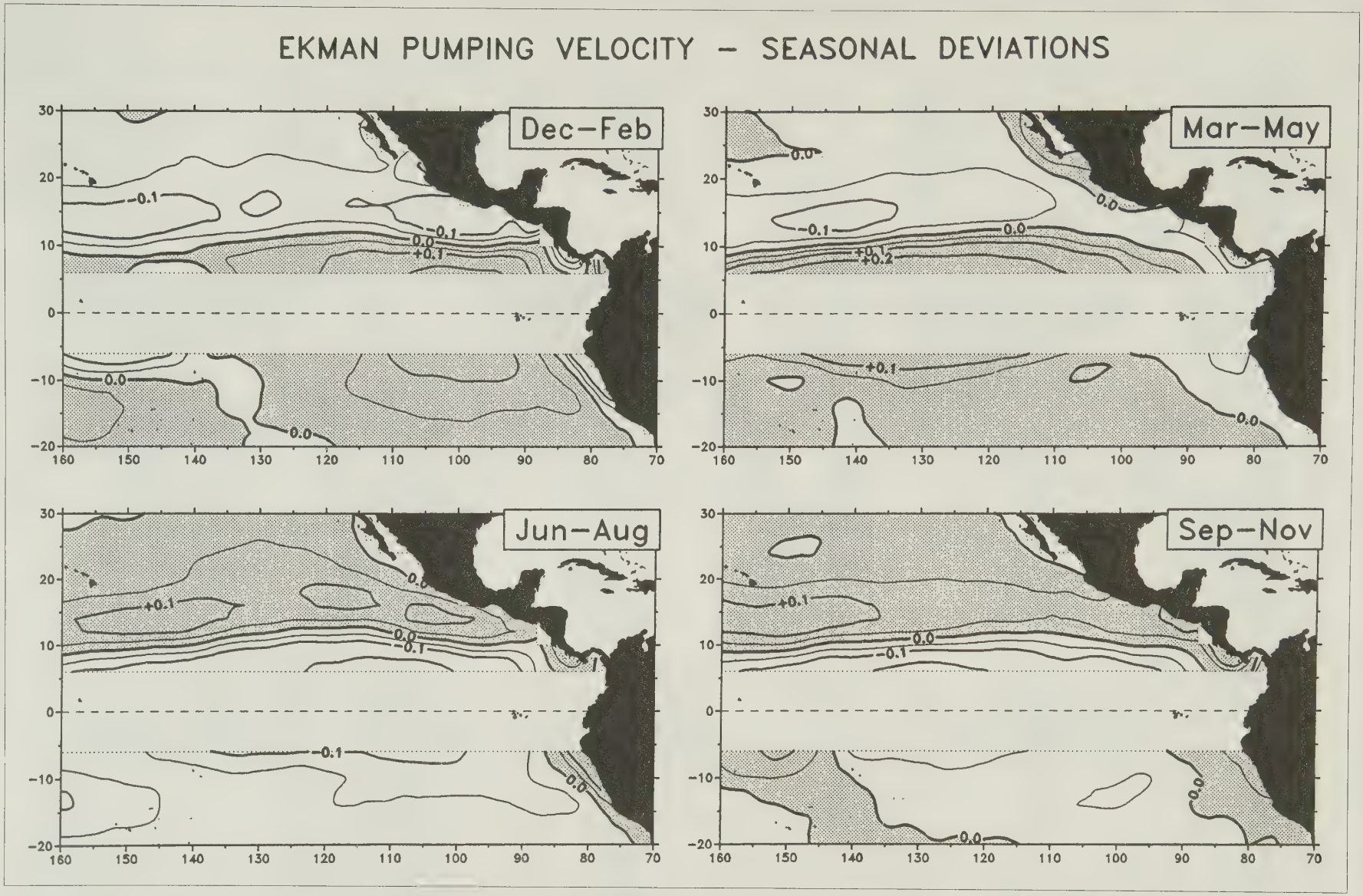

Figure A-26b
Ekman pumping velocity seasonal deviations from annual climatology (10^{-3} cm s^{-1}).

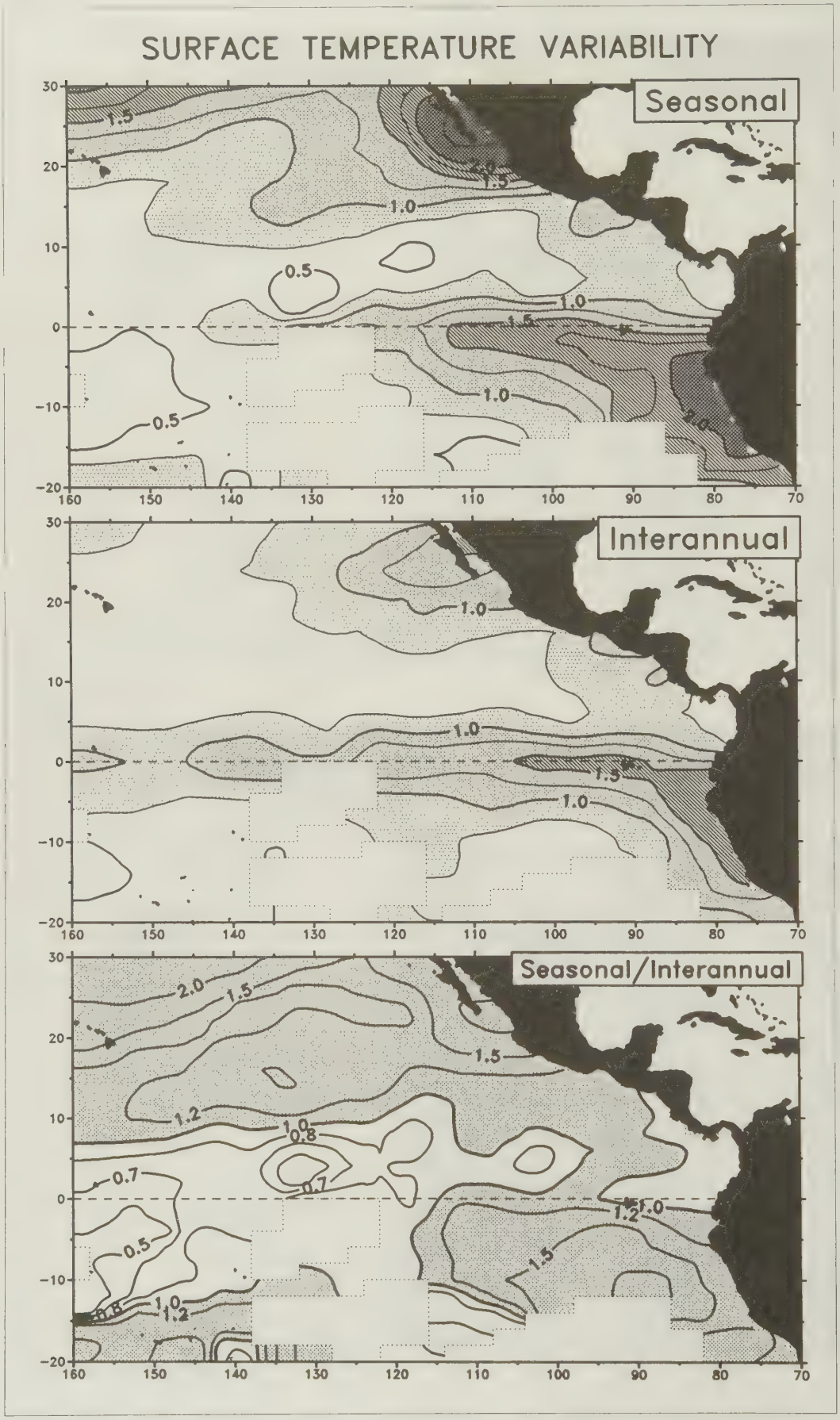

Figure A-27
Surface temperature variability (standard deviation, °C) between bimonths (seasonal) and between years (interannual), from 1960–1989 bathythermograph data.

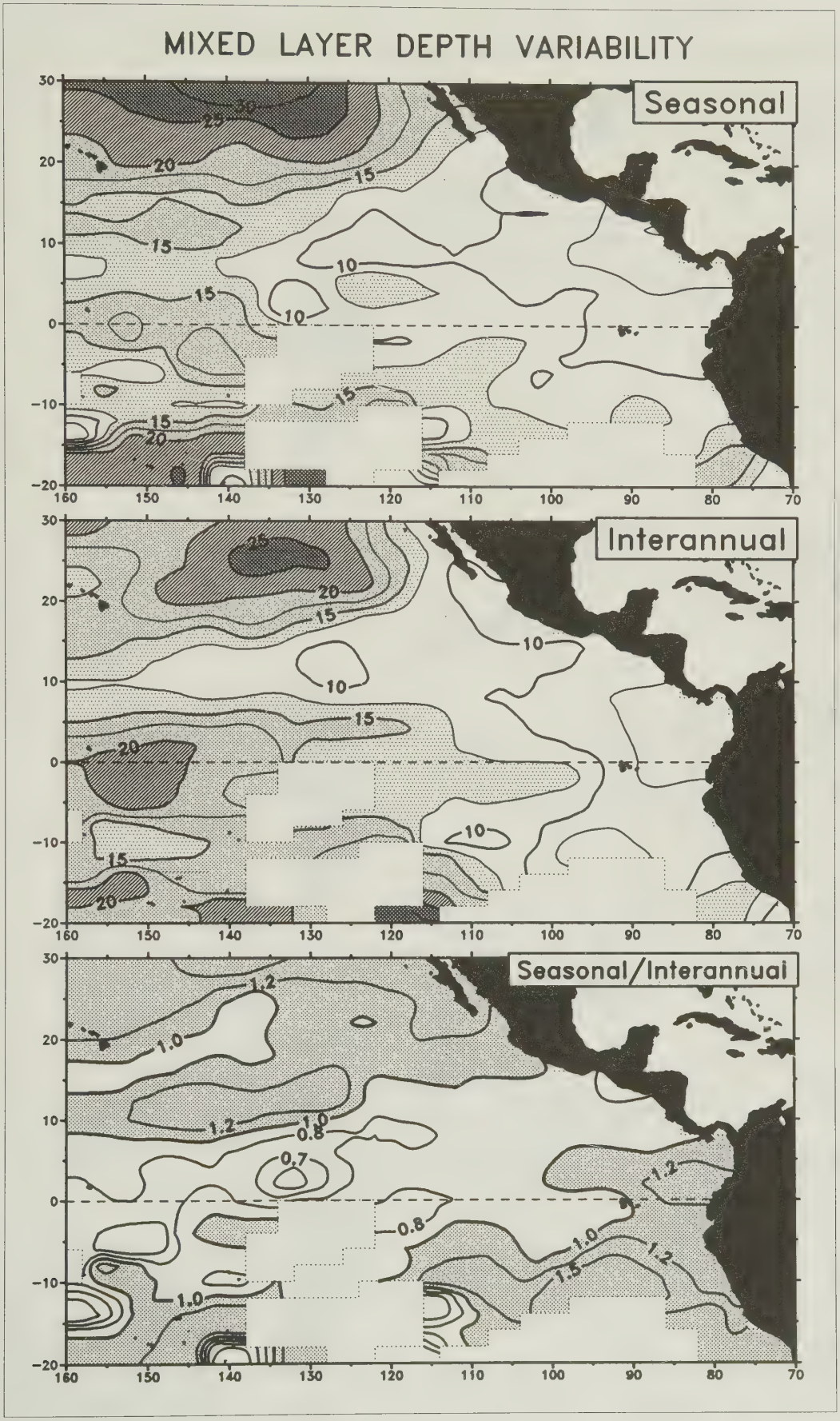

Figure A-28
Mixed layer depth variability (standard deviation, m) between bimonths (seasonal) and between years (interannual), from 1960–1989 bathythermograph data.

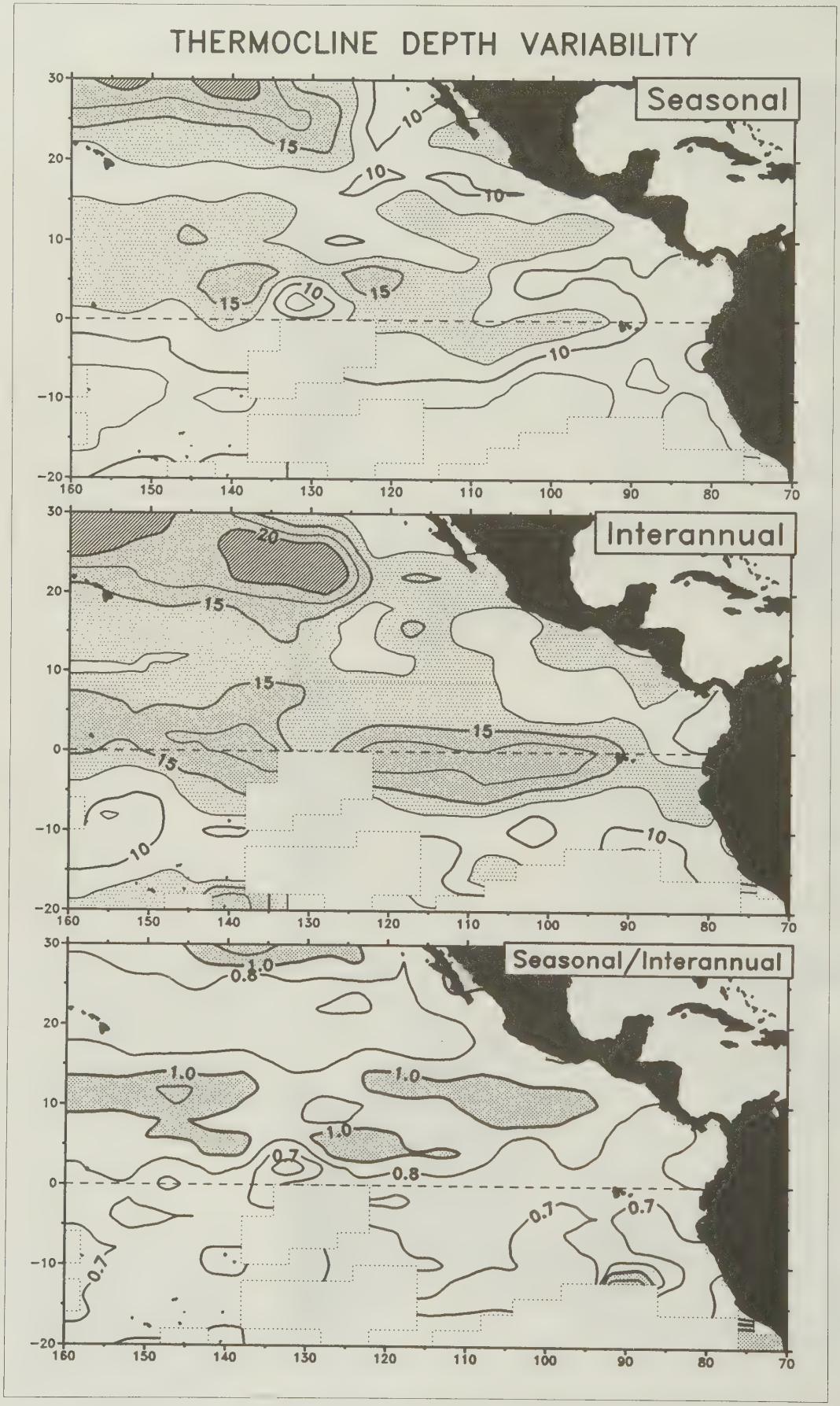

Figure A-29
Thermocline depth variability (standard deviation, m) between bimonths (seasonal) and between years (interannual), from 1960–1989 bathythermograph data.

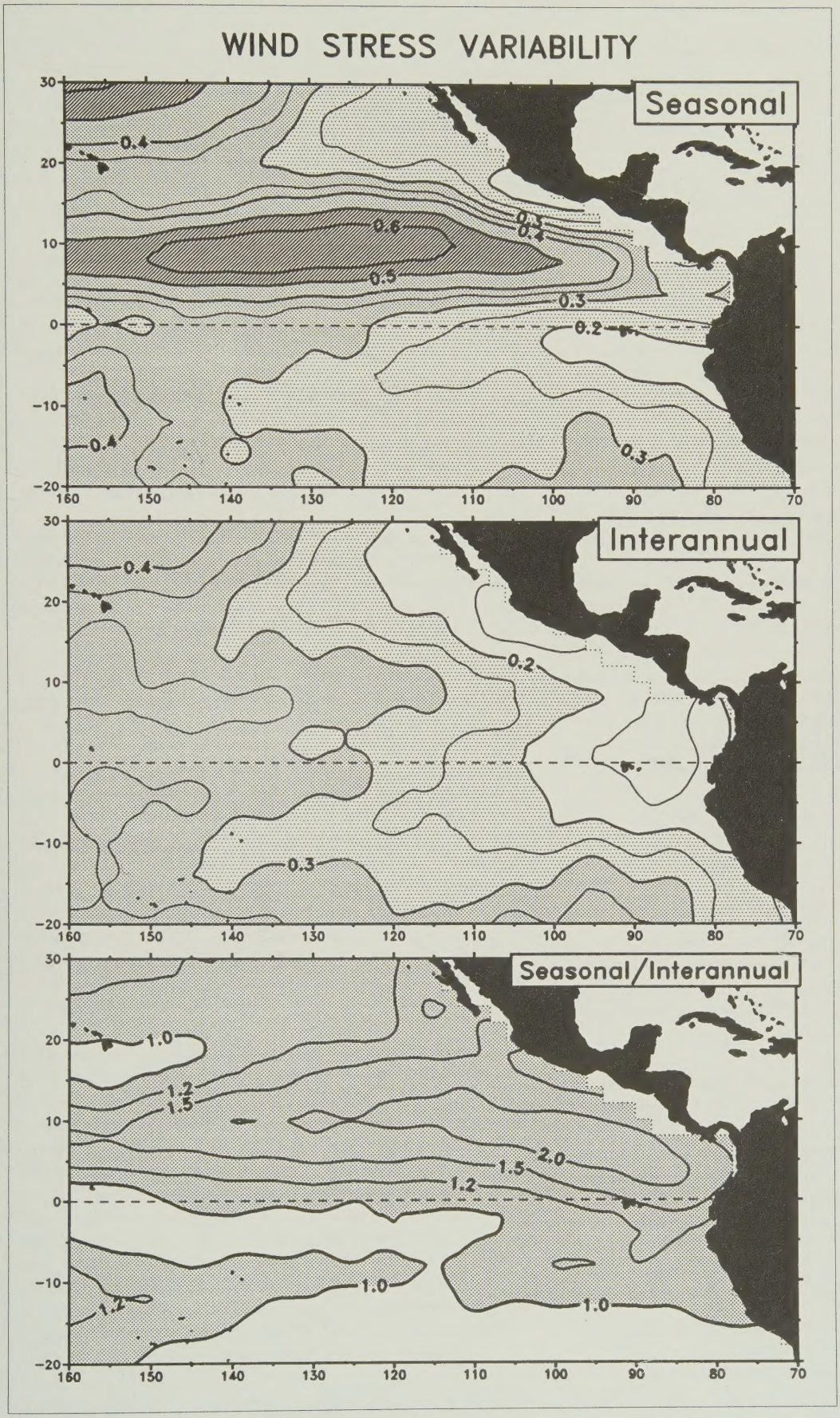

Figure A-30
Wind stress variability (standard deviation, dyne cm^{-2}) between bimonths (seasonal) and between years (interannual), from 1961–1989 Florida State University monthly gridded fields of pseudostress.

Guide for Authors

NOAA Technical Report NMFS

PREPARATION

Title of the paper should be as brief as possible (between 6 and 12 words) and should not include the Latin binomial except when it is needed for clarification, i.e., to distinguish between species sharing the same common name or between species known internationally by different common names.

Abstract should be one paragraph of about 200 words or less. It should state the main scope of the paper but emphasize its conclusions and relevant findings. Because abstracts are circulated by abstracting agencies, it is important that they represent the research clearly and concisely.

Text must be typed double-spaced throughout and should be divided into the following sections: **Introduction**, **Materials and Methods**, **Results**, **Discussion** (or **Conclusions**), and **Acknowledgments**. Headings within each section must be short, reflect a logical sequence, and follow the rules of multiple subdivision (i.e., there can be no subdivision without at least two items of subdivision). The entire text should be intelligible to interdisciplinary readers; therefore, all acronyms, abbreviations, and technical terms should be defined the first time they are used. The scientific names of species must be written in full the first time they are mentioned and abbreviated in subsequent references. Footnotes should be avoided as much as possible. We follow the *U.S. Government Printing Office, Style Manual* (1984 ed.) and the *CBE Style Manual* (5th ed.) for general format and style; the American Fisheries Society's most recent edition of *Common and Scientific Names of Fishes from the United States and Canada* for fish nomenclature. Dates should be written as 11 November 1991. Measurements should be expressed in metric units, e.g., tons as metric tons (t), but if the work is in British long tonnes, please make this fact explicit to the reader. The numeral one (1) should be typed as a one, not a lower-case el (l).

Citations comprise both unpublished and published works. Authors are advised to avoid references to nonstandard material such as internal and project reports wherever possible. For these works, include whether they are available from NTIS (National Technical Information Service) or from some other public depository. Personal communications and unpublished data must be cited in parentheses in the text with full address of communicator or author. Follow the name-and-year system for citation format. In the text, cite Smith and Jones (1977) or (Smith and Jones 1977). If there is a sequence of citations, list chronologically: Smith 1932; Green 1947; Smith and Jones 1985. Abbreviations of serials should conform to abbreviations given in *Serial Sources for Biosis Data Base*™. AUTHORS ARE RESPONSIBLE FOR THE ACCURACY AND COMPLETENESS OF ALL CITATIONS.

Tables should not be excessive in size and must be cited in numerical order in the text. All unusual symbols must be explained in the table heading. Other incidental comments can be footnoted with italic lower case letters (*a*, *b*, *c*) for general comment, with asterisks for probability in statistical data. Because tables are typeset, they need only be submitted typed and formatted.

Figures include line illustrations and photographs. Unless photographs are submitted on glossy paper with good contrast, we cannot guarantee a good final printed copy. Figures must be labeled with author's name and number of figure. Lettering within the figure should not be so heavy and large as to upstage the impact of the entire figure. Avoid "outlier" words in a figure which take up needless space. Each figure must include a legend that explains all symbols and abbreviations. These figure legends should be typewritten on a separate piece of paper at the end of the manuscript.

Copies of Published Reports are available free of charge to the senior author (50 copies) and to his or her laboratory (50). If the article is part of a proceedings or collection of articles, the senior author receives 50 free copies of the individual article and one copy of the collective work. Additional copies (reprints or offprints) of an article may be purchased in lots of 100 at a cost of $1.40 per page at the time of first printing. Additional copies of a collective work must be sought from the editor assigned to coordinate the research papers for submission as a NOAA Technical Report.

SUBMISSION

Send manuscript (original and two copies) to the Scientific Editor:

Dr. Linda Jones, Scientific Editor
National Marine Mammal Laboratory, F/AKC3
National Marine Fisheries Service, NOAA
7600 Sand Point Way NE
Seattle, WA 98115-0070.

Once the manuscript has been accepted for publication, you will be asked to submit a software copy of your manuscript to the Scientifc Editor. The software copy should be submitted in ASCII format (i.e., in a MS-DOS "print" or "nondocument" file) and should be placed on a 5.25-inch (preferably) or 3.5-inch disk that is double-sided, double or high density, and that is compatible with either IBM or Apple Macintosh systems.

Once the manuscript is being typeset and prepared for publication, all inquiries should be made to the Managing Editor:

Sharyn Matriotti, Managing Editor
NOAA Technical Reports NMFS
National Marine Fisheries Service
Scientific Publications Office, F/NWR1
7600 Sand Point Way NE
Seattle, WA 98115-0070.

UNITED STATES
DEPARTMENT OF COMMERCE
NATIONAL OCEANIC AND ATMOSPHERIC
ADMINISTRATION
NATIONAL MARINE FISHERIES SERVICE
SCIENTIFIC PUBLICATIONS OFFICE
BIN C15700
SEATTLE, WA 98115
OFFICIAL BUSINESS

Penalty for Private Use, $300

BULK RATE
POSTAGE & FEES PAID
U.S. Department of Commerce
Permit No. G-19

NOAA SCIENTIFIC AND TECHNICAL PUBLICATIONS

The National Oceanic and Atmospheric Administration was established as part of the Department of Commerce on October 13, 1970. The mission responsibilities of NOAA are to assess the socioeconomic impact of natural and technological changes in the environment and to monitor and predict the state of the solid Earth, the oceans and their living resources, the atmosphere, and the space environment of the Earth.

The major components of NOAA regularly produce various types of scientific and technical information in the following kinds of publications:

PROFESSIONAL PAPERS—Important definitive research results, major techniques, and special investigations.

CONTRACT AND GRANT REPORTS—Reports prepared by contractors or grantees under NOAA sponsorship.

ATLAS—Presentation of analyzed data generally in the form of maps showing distribution of rainfall, chemical and physical conditions of oceans and atmosphere, distribution of fishes and marine mammals, ionospheric conditions, etc.

TECHNICAL SERVICE PUBLICATIONS—Reports containing data, observations, instructions, etc. A partial listing includes data serials; predictions and outlook periodicals; technical manuals, training papers, planning reports, and information serials; and miscellaneous technical publications.

TECHNICAL REPORTS—Journal quality with extensive details, mathematical developments, or data listings.

TECHNICAL MEMORANDUMS—Reports of preliminary, partial, or negative research or technology results, interim instructions, and the like.

Information on availability of NOAA publications can be obtained from:

U.S. Department of Commerce
National Technical Information Service
5285 Port Royal Road
Springfield, VA 22161